Greedy, Stephen (2002) Advances in the Spectral Index method for the analysis of photonic integrated circuits. PhD thesis, University of Nottingham.

# Advances in the Spectral Index Method for the Analysis of Photonic Integrated Circuits

by

Stephen Greedy, MEng

Thesis submitted to the University of Nottingham for the

Degree of Doctor of Philosophy, July, 2002.

# Acknowledgements

# Abstract

The prolific rate at which advances in photonics have been made in recent years has increased the need for accurate and efficient computer aided design tools. New device technologies and material systems mean the designer is faced with many more degrees of freedom with which to optimise a design. Because of this versatile techniques that yield results accurately and quickly are foremost in the designers mind.

Throughout this work a well proven technique, the Spectral Index (SI) method is extended and generalised to a wide variety design situations of practical importance.

The design of a novel Silicon Germanium based device was used to prove the suitability of an iterative design methodology in developing and optimising practical waveguiding components. The novel development of the SI method for the accurate analysis of waveguide losses is then presented further extending its suitability to the analysis and design of rectangular rib waveguides. Following this the generalisation of the SI method to structures of non-rectangular cross-section is presented allowing for the analysis of a wider range of optical rib waveguides.

A novel implementation of the SI method is then developed for the analysis of the whispering gallery class of resonant modes supported by cylindrical dielectric disc and ring structures, allowing for the characterisation of the optical properties of this important class of devices.

A 3D circuit analysis technique based upon a robust implementation of the SI method in its complex form is developed that allows for the characterisation of any waveguide system that may be represented by a number of discrete waveguide components. Finally the SI method is generalised to the full 3D exact analysis of optical waveguiding structures.

# List of Publications

The following is a list of publications that have been published to date as a result of the work presented in this thesis.

1. Stephen C. Greedy, Phillip Sewell, Trevor M. Benson, "**A Generalised Spectral Index Approach for the Analysis of 3D Structures",** *Presented at Photonics West,San Jose, January 2001.*

2. Stephen C. Greedy, Svetlana V. Boriskina, Phillip Sewell, Trevor M. Benson, "**Design and Simulation Tools for Optical Micro-resonators",** *Presented at Photonics West,San Jose, January 2001.*

3. S. C. Greedy, H. F. Arrand, P. D. Sewell, T. M. Benson, "**Fibre Coupling to SiGe Optoelectronic Devices",** *IEE Proc.-Optoelectronics, vol. 147, No. 6, pp. 391-394, December 2000.*

4. S Greedy, P Sewell, TM Benson, "**Spectral Index Method Applied to the Analysis of Whispering Gallery Modes in Semiconductor Disk Resonators",** *International Conference on Mathematical Methods in Electromagnetic Theory ,MMET 2000, vol. 2, pp 412-414, 2000.*

5. S Greedy, P Sewell,S V Boriskina, TM Benson, "**Efficient Analysis of Semiconductor Resonators",** *Presented at Piers2000, Boston, July 2000 .*

6. TM Benson, P Sewell, H F Arrand,S Greedy, "**Silicon-based Optical Waveguides (invited paper)",** *Presented at E-MRS2000, Strasbourg, June 2000*

7. A Vukovic, S Greedy, P Sewell, TM Benson and PC Kendall, "**Advances in spectral methods for optoelectronic design",** *FACTA UNIVERSITATIS (NIS) Series Electronics and Energetics, vol 13, no 1, pp 73-82, 2000.*

8. S. Greedy, P Sewell, T. M. Benson, "**Spectral Index Method Applied to Semiconductor Micro-Ring and Disk Resonators",** *Presented at Semiconductor and Integrated Optoelectronics conference,SIOE'99, Cardiff, April 2000.*

9. S. Greedy, H. F. Arrand, P. Sewell, T. M. Benson, "**Fibre Coupling to SiGe Optoelectronic Devices",** *Presented at Postgraduate Research in Electronics and Photonics,PREP 2000, Nottingham, April 2000.*

10. A Vukovic, S Greedy, TM Benson, P Sewell, PC Kendall, "**Advances in Spectral Methods for optoelectronic design",** *4th International Conference on Telecommunications in Modern Satellite, Cable & Broadcasting Services, TELSIKS '99, vol. 2, pp. 329-332, 1999.*

11. S Greedy, P Sewell, TM Benson, PC Kendall, "**Spectral Index Method Applied to Oblique Walled Rib Waveguides",** *Presented at Semiconductor and Integrated Optoelectronics conference, SIOE'99, Cardiff, April 1999.*

# Contents

# List of Principal Symbols

| | |
|---|---|
| $B$ | magnetic induction |
| $D$ | electric displacement |
| $E$ | electric field |
| $\tilde{e}$ | Fourier transform of the electric field |
| $H$ | magnetic field |
| $V$ | voltage |
| $I$ | current |
| $Y$ | admittance |
| $Z$ | impedance |
| $t$ | time |
| $k, k_0$ | wavenumber |
| $n, n_1, n_2 \ldots n_x$ | material refractive indices |
| $s$ | spectral Fourier variable |
| $x, y, z$ | rectangular coordinate system |
| $r, \phi, y$ | cylindrical coordinate system adopted in this work |
| $\beta$ | longitudinal propagation constant |
| $b$ | normalized propagation constant |
| $\gamma$ | transverse propagation constant |
| $\omega$ | angular frequency |
| $\Delta_t, \Delta_n$ | Goos-Hänchen shift (rectangular system) |
| $\Delta r_t, \Delta r_n$ | Goos-Hänchen shift (cylindrical system) |
| $\varepsilon$ | dielectric permittivity |
| $\varepsilon_0$ | permittivity of free space |
| $\varepsilon_r$ | relative permittivity |
| $\mu_0$ | permeability of free space |
| $\mu_r$ | relative permeability |
| $\lambda$ | wavelength |

# Chapter 1 Introduction

## 1.1 Background and Motivation for the Work Described in the Thesis

Efficient and accurate analysis methods are essential tools for the design and optimisation of both traditional and emerging optical waveguide based technologies. The rapid turnaround of designs, from drawing board to fabrication, is a major factor in their overall success in today's technology climate. Along with this, the ever increasing desire for systems with greater functionality and higher bandwidth inevitably results in an increase in the complexity of modern integrated optoelectronic circuits (OEICs).

The concept of integrated optics was proposed by S. E. Miller of Bell Laboratories in 1969, [1.1]. In its most basic form the device consisted of a source, a waveguide and a detector each fabricated in a dissimilar material system and hence were of a hybrid nature, [1.2]. The hybrid approach, although being most versatile, requires assembly of the separate components each of which, whilst being relatively easy to fabricate, will suffer greatly in performance if poorly assembled. Accurate alignment of components is required and any mismatch introduces a loss mechanism (cf. impedance mismatch in transmission line circuits) and, at best, results in poor performance. Monolithic integration of all the components is therefore desired,

whereby all the components are fabricated on a single substrate avoiding any post production assembly of components and hence alignment issues, [1.3].

The progress of monolithic integration is reliant on the required device functions being feasible in the material system. Silicon (Si), being the most common and favourable semiconductor device material, is appealing for optoelectronic applications as it is ideally suited to large scale manufacture of monolithic OEICs. Although Si is transparent over the all important optical communication range (1.3-1.55μm), [1.4]-[1.5], the material had traditionally been overlooked for use in communications systems due to it being an indirect band gap material and hence, unsuitable for active device applications. Recent developments in active Si based material alloys, [1.6]-[1.8], namely SiGe, have seen a resurgence of interest in Si as a viable alternative to the more traditional III-V group of compounds, such as Gallium Arsenide (GaAs) and Indium Phosphide (InP).

The development of novel devices, fabrication methods and new technologies form the major contributions to the field of optoelectronics. But, the reliance upon the computer aided design (CAD) process as an enabling factor for the increased rate at which these developments take place should not be underestimated. The reduction in the length of the design cycle for existing and emerging optical technologies pushes forward new developments that may otherwise be hindered for reasons of economy.

In order to determine the stability of any design within a range of fabrication and operational tolerances, and to arrive at the optimum design, it is necessary to carry

out the modelling process for a range of parameters. Therefore analysis methods that readily lend themselves to an iterative design procedure are sought that are not only accurate but fast. Such methods allow for the efficient exploration of device operation across a range of parameters and also allow the designer to retain an intuitive grasp for the operation of a device.

Computer based analysis methods are required to model a wide range of optical components, from simple longitudinally invariant rectangular rib waveguides through to complex optical circuits. Many methods have developed to date but the different approaches generally fall into one of three categories; numerical, semi-analytical or analytical. Numerical methods, such as those based on finite differences [1.9]- [1.13], are generally accepted as the most versatile and accurate approaches, relying on the discretisation of the problem space. They are therefore readily applied to devices of complex cross-section, passive and active materials and full 3D analysis of complex circuits, but this generality comes at the expense of computational overheads. Memory requirements and computation time may make numerical methods impracticable unusable in a general design environment. Analytical methods are applicable only in the simplest of cases and so are restricted in their range of use. Semi-analytical approaches, [1.15]- [1.18], form a compromise, in that they make use of *a priori* knowledge of the solution typically gained from experimental analysis, or make use of approximations without loss of accuracy. The problem is thus greatly simplified and results in the production of accurate results with minimal computational effort. Therefore semi-analytical techniques lend themselves extremely well to an iterative design process. The Spectral Index (SI)

method, [1.19]-[1.21], is one such approach that has traditionally been applied to the analysis of air clad semi-conductor rib waveguides with great success. Throughout this thesis the philosophy of the SI method is used as a basis for the formulation of semi-analytical approaches to the analysis of a wider range of components and devices. The suitability of the method is also demonstrated through application to the successful design of optical components and circuits.

Component fabrication issues are an important consideration in the design process. Process tolerances may not only result in differences in dimensions, but severely affect the geometry of the device. Optimisation of device performance within the constraints of fabrication issues is therefore an important consideration. Generalisation of the SI method to the analysis of rib waveguides of arbitrary cross section is the first novel contribution of the present work and was developed to account for the anisotropy of the vertical etching processes that produce waveguides of trapezoidal cross section, [1.22]. Such trapezoidal cross sections may also occur as a result of design of electro-optic devices, where they can be employed to beneficially tailor electrical characteristics such as current distribution, and so the approach is more widely applicable to the design of such devices.

Mono-modal propagation is a desired characteristic of many optical waveguides and has been achieved in rib waveguide structures of large cross section with respect to wavelength, [1.23]-[1.24], that are suitable for coupling to single mode optical fibres. Single mode operation is achieved by ensuring that all the modes except the fundamental are highly attenuated. One method of accomplishing this is by

controlling the leakage of these higher order modes into the substrate. Alternatively, by designing the waveguide so that the propagation constants of the higher order modes lie below that of the outer slab regions mono-modal propagation may be obtained. When the outer slab regions of the rib waveguides support guided modes an additional loss mechanism is introduced. The calculation of this additional loss is important for the accurate design of mono-modal waveguide systems and is introduced for the first time in this thesis.

Along with longitudinally invariant waveguides other optical components play important roles in developing the functionality of OEICs. One such component is the circular dielectric resonator, that has recently found favour as a wavelength selective device because of the high Q's that may be realised through their use, [1.25]-[1.26]. A novel SI based approach is developed in this work that allows for the efficient analysis of theses promising components.

## 1.2   Thesis Organisation

The following outlines the organisation of the work contained in this thesis. In cases where a novel technique has been introduced comparisons with results gained from existing methods are drawn as appropriate and discussed in context with the work described.

In chapter 2 the motivation of this work is expanded in context with the present state of the art in optical waveguide modelling. The principles of wave optics are then

introduced and discussed. From the starting point of the source free Maxwell's equations for non-magnetic isotropic media, the general wave equation is derived in Cartesian coordinates and consequently simplified in lieu of approximations that are valid for given situations. As a pre-emptor to the development of the SI approach to dielectric resonators, the general wave equation in cylindrical coordinates is derived. The concept of modes is discussed and the method of false position, key in the development of the SI method, is then described. This is followed an introduction to the variational boundary condition that is another key element in the formulation of the SI approach. Circuit concepts as applied to optical waveguides are outlined. Methods commonly applied to the analysis of optical waveguides are then introduced and discussed within the framework of this thesis.

In chapter 3 the SI method is described in detail, introducing the fundamental concepts of the approach, its suitability and its limitations. The application and extension of the method prior to this work is also discussed.

In chapter 4 the suitability of the SI method to an iterative design process is demonstrated through the development of a novel waveguide based device - a rib waveguide based spot size converter (SSC). The design was fabricated and consequently experimentally analysed as part of this work and resulted in the first such SSC demonstrated in silicon-germanium (SiGe). This chapter also covers the material properties of SiGe that required consideration in producing a successful design and draws attention to some of the many variables the designer is faced with.

Chapter 5 extends the SI method for the first time to the analysis of rib waveguides of arbitrary cross-section. The method provides the means for the inclusion of non-rectangular cross-sections that results from the fabrication process, but is generally applicable to devices of arbitrary cross section that fall within the remit of the SI approach.

In chapter 6 a novel technique for the accurate analysis of a waveguide loss mechanism is developed that has importance for the design of single mode waveguide systems.

Chapter 7 builds upon the philosophy of the SI method to develop a technique for the analysis of circular dielectric resonators that operate in the whispering gallery mode regime. Operated in this mode, dielectric resonators yield extremely high Q factors making them highly desirable components for inclusion in optical signal processing circuits e.g. wavelength division multiplexing (WDM) circuits. The basic method is then extended to the analysis of ring dielectric resonators.

In chapter 8 the SI method is applied to the analysis of a full 3D circuit based upon multi-mode interference (MMI) components. The analysis of such circuits with a high aspect ratio (micrometers wide and millimetres long) using purely numerical methods would prove prohibitive in terms of computational effort, requiring enormous run times and memory resources. The efficiency the SI approach allows for a full circuit simulation on a standard pc in a matter of minutes, providing important information such as field profiles and device insertion loss.

Chapter 9 introduces a novel technique, again for the analysis of 3D circuits. Whereas the technique introduced in the previous chapter is based upon a scattering matrix approach the new technique generalises the SI method to the analysis of fully three dimensional structures. Finally, chapter 10 draws together the main conclusions of this work, together with a discussion on further study that may build upon the work introduced here.

## 1.3   References

[1.1]   S. E. Miller, Bell System Technical Journal, vol.48, pp. 2059, 1969.

[1.2]   T. Tamir, "Integrated Optics", Springer-Verlag, New York, 1979.

[1.3]   I. Moerman, P. P. Van Daele, P. M. Demeester, "A review on fabrication technologies for the monolithic integration of tapers with III-V semiconductor devices", IEEE Journal of Selected Topics in Quantum Electronics, vol. 3, pp. 1308-1320, 1997.

[1.4]   J. S. Richard, R. A. Soref, and K. laus Petermann, "Large Single-Mode Rib Waveguides in GeSi-Si and Si-on-SiO2", IEEE Journal of Quantum Electronics, vol. 27, pp. 1971-1974, 1991.

[1.5]   R. A. Soref, "Silicon based optoelectronics", Proc. IEEE, vol. 81, pp. 1687-1706, 1993.

[1.6]   B. Schüppert, J. Schmidtchen, A. Splett, U. Fischer, T. Zinke, R. Moosburger, and K. Petermann, "Integrated Optics in Silicon and SiGe-Heterostructures", IEEE Journal of Lightwave Technology, vol. 14(10), pp. 2311-2323, 1996.

[1.7]   L. Naval, B. Jalali, L. Gomelsky, and J. M. Lui, "Optimization of $Si_{1-x}Ge_x$/Si Waveguide Photodetectors Operating at $\lambda$=1.3 $\mu$m", IEEE Journal of Lightwave Technology, vol. 14(5), pp. 787-797, 1996.

[1.8]   B. Li, G. Li, E. Lui, Z. Jiang, J. Qie, and X. Wang, "Monolithic integration of a SiGe/Si modulator and multiple quantum well photodetector for 1.55 $\mu$m operation", Applied Physics Letters, vol. 73(24), pp. 3504-3505, 1998.

[1.9]   K. S. Yee, "Numerical solution of initial boundary value problems involving Maxwell's equations in isotropic media", IEEE Trans. on Antennas and Propagation, vol. 14, pp. 302-307, 1966.

[1.10]  S. T. Chu, and S. K. Chaudhuri, "A finite-difference time-domain method for the design and analysis of guided-wave optical structures", Journal of Lightwave Technology, vol. 7, pp. 2033-2038, 1989.

[1.11]  M. D. Feit, and J. A. Fleck, "Light propagation in graded-index optical fibers", Applied Optics, vol. 17, pp. 3990-3998, 1978.

[1.12]  Reinhard März, "Integrated Optics Design and Modeling", Boston/London, Artech House, 1994.

[1.13]  B. M. A. Rahman, F. A. Fernandez, and J. B. Davies, "Review of finite element methods for microwave and optical wavguides", Proc. IEEE, vol. 79, 1442-1448, 1991.

[1.14]  S. M. Saad, "Review of numerical methods for the analysis of abitarily-shaped microwave and optical dielectric waveguides", IEEE Trans. Microwave Theory and Tech., vol. 33, pp. 894-899, 1985.

[1.15]  P. N. Robson, and P. C. Kendall (Ed.), "Rib Waveguide Theory by the Spectral Index Method", Chapter 4, Research Studies Press, 1990.

[1.16]  M. J. Robertson, P. C. Kendall, S. Ritchie, P. W. A. McIlroy, and M. J. Adams, "The weighted index method: a new technique for analyzing planar optical waveguides", Journal of Lightwave Technology, vol. 7, pp. 2105-2111, 1989.

[1.17]  N. Dagli, "Equivalent circuit representation of open guided-wave structure", Journal of Quantum Electronics, vol. 26, pp. 98-108, 1990.

[1.18] J. A. Kong, "Methods for modelling and simulation of guided-wave optoelectronic devices: Part I: Modes and couplings", EMW Publishing Cambridge/Massachusetts, 1995.

[1.19] P. C. Kendall, P. W. A. McIlroy, and M. S. Stern, "Spectral index method for rib waveguide analysis", Electronics Letters, vol. 25(2), pp. 107-108, 1989.

[1.20] P. W. A. McIlroy, M. S. Stern and, P. C. Kendall, "Spectral index method for polarized modes in semiconductor rib waveguides", Journal of Lightwave Technology, vol. 8(1), pp. 113-117, 1990.

[1.21] P. N. Robson, and P. C. Kendall (Ed.), "Rib Waveguide Theory by the Spectral Index Method", Chapter 5, Research Studies Press, 1990.

[1.22] S. Adachi, O. Kunishige, "Chemical etching characteristics of (001) GaAs", Journal of the Electrochemical Society, vol. 130(12), pp. 2427-2435, 1983.

[1.23] R. A. Soref, J. Schmidtchen, and K. Petermann, "Large single-mode rib waveguides in GeSi-Si and Si-on-SiO$_2$", IEEE Journal of Quantum Electronics, vol. 27(8), pp. 1971-1974, 1991.

[1.24] S. P. Pogossian, L. Vescan, and A. Vonsovici, "The single mode condition for semiconductor rib waveguides with large cross section", Journal of Lightwave Technology, vol. 6(10), pp. 1851-1853, 1998.

[1.25] C. Verdrenne, and J. Arnaud, "Whispering-gallery modes of dielectric resonators", Proc. Inst. Elec. Eng, vol. 129(H), pp. 183-187, 1982.

[1.26] X. H. Jiao, P. Guillon, L. A. Bermudez, and P. Auxernery, "Whispering-gallerymodes of dielectric structures: Appluactions to millimetre-wave bamdstop filters", IEEE Trans. Microwave Theory and Techniques, vol. MTT-35, pp. 1169-1175, 1987.

# Chapter 2 Background Theory and Analysis Techniques

This chapter presents an overview of the electromagnetic fundamentals that provide the basis for the work developed in this thesis. Maxwell's equations as they apply to the material properties at optical frequencies are given, together with the boundary conditions for optical waveguides. From here the wave equations for longitudinally invariant waveguides are derived in both rectangular and cylindrical co-ordinate systems. The concept of waveguide modes is then introduced along with the classification of propagation regimes. The method of false position and variational principle are described, both of which, although being applicable to a variety of analysis techniques, are fundamental to the development of the Spectral Index method used as a basis throughout this work. The chapter then continues by introducing some of the more common methods employed in the solution of Maxwell's equations.

## 2.1 Optical fields and Maxwell's equations

Being a time dependent electromagnetic wave, an optical field can be completely described by Maxwell's equations, [2.1]. In a source free region Maxwell's equations in their differential form are

$$\nabla \times \vec{E} = -\frac{\partial \vec{B}}{\partial t} \qquad (2.1)$$

$$\nabla \times \vec{H} = \frac{\partial \vec{D}}{\partial t} \tag{2.2}$$

$$\nabla \cdot \vec{D} = 0 \tag{2.3}$$

$$\nabla \cdot \vec{B} = 0 \tag{2.4}$$

where $\vec{E}$, $\vec{H}$, $\vec{D}$ and $\vec{B}$ are the time dependent vectors of the electric and magnetic fields, the displacement vector and the magnetic induction vector respectively. The introduction of Maxwell's two constitutive relationships provides the mechanism to relate the dependence of the optical field to the characteristics of the guiding medium and are defined for the isotropic media considered as

$$\vec{D} = \varepsilon \vec{E} \tag{2.5}$$

$$\vec{B} = \mu \vec{H} \tag{2.6}$$

These introduce the dielectric permittivity, $\varepsilon$ and the magnetic permeability, $\mu$, of the medium. The dielectric permittivity is further defined as $\varepsilon = \varepsilon_0 \varepsilon_r$, where $\varepsilon_r$ is the relative permittivity or dielectric constant of the medium and $\varepsilon_0$ the free space permittivity. The magnetic field is defined similarly as $\mu = \mu_0 \mu_r$, but in the context of this work only non-magnetic materials are considered, $\mu_r = 1$, and thus only the free

space permeability, $\mu_0$, is used in (2.6). At optical frequencies it is more common to consider the refractive index of the material, n, which is given by $\sqrt{\varepsilon_r}$. It is further noted that the refractive index is frequency dependent and is, in general, a complex quantity.

## 2.2  Boundary conditions for optical waveguides

Maxwell's equations, as stated in (2.1)-(2.4), hold true for homogenous regions. Commonly, optical waveguides rely on an abrupt change in refractive index across a surface to provide a confinement mechanism. It is therefore necessary that the quantities under investigation satisfy certain boundary conditions across the interface separating the different media. Figure 2-1 illustrates this situation where the differing media are classified by their refractive indices $n_1$ and $n_2$, where $\vec{n}$ is the unit normal to the interface.   The conditions, in the absence of surface charge and surface currents, are

$$\vec{n} \times \left( \vec{E}_1 - \vec{E}_2 \right) = 0, \quad \vec{n} \times \left( \vec{H}_1 - \vec{H}_2 \right) = 0$$
$$\vec{n} \cdot \left( \vec{D}_1 - \vec{D}_2 \right) = 0, \quad \vec{n} \cdot \left( \vec{B}_1 - \vec{B}_2 \right) = 0 \tag{2.7}$$

which for non-magnetic media maybe stated as; the tangential component of the fields $\vec{E}$ and $\vec{H}$ are continuous across the boundary, the normal component of the field, $\vec{H}$, and the normal component of the electric flux, $\vec{D}$. The latter further

implies that the electric field is subject to a jump due to the discontinuity in the refractive indices of the media as it is required that

$$\varepsilon_1 E_{n_1} = \varepsilon_2 E_{n_2} \tag{2.8}$$
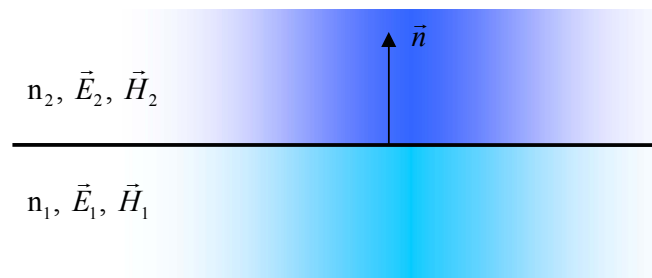


**Figure 2-1** Illustration of the boundary between two different media.

## 2.3 The wave equation – rectangular coordinates

Figure 2-2 illustrates a typical rib waveguide together with the co-ordinate system adopted in this thesis. From Maxwell's equations a general vector wave equation may be derived for either the electric or magnetic field that describes totally the optical field supported by a waveguide of refractive index distribution $n = n(x, y, z)$. Assuming a time dependence of $e^{j\varpi t}$, eliminating $\vec{H}$ between equations (2.1) and (2.2) and replacing the time derivatives with $j\varpi$
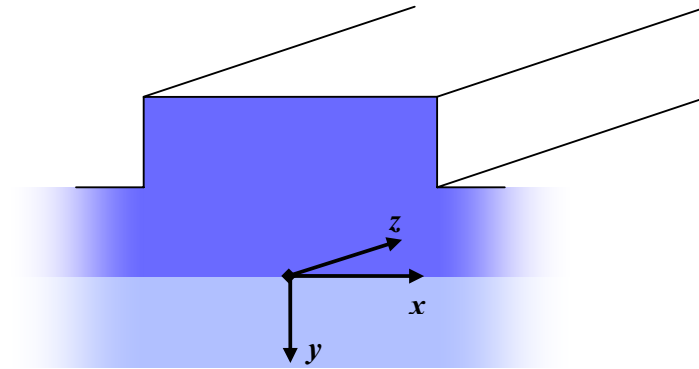
**Figure 2-2** Illustration of a typical rib waveguide geometry and reference co-ordinate system.

$$\nabla \times \nabla \times \underline{E} = k^2 \underline{E} \qquad (2.9)$$

where the local plane wave propagation constant or wavenumber, *k*, is given by

$$k = \omega \sqrt{\mu_0 \varepsilon} = \omega \sqrt{\mu_0 \varepsilon_0} \sqrt{\varepsilon_r} = \frac{2\pi}{\lambda} n(x, y)$$

and λ is the free space wavelength. Using the identities

$$\nabla \times \nabla \times = \nabla \nabla \cdot - \nabla^2$$
$$\nabla \cdot \left( n^2 \vec{E} \right) = n^2 \nabla \cdot \vec{E} + \vec{E} \cdot \nabla n^2 = 0 \qquad (2.10)$$

the general vector wave equation for the electric field is obtained

$$\nabla \cdot \vec{E} + \nabla \left( \frac{\vec{E} \cdot \nabla k^2}{k^2} \right) + k^2 \vec{E} = 0 \qquad (2.11)$$

The general vector wave equation for the magnetic field may be derived in a similar manner by eliminating $\vec{E}$ between equations (2.1) and (2.2) to obtain

$$\nabla^2 \vec{H} + k^2 \left( \nabla \cdot \frac{1}{\kappa^2} \right) \times \left( \nabla \times \vec{H} \right) + k^2 \vec{H} = 0 \qquad (2.12)$$

The geometry of the waveguide or an *a priori* knowledge of the nature of the fields supported by the guide may allow simplifications to be made to the full vector case, through the application of certain approximations. Considering waveguides that are longitudinally invariant in the direction of propagation, *z*, field solutions of the form

$$\vec{E} = E(x,y) e^{j(\omega t - \beta z)}, \quad \vec{H} = H(x,y) e^{j(\omega t - \beta z)} \qquad (2.13)$$

are sought. The simplification that $\dfrac{\partial n}{\partial z} = 0$ is introduced, as the refractive index distribution is now only a function of the coordinates *x* and *y*. The total field may now be derived from just the transverse component of the electric ($E_x$, $E_y$) or magnetic ($H_x$, $H_y$) fields. Therefore, for the electric field, equation (2.11) reduces to

$$\frac{\partial^2 E_x}{\partial x^2} + \frac{\partial^2 E_x}{\partial y^2} + \frac{\partial^2 E_x}{\partial z^2} + \frac{\partial}{\partial x}\left(\frac{1}{k^2} E_x \frac{\partial k^2}{\partial x}\right) + k^2 E_x = -\frac{\partial}{\partial x}\left(\frac{1}{k^2} E_y \frac{\partial k^2}{\partial y}\right) \quad (2.14)$$

or

$$\frac{\partial^2 E_y}{\partial x^2} + \frac{\partial^2 E_y}{\partial y^2} + \frac{\partial^2 E_y}{\partial z^2} + \frac{\partial}{\partial y}\left(\frac{1}{k^2} E_y \frac{\partial k^2}{\partial y}\right) + k^2 E_y = -\frac{\partial}{\partial y}\left(\frac{1}{k^2} E_x \frac{\partial k^2}{\partial x}\right) \quad (2.15)$$

and similarly for the magnetic field, equation (2.12) reduces to

$$\frac{\partial^2 H_x}{\partial x^2} + \frac{\partial^2 H_x}{\partial y^2} + \frac{\partial^2 H_x}{\partial z^2} + k^2 \frac{\partial}{\partial y}\left(\frac{1}{k^2}\right)\frac{\partial H_x}{\partial y} + k^2 H_x = -k^2 \frac{\partial}{\partial y}\left(\frac{1}{k^2}\right)\frac{\partial H_y}{\partial x} \quad (2.16)$$

or

$$\frac{\partial^2 H_y}{\partial x^2} + \frac{\partial^2 H_y}{\partial y^2} + \frac{\partial^2 H_y}{\partial z^2} + k^2 \frac{\partial}{\partial x}\left(\frac{1}{k^2}\right)\frac{\partial H_y}{\partial x} + k^2 H_y = -k^2 \frac{\partial}{\partial x}\left(\frac{1}{k^2}\right)\frac{\partial H_x}{\partial y} \quad (2.17)$$

The vector equations, (2.14)-(2.17), should then be solved, subject to the appropriate boundary conditions, dictated by the nature of the waveguide or requirements of the model to yield an eigenvalue problem that is generally solved for the propagation constant β. The approaches to solving these equations for the fields supported by the waveguide fall into one of three classes; (a) vectorial, (b) semi-vectorial or (c) scalar.

The solutions of the general vector equations, which provide the most accurate results, take into account all six field components. Solution for either the $\vec{E}$ field or $\vec{H}$ field can then be used to calculate the other via Maxwell's equations.

Semi-vectorial or polarised fields are five component solutions in which one transverse field component is assumed zero. The remaining transverse component, deemed the principal component, is used to classify the field either transverse electric (TE) or transverse magnetic (TM). In the TE case the component $E_x$ (or $H_y$) is non-zero and for TM the component $E_y$ (or $H_x$) is non-zero. Thus in this case the corresponding right hand sides of equations (2.14)-(2.17) become zero, effectively decoupling the polarisations, resulting in reduced equations for the principal field components. In the TE case the resulting wave equations are

$$\frac{\partial^2 E_x}{\partial x^2} + \frac{\partial^2 E_x}{\partial y^2} + \frac{\partial^2 E_x}{\partial z^2} + \frac{\partial}{\partial x}\left(\frac{1}{k^2} E_x \frac{\partial k^2}{\partial x}\right) + k^2 E_x = 0 \tag{2.18}$$

$$\frac{\partial^2 H_y}{\partial x^2} + \frac{\partial^2 H_y}{\partial y^2} + \frac{\partial^2 H_y}{\partial z^2} + k^2 \frac{\partial}{\partial x}\left(\frac{1}{k^2}\right)\frac{\partial H_y}{\partial x} + k^2 H_y = 0 \tag{2.19}$$

and likewise for the TM case

$$\frac{\partial^2 E_y}{\partial x^2} + \frac{\partial^2 E_y}{\partial y^2} + \frac{\partial^2 E_y}{\partial z^2} + \frac{\partial}{\partial y}\left(\frac{1}{k^2} E_y \frac{\partial k^2}{\partial y}\right) + k^2 E_y = 0 \tag{2.20}$$

$$\frac{\partial^2 H_x}{\partial x^2} + \frac{\partial^2 H_x}{\partial y^2} + \frac{\partial^2 H_x}{\partial z^2} + k^2 \frac{\partial}{\partial y}\left(\frac{1}{k^2}\right)\frac{\partial H_x}{\partial y} + k^2 H_x = 0 \tag{2.21}$$

In the scalar field solution no discrimination is made between the polarisations. The field equations are thus reduced to a pair of scalar Helmholtz equations

$$\left( \frac{\partial^2}{\partial x^2} + \frac{\partial^2}{\partial y^2} + \frac{\partial^2}{\partial z^2} \right) E + k^2 E = 0 \tag{2.22}$$

and

$$\left( \frac{\partial^2}{\partial x^2} + \frac{\partial^2}{\partial y^2} + \frac{\partial^2}{\partial z^2} \right) H + k^2 H = 0 \tag{2.23}$$

for the electric and magnetic fields respectively. The scalar approximation further requires that the field and its derivative are continuous throughout the solution space.

In structures of high refractive index contrast, significant coupling occurs between field polarisations and so the accurate modelling of these structures requires the solution of the full vector equations. In weakly guiding structures, i.e. those with low refractive index contrasts, the field components remain uncoupled and may be modelled using the semi-vectorial and scalar approximations.

In the case of the work presented here, which predominantly features air-clad rib waveguide structures with high refractive index contrasts between the guiding and cladding regions, the semi-vectorial approximation is successfully applied taking advantage of the relatively weak coupling of the field components that only take place in the rib region , [2.2], i.e. not general but for rib-like structures.

## 2.4   The wave equation – cylindrical coordinates

For a wave guiding system that contains circular boundaries or when dealing with fields that have cylindrical wavefronts it is advantageous to solve the wave equation in cylindrical coordinates, [2.7], where the conventional co-ordinate system has been dropped in favour of that depicted in order to maintain consistency with the rib geometry of figure 2-2. The following presents the derivation of the vector wave equation in cylindrical co-ordinates and its subsequent simplification to its polarised form.
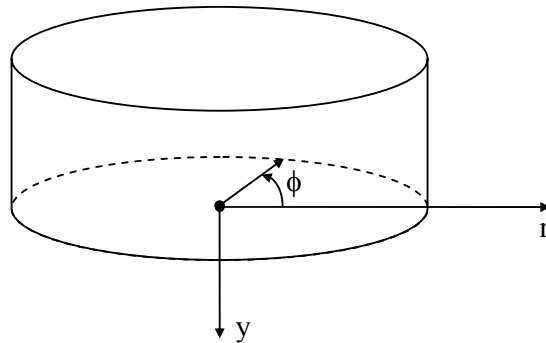
**Figure 2-3** Illustration of a dielectric disc and the reference coordinate system adopted in this work.

With reference to Figure 2-3, restating equation (2.11) in the form

$$\nabla^2 \vec{E} - \nabla\left(\nabla \cdot \vec{E}\right) + k^2 \vec{E} = 0 \qquad (2.24)$$

where

$$\nabla \cdot \vec{E} = \frac{-\vec{E}\nabla k^2}{k^2} = \frac{-\vec{E}\nabla n^2}{n^2} \tag{2.25}$$

has been used and n is the local refractive index. The terms in equation (2.24) may now be expressed in cylindrical coordinates as

$$\nabla^2 \vec{E} = \hat{r}\left(\nabla^2 E_r - \frac{2}{r^2}\frac{\partial E_\phi}{\partial \phi} - \frac{E_r}{r^2}\right) + \hat{\phi}\left(\nabla^2 E_\phi + \frac{2}{r^2}\frac{\partial E_r}{\partial \phi} - \frac{E_\phi}{r^2}\right) + \hat{y}\left(\nabla^2 E_y\right) \tag{2.26}$$

$$\nabla\left(\nabla \cdot \vec{E}\right) = \hat{r}\frac{\partial\left(\nabla \cdot \underline{E}\right)}{\partial r} + \hat{\phi}\frac{1}{r}\frac{\partial\left(\nabla \cdot \underline{E}\right)}{\partial \phi} + \hat{y}\frac{\partial\left(\nabla \cdot \underline{E}\right)}{\partial y} \tag{2.27}$$

$$\nabla \cdot \vec{E} = \frac{1}{r}\frac{\partial\left(rE_r\right)}{\partial r} + \frac{1}{r}\frac{\partial E_\phi}{\partial \phi} + \frac{\partial E_y}{\partial y} \tag{2.28}$$

through use of the Laplacian in cylindrical coordinates

$$\nabla^2 = \frac{1}{r}\frac{\partial}{\partial r}\left(r\frac{\partial f}{\partial r}\right) + \frac{1}{r^2}\frac{\partial^2 f}{\partial \phi^2} + \frac{\partial^2 f}{\partial y^2} \; .$$

Equations (2.3) and (2.5) give the condition

$$\nabla \cdot \left(n^2 \vec{E}\right) = 0 \tag{2.29}$$

The refractive index, n, is constant with respect to $\phi$ hence $\dfrac{\partial \left( n^2 \right)}{\partial \phi} = 0$. Applying this

condition to (2.29) gives

$$-\frac{1}{r}\frac{\partial E_\phi}{\partial \phi} = \frac{1}{n^2 r}\frac{\partial \left( rn^2 E_r \right)}{\partial r} + \frac{1}{n^2}\frac{\partial \left( n^2 E_y \right)}{\partial y} \tag{2.30}$$

and its subsequent substitution into (2.28) yields

$$\nabla \cdot \underline{E} = \frac{1}{r}\frac{\partial \left( rE_r \right)}{\partial r} + \frac{\partial E_y}{\partial y} - \frac{1}{n^2 r}\frac{\partial \left( rn^2 E_r \right)}{\partial r} - \frac{1}{n^2}\frac{\partial \left( n^2 E_y \right)}{\partial y} \tag{2.31}$$

Equations (2.26), (2.27) , (2.31) are now used to expand the wave equation (2.24)

into its component parts resulting in

$$
\begin{aligned}
&\hat{r}\left[ \nabla^2 E_r - \frac{2}{r^2}\frac{\partial E_\phi}{\partial \phi} - \frac{E_r}{r^2} - \frac{\partial}{\partial r}\left( \frac{1}{r}\frac{\partial \left( rE_r \right)}{\partial r} + \frac{1}{r}\frac{\partial E_\phi}{\partial \phi} + \frac{\partial E_y}{\partial y} \right) + k^2 E_r \right] \\
&\hat{\phi}\left[ \nabla^2 E_\phi + \frac{2}{r^2}\frac{\partial E_r}{\partial \phi} - \frac{E_\phi}{r^2} - \frac{1}{r}\frac{\partial}{\partial \phi}\left( \frac{1}{r}\frac{\partial \left( rE_r \right)}{\partial r} + \frac{1}{r}\frac{\partial E_\phi}{\partial \phi} + \frac{\partial E_y}{\partial y} \right) + k^2 E_\phi \right] = 0 \\
&\hat{y}\left[ \nabla^2 E_y - \frac{\partial}{\partial y}\left( \frac{1}{r}\frac{\partial \left( rE_r \right)}{\partial r} + \frac{1}{r}\frac{\partial E_\phi}{\partial \phi} + \frac{\partial E_y}{\partial y} \right) + k^2 E_y \right]
\end{aligned} \tag{2.32}
$$

For the TE like modes in the cylindrical case the principal field component is $E_r$ .In

order to find the corresponding semi-vectorial wave equation for propagating modes

of the form $e^{j(\omega t - v\phi)}$, where $v$ is the angular propagation constant, consider the $r$ component of (2.32)

$$\hat{r}\left[\nabla^2 E_r - \frac{2}{r^2}\frac{\partial E_\phi}{\partial \phi} - \frac{E_r}{r^2} - \frac{\partial}{\partial r}\left(\frac{1}{r}\frac{\partial(rE_r)}{\partial r} + \frac{1}{r}\frac{\partial E_\phi}{\partial \phi} + \frac{\partial E_y}{\partial y}\right) + k^2 E_r\right] = 0 \quad (2.33)$$

Using equation (2.30) and the Laplacian in cylindrical co-ordinates

$$\nabla^2\Psi = \frac{\partial^2\Psi}{\partial y^2} + \frac{\partial^2\Psi}{\partial r^2} + \frac{1}{r}\frac{\partial\Psi}{\partial r} - \frac{v^2}{r^2}\Psi \quad (2.34)$$

for a $\phi$ dependence $e^{-jv\phi}$, where $v$ is the angular propagation constant. Equation (2.33) may be re-written as

$$\begin{aligned}
0 = {} & \frac{\partial^2 E_r}{\partial y^2} + \frac{1}{r}\frac{\partial}{\partial r}\left(r\frac{\partial E_r}{\partial r}\right) + \frac{1}{r^2}\frac{\partial^2 E_y}{\partial \phi^2} + \frac{2}{r}\left(\frac{1}{n^2}\frac{\partial(n^2 E_r)}{\partial r} + \frac{E_r}{r} + \frac{1}{n^2}\frac{\partial(n^2 E_y)}{\partial y}\right) \\
& -\frac{E_r}{r^2} - \frac{\partial}{\partial r}\left(\frac{1}{r}\frac{\partial(rE_r)}{\partial r} - \frac{E_r}{r} + \frac{1}{n^2}\frac{\partial(n^2 E_r)}{\partial r} - \frac{1}{n^2}\frac{\partial(n^2 E_y)}{\partial y} + \frac{\partial E_y}{\partial y}\right) + \left(k^2 - \frac{v^2}{r^2}\right)E_r
\end{aligned} \quad (2.35)$$

Since the TE mode designation requires $E_y = 0$, equation (2.35) may be simplified to

$$\frac{v^2}{r^2}\Psi = \frac{\partial^2\Psi}{\partial y^2} + \frac{2}{n^2 r}\frac{\partial(n^2\Psi)}{\partial r} + r\frac{\partial}{\partial r}\frac{1}{n^2 r}\frac{\partial(n^2\Psi)}{\partial r} + k^2\Psi \quad (2.36)$$

where

$$\Psi = rE_r .$$ (2.37)

and similarly for TM modes, $E_r = 0$, thus

$$\frac{v^2}{r^2}E_y = \frac{\partial^2 E_y}{\partial r^2} + \frac{1}{r}\frac{\partial E_y}{\partial r} + \frac{\partial}{\partial y}\frac{1}{n^2}\frac{\partial\left(n^2 E_y\right)}{\partial y} + k^2 E_y$$ (2.38)

## 2.5 Waveguide Modes

The solutions of the previously developed wave equations yield the modal properties of the waveguide being analysed. Open optical waveguides, such as the air clad rib waveguide, support modes which may be considered in two classes; a discrete set of bound modes and a continuum of radiation modes that come together to form a complete set of functions describing the properties of the waveguide, [2.8].

Consider the simple case of the asymmetric 3-layer slab waveguide illustrated in figure 2-5, where $n_{core} > n_{substrate} > n_{cladding}$. The discrete set of bound modes are characterised by propagation constants, $\beta$, that are purely real and lie within the range $n_{core}k_0 < \beta < n_{substrate}k_0$. These modes are oscillatory within the core region and exponentially decay in the substrate and cladding regions, figure 2-5(a).
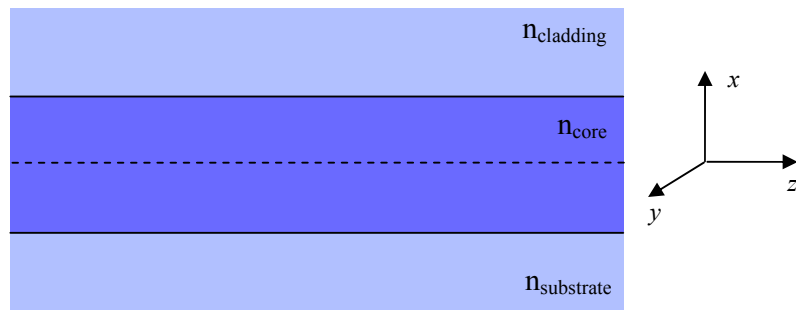
**figure 2-4** 3-layer dielectric slab waveguide.
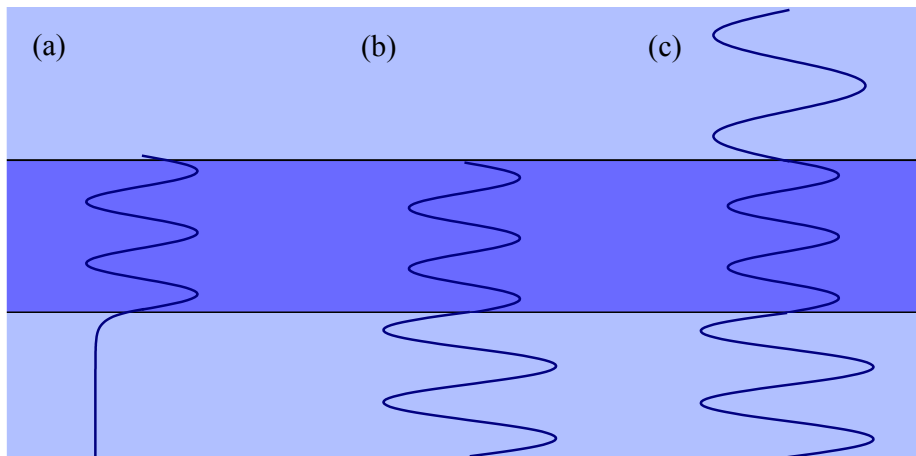


**figure 2-5** Illustration of the modes supported by a 3-layer asymmetric slab waveguide; (a) guided mode, (b) substrate radiation mode and (c) substrate-cladding radiation mode.

The total radiation field is comprised of radiation modes and leaky modes. Radiation modes are characterised by propagation constants below the cut-off for bound modes i.e. $0 < \beta < \mathrm{n}_{cladding} k_0$. These are illustrated in figure 2-5 (b) and (c) for the cases of

26

substrate radiation modes, $n_{cladding}k_0 < \beta < n_{substrate}k_0$ and cladding-substrate radiation modes, $0 < \beta < n_{cladding}k_0$, respectively. Leaky modes are characterised by discrete solutions that yield complex propagation constants below cut off which lose power into the cladding as they propagate. These solutions are non-physical as the boundary conditions at infinity, $E = 0$, are not satisfied, but they serve to describe physically consistent characteristics that are further explored in chapters 5 and 6 as they apply to the lossy systems considered.

### 2.5.1 Bound Mode Classification

Throughout this work solutions are sought to the polarised wave equation under the approximation (in a rectangular co-ordinate system) that the field components $E_x$ and $E_y$ remain uncoupled. Two polarisations may then be defined in terms of the principal electric field component, $E_x$ or $E_y$, figure 2-6. Quasi-TE (Transverse Electric) modes,[2.9], which are defined by the experimentally observed polarisation such that

$$\vec{E}(x,y,z) \equiv (E_x, 0, E_z) \tag{2.39}$$

where

$$E_x \gg E_z$$

and Quasi-TM (Transverse Magnetic) modes are similarly defined by the observed polarisation such that

$$\vec{E}(x, y, z) \equiv \left(0, E_y, E_z\right) \tag{2.40}$$

where

$$E_y \gg E_z$$

(a)                                                    (b)



**figure 2-6** Principal electric field components for the (a) quasi-TE mode and (b) quasi-TM mode.

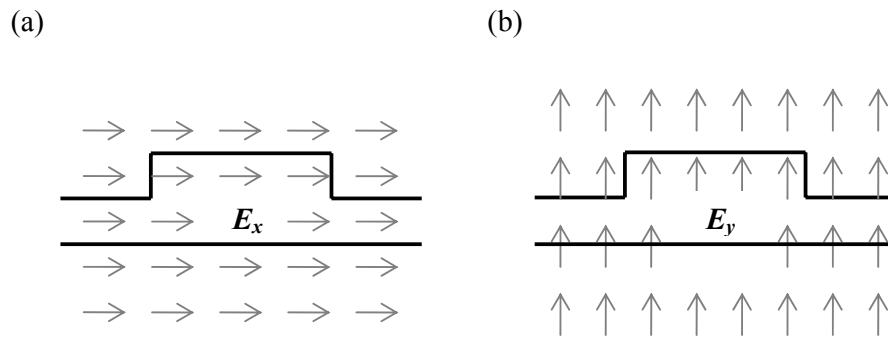## 2.6   The Goos-Hänchen Shift and the Method of False Position

Air-clad optical waveguides are, in general, open structures which may support modes that are unbounded in the plane of the cross-section. This results in an optical field that is not entirely confined to a finite region but one that extends to infinity.

The open waveguide may support a finite number of discrete bound modes, together with a continuum of modes. The analysis of truly open waveguides becomes increasingly complex as the complexity of the waveguide increases; e.g. slab waveguide to rib waveguide etc., and generally analytical solutions to these waveguides do not exist.

In this work advantage is taken of the fact that air-clad optical waveguides with high core/cladding refractive index contrasts may, due to the rapidly decaying field in the cladding region, be approximated by a partially closed system. The closed system results in one that is far less complex and time consuming to analyse without significant loss in accuracy. The approximation requires the imposition of an $E=0$ condition along a suitably modified core/cladding interface. Considering the case of the 3-layer symmetric slab waveguide, figure 2-7, it is well known that rays travelling along the waveguide are not immediately reflected at the core cladding interface but penetrate a small distance into the cladding region before being reflected. This penetration into the cladding effectively widens the waveguide by an amount $2\Delta W$ and further results in a lateral displacement of the reflected ray from the incident ray by an amount $\Delta z$, the Goos-Hänchen shift [2.10] .

For large core/cladding refractive index contrasts, the field penetration depth becomes small and the approximation that $E = 0$ along the boundary $|x| = W + \Delta W$ is justified as the difference between the true field and the approximated field becomes negligible. The slab waveguide may now be replaced by its metal clad equivalent,

simplifying its analysis. This approach is fundamental to the analysis method used as a basis throughout this work, which is discussed in detail in chapter 3.
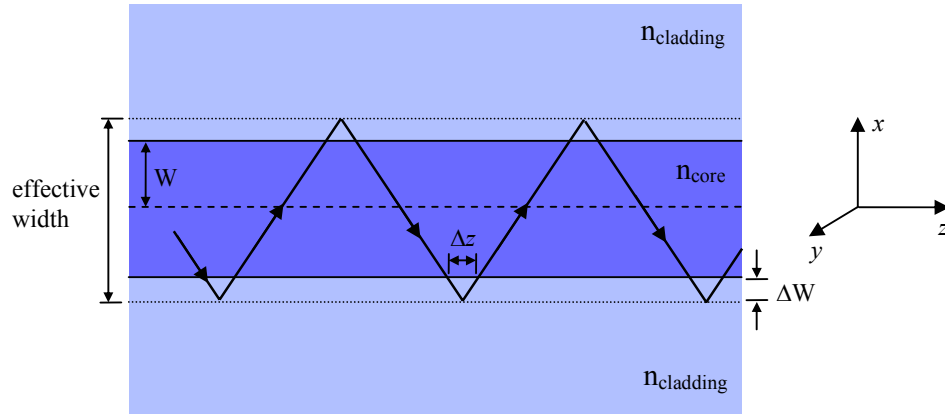


**figure 2-7** Ray diagram of a 3-layer slab waveguide illustrating the Goos Hänchen shift, $\Delta z$.

The amount by which the physical boundary is displaced is dependant upon the polarisation of the field component of interest, with respect to the boundary, [2.2]. In the case where the field component is incident normal to the interface the displacement $\Delta_n$ is given by

$$\Delta_n = \frac{\left(n_{cladding}\right)^2}{\left(n_{core}\right)^2} \frac{1}{\left(\beta^2 - k_1^2\right)^{\frac{1}{2}}}$$

(2.41)

where

$$k_1^2 = n_{cladding}^2 k_0^2 ,$$

$$k_0 = \frac{2\pi}{\lambda}$$

and $\beta$ is the propagation constant. For a field component tangential to the interface the displacement $\Delta_t$ is given by

$$\Delta_t = \frac{1}{\left(\beta^2 - k_1^2\right)^{1/2}} \tag{2.42}$$

## 2.7  The Variational Method

Fundamental to the formulation of the Spectral Index method is the application of a variational method. The variational approach seeks to minimise the error between the true field and the field obtained through application of a trial function. Consider the eigenvalue problem such that

$$L\Psi = \lambda\Psi \tag{2.43}$$

where $L$ is a linear operator, $\Psi$ is an eigenfunction and $\lambda$ the associated eigenvalue. The variational method seek to identify a function $\Phi(\lambda)$, that maybe either scalar or vectorial, which is subject to the same boundary conditions as $\Psi$ that in turn corresponds to a stationary value of $\Psi$.

Variational formulations have been applied to the analysis of optical waveguides, [2.3]-[2.4] and are used in Finite Element formulations, discussed in (§2.8.2). By in large the variational formulations that have been obtained have been so through a process of trial and error or through the application of general principles, [2.5].

Variational formulations form a basis from which approximate, but nevertheless accurate, solutions to practical problems that may otherwise prove to be extremely difficult, [2.6].

In the case of the SI method the variational expression is developed from the scalar wave equation in order to obtain a simple boundary condition, the exact nature of the expression and resulting boundary condition is introduced in the next chapter, (§3.6)

## 2.8 Analysis Methods – An Introduction

Efficient and accurate analysis methods are essential tools in the design and optimisation of optical waveguide based technologies. From simply determining the optical characteristics of simple waveguide structures figure 2-8, to the characterisation of more complex optical circuits, figure 2-9, computational techniques lend themselves extremely well to the design process. The boundaries of CAD software are continually being pushed forward by the industry's demand for greater complexity, higher accuracy and increased efficiency.
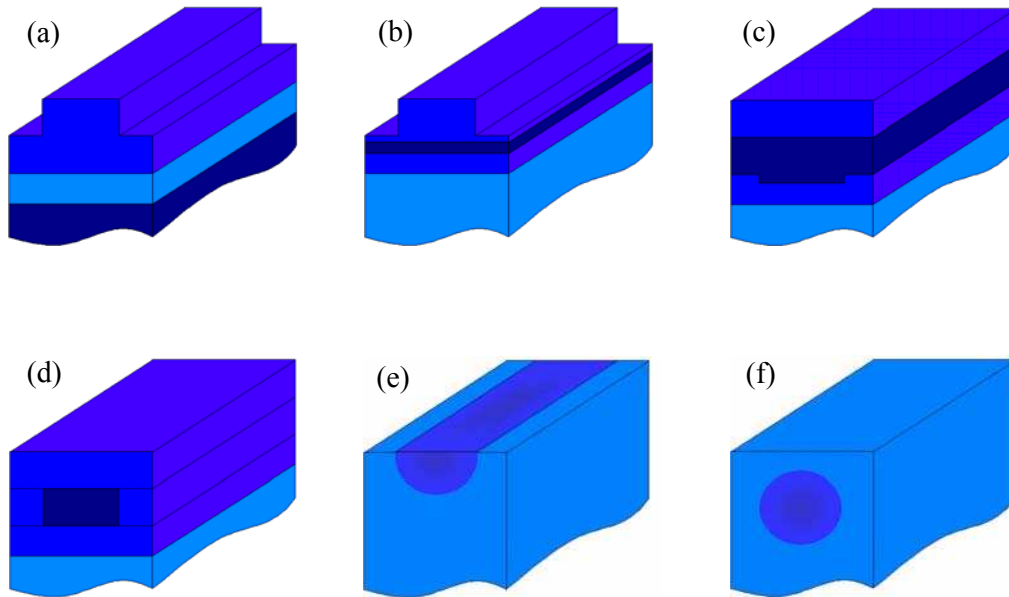
**figure 2-8** Schematic illustration of some common dielectric waveguiding structures; (a) rib waveguide, (b) strip-loaded rib waveguide, (c) buried rib waveguide, (d) buried strip waveguide, (e) diffused waveguide and (f) buried diffused waveguide.
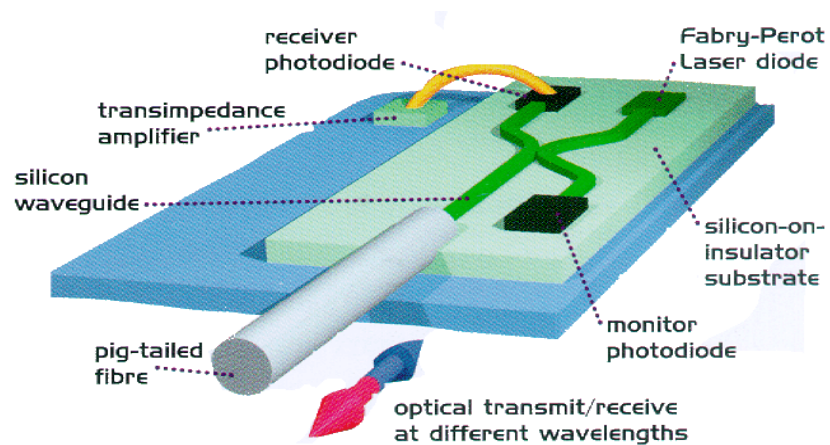


**figure 2-9** Illustration of an integrated optical transceiver (Image © Bookham Technology).

The methods employed by CAD software can be considered to fall into one of three categories; numerical, semi-analytical and analytical. As eluded to in chapter 1, analytical methods are unsuitable for the analysis of all but the simplest of structures. The following will therefore concentrate on numerical and semi-analytical approaches and introduce the more common methods used in the solution of Maxwell's equation for the analysis of optical wave-guiding structures.

### 2.8.1 The Finite Difference Method

The finite difference (FD) method, [2.11], is a numerical technique and one of the most frequently applied analysis techniques, [2.12]. The FD method discretises the problem domain by way of a rectangular mesh of points, figure 2-10(a). The discretisation of the problem space maybe uniform or variable, the latter used to improve accuracy by say allocating a finer mesh to small features and a coarser mesh to larger features of a structure, figure 2-10(b). The wave equation in either its scalar, semi-vectorial or vector form is then solved at each of the mesh points or nodes. These nodes may be chosen to either lie at the mesh points, figure 2-10(c), or at the centre of each cell, figure 2-10(d). Application of the correct boundary conditions at the mesh interfaces and discretisation of the wave equation results in an eigenvalue equation. The solution of the resulting eigenvalue equation may then be obtained via an iterative method or through the application of a sparse matrix routine. Also, as the open structures must be boxed for analysis, hence only a finite domain can be studied, the successful implementation of the FD method requires careful

consideration of the problem domain boundaries so they do not adversely affect the true field.

Also as an orthogonal mesh is employed, structures with physical features that lie obliquely to the mesh require the approximation of those features through use of a staircase approximation, figure 2-10(e). This stair-casing results in the introduction of artificial dielectric corners resulting in a series of sharp field peaks along the staircase and as a result poor convergence and accuracy may be observed. This problem has been addressed with more recent work utilising structure-related (SR) co-ordinate systems, figure 2-10(f), such as that described in [2.22]. These allow the physical boundaries to be modelled exactly, thus overcoming the restrictions introduced by stair-casing.

The relative ease of application of the method, together with its generality, maintains the popularity of the method. Difficulty arises though when considering large structures and those close to cut off, requiring large and/or dense meshes. The possibility of complex eigenvalues results in an additional level of complexity. Both of the aforementioned problems increase the computational requirements of the method in terms of both time and memory.

## 2.8.2 The Finite Element Method

The finite element (FE) method, [2.13] is another numerical method that discretises the problem domain. Here the domain is normally discretised into a set of
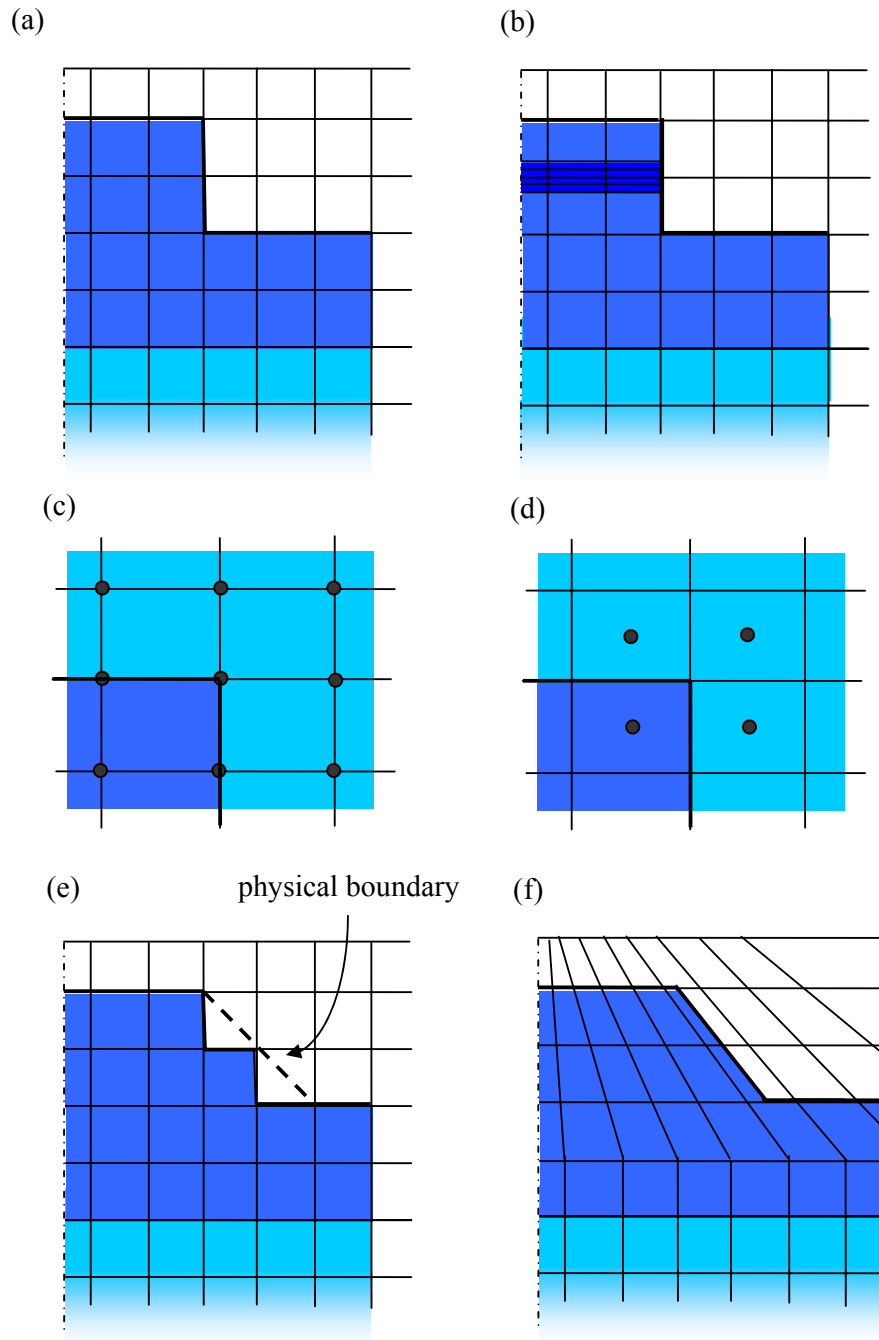
**figure 2-10** Finite difference discretisation schemes; (a) uniform orthogonal mesh, (b) non-uniform orthogonal mesh. Location of node points; (c) at mesh points, (d) at centre of cell, (e) staircased approximation to an oblique boundary, and (e) structure related co-ordinate system..

adjoining triangular elements, figure 2-11(b), although other geometric elements maybe used, such as rectangular that may provide for more accurate solutions when considering complex structures, [2.14]. This discretisation approach allows the standard method to more faithfully model arbitrary shapes. The field at the nodes of the triangles is then represented using interpolating polynomials and, through application of a variational principle, [2.15], a final eigenvalue equation can be formed.

Again the method requires that open structures are boxed and a suitable boundary condition employed so as not to affect the true field. As with the FD method, for higher accuracy a denser mesh is required and the computational overheads increase.

(a)                                          (b)

true boundary

staircased approximation
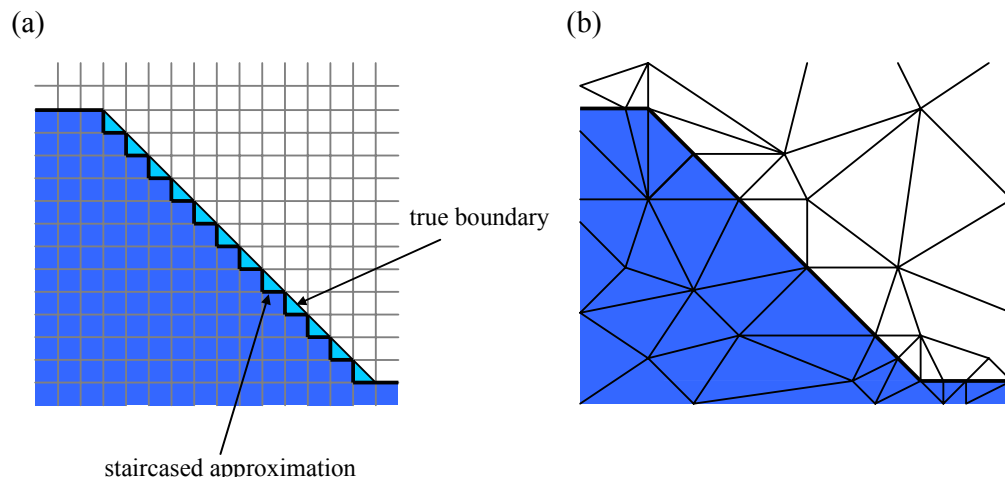
**figure 2-11** Discretisation of an oblique walled rib waveguide; (a) FD staircase approximation to true boundary and (b) FE representation using a triangular mesh.

### 2.8.3  Finite Difference Beam Propagation Method

The finite difference beam propagation method (FD-BPM), [2.16]-[2.17], is the one of the most widely employed techniques for the analysis of propagation characteristics of optical systems. In its earliest formulation FD-BPM solved the scalar, paraxial wave equation and in later work has been extended to the vectorial case in order to accurately account for polarisation effects through solution of the vector wave equation, [2.18]. In its paraxial form the FD-BPM method precludes the analysis of structures with high index contrasts in the direction of propagation. The method also suffered in terms of accuracy when applied to structures with a large phase variation in the direction of propagation and those structures that rely on reflection for their operation. These issues have more recently been overcome through the development of wide-angle-BPM, [2.19], and bidirectional-BPM, [2.20]. More recently the introduction of structure dependent coordinate systems has improved the flexibility of the method, [2.21]-[2.22].

Computational times, as with the previous methods, suffer from the needs of increased accuracy and complexity of the problem domain. Again the open domain requires truncation with a suitable boundary condition so the accuracy of the solution is not compromised. Traditionally absorbing boundary conditions (ABC), [2.23], were employed, whereby reflections at the boundary of the domain are absorbed. ABCs are heavily problem specific and a more efficient approach, that of the transparent boundary condition (TBC), [2.24], was introduced, which allows outgoing waves to pass thus reducing unwanted reflections. More recently, perfectly

matched layers (PML), [2.25], have been employed with higher efficiency than the previous approaches. PMLs introduce a false layer that totally eliminates unwanted reflections at the imposed domain boundary.

### 2.8.4  The Mode Matching Method

The mode matching (MM) method, [2.26], is a semi-analytical technique that has been used for the analysis of composite waveguide structures. The structure is broken down into constituent elements and the fields in these elements described expanded as a complete set of modes. The elements are then brought back together by enforcing the expansion to obey the necessary boundary conditions at the interfaces of the elements. The method has been successfully used in the work described in chapter 8 in a modular approach to optical circuit analysis. This approach is similar in formulation to that encountered in transmission line theory and so the MM method is often referred to as an equivalent-network method. Open domains again require boxing and a discrete representation of the radiation field is so obtained. The speed/accuracy of the method is ultimately determined by the number of modes used in the total field expansion.

### 2.8.5  The Effective index Method

Offered as an improvement to the method of Marcatilli, [2.27], the effective index (EI) method, [2.28], represents a structure as a combination of slab waveguides, figure 2-12. The solution of the transcendental equations for the slab waveguides yeild the effective refractive indices, $n_{eff,}$ of each slab. The effective indices of each

slab are then used to provide a final slab whose resulting effective index yields the propagation constants of the original structure. Because of its reliance of the outer slab regions to provide effective indices the method becomes in accurate when these regions are close to cut-off or support no modes, [2.29]. Due to its simplicity the method has found wide application and has undergone several extensions in order to increase it accuracy, [2.30]-[2.33].
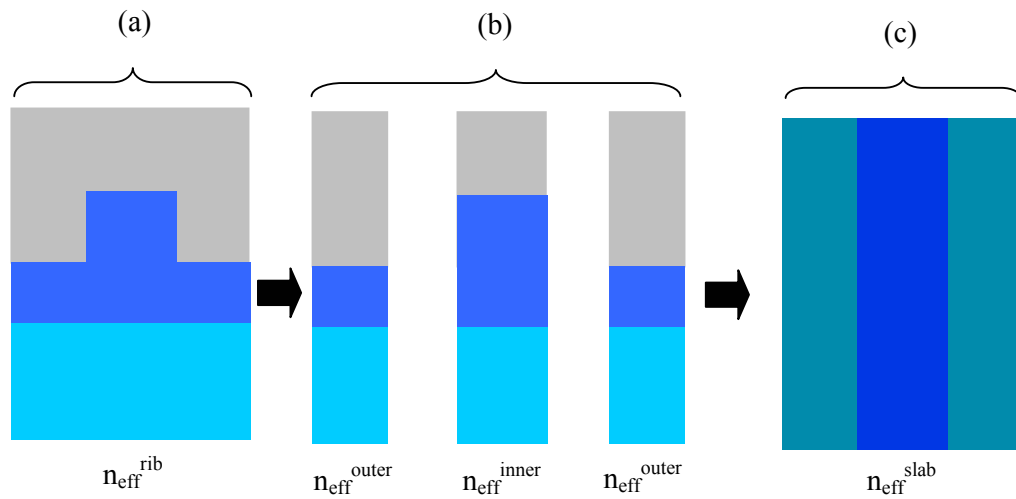


**figure 2-12** Effective index representation for a slab waveguide where $n_{eff}^{rib}$ is equivalent to $n_{eff}^{slab}$; (a) physical structure, (b) separation into distinct slab regions and (c) slab representation of the original structure.

## 2.9   Conclusion

This chapter has introduced the fundamentals of electromagnetic theory as applicable to the analysis of optical waveguide structures composed of non-magnetic media in a source free environment. The wave equations, through consideration of the appropriate boundary conditions have been derived in both Cartesian and cylindrical coordinates.

A brief overview of some of the more common numerical and semi-techniques applied to the solution of the wave equations was then given with an emphasis placed on introducing those methods that are discussed in later chapters. For an introduction to other techniques that are out of context with the work presented in this thesis and reader is referred to references [2.34]-[2.36] and [2.12]. Of the techniques introduced, the numerical methods, whilst being the most widely applicable and looked upon as providing benchmark results, suffer when considering large problem domains. The computational requirements of the methods then become prohibitive, requiring long run times on state-of-the-art workstations. Alternatively semi-analytical approaches can be extremely fast and efficient and of sufficient accuracy to allow their use in an iterative design environment. But these method suffer in terms of generality and for the most part need to be formulated with specific materials or geometries in mind.

## 2.10 References

[2.1]   R. F. Harrington, "Time harmonic electromagnetic fields", Mc-Graw Hill, 1961.

[2.2]   P. N. Robson, and P. C. Kendall (Ed.), "Rib Waveguide Theory by the Spectral Index Method", Chapter 4, Research Studies Press, 1990.

[2.3]   W. P. Huang, and S. K. Chaudhuri, "Variational coupled mode theory of optical couplers", IEEE Journal of Lightwave Technology, vol. 8(10), pp. 1565-1570, 1990.

[2.4]   W. P. Huang, and H. A. Haus, "A simple variational approach to optical rib waveguides", IEEE Journal of Lightwave Technology, vol. 9(10), pp. 56-61, 1991.

[2.5]   Morse and Feshback, "Methods of theoretical Physics Part I & II, McGraw-Hill, 1953.

[2.6]   J. N. Reddy, "Applied functional analysis and variational methods in engineering", McGraw-Hill,1986.

[2.7]   S. Ramo, J. R. Whinnery, T. Van Duzer, "Fields and waves in communication electronics", John Wiley & Sons, 1993.

[2.8]   T. Rozzi, M, Mongiardo, "Open electromagnetic waveguides", The IEE, 1997.

[2.9]   M. S. Stern, "Semi-vectorial polarised finite difference method for optical waveguides with arbitrary index profiles", IEE proc. J, vol. 135, pp. 56-63, 1988.

[2.10]  T. Tamir, "Guided-wave optoelectronics", Springer-Verlag, 1990.

[2.11] M. S. Stern, "Finite difference analysis of planar optical waveguides", Chapter 4, PIER 10, partI, EMW publishing, 1995.

[2.12] R. Scarmozzino, "Numerical techniques for modeling guided-wave photonic devices", IEEE Journal of Lightwave Technology, vol. 6(1), pp.150-162, 2000.

[2.13] B. M. A. Rahman, "Finite element analysis of optical waveguides", Chapter 5, PIER 10, partI, EMW publishing, 1995.

[2.14] N. K. Uzunoglu, K. S. Nikita, and D. I. Kaklamani (Eds.), "Applied computational electromagnetics: State of the art and future trends", Springer-Verlag, 1998.

[2.15] A. J. Davies: 'The finite element method: A first approach' Oxford University Press, 1980, 1986.

[2.16] M. D. Feit, and J. A. Fleck, "Light propagation in graded-index optical fibers", Applied Optics, vol. 17, pp.3990-3998.

[2.17] C. L. Xu, and W. P. Huang, "Finite-difference beam propagation method for guided-wave optics", Chapter 1, PIER 11, partII, EMW publishing, 1995.

[2.18] W. P. Haung, C. L. Xu, "Simulation of three-dimensional optical waveguides by a full vector beam propagation method", Journal of Quantum Electronics, vol. 29, pp. 2639-2649, 1993.

[2.19] G. R. Hadley, "Wide-angle beam propagation using Pade approximant operators", Optoelectronics Letters, vol. 17, pp. 1426-, 1992.

[2.20] H. Rao, R. Scarmozzino, and R. M. Osgood Jr., "A bidirectional beam propagation method for multiple dielectric interfaces", Photonics Technology Letters, vol. 11, pp. 830-832, 1999.

[2.21]  T. M. Benson, P. Sewell, S. Sujecki, and P. C. Kendall, "Structure related beam propagation", Optical and Quantum Electronics, vol. 31, pp. 689-703, 1999.

[2.22]  D. Z. Djurdjevic, P. Sewell, T. M. Benson, and A. Vukovic, "Highly efficient finite-difference schemes for structures of non-rectangular cross section", Microwave and Optical Technology Letters, vol. 33, pp.401-407, 2002.

[2.23]  P. E. Lagasse, R. Baets, "Application of propagating beam methods to electromagnetic and acoustic wave propagation problems: a review", Radio Sci., 22, pp.1225-1233, 1987.

[2.24]  R. G. Hadley, "Transparent boundary condition for beam propagation methods", Opt. Lett., 16, pp.624-626, 1991.

[2.25]  W. P. Huang, C. L. Xu, L. Yokoyama, "The perfectly matched layer (PML) boundary condition for the Beam Propagation Method", IEEE Photonics Technology Letters, vol. 8, pp.649-651, 1996.

[2.26]  R. E. Collin, "The field Theory of Guided Waves", IEEE Press, Chapter 8, 1991.

[2.27]  E. A. J. Marcatili, "Dielectric rectangular waveguide and directional coupler for integrated optics", Bell Syst. Tech. J., 48, pp.2071-2102, 1969.

[2.28]  R. M. Knox, and P. P. Toulios, "Integrated circuits for the millimeter through optical frequency range", Proc. M.R.I. Symp. Submillimeter waves, Fox J., Ed. Brooklyn, N.Y.: Polytechnic Press, pp.497-516, 1970.

[2.29]  K. S. Chiang, "Review of numerical and approximate methods fort he analysis of general optical dielectric waveguides", Optical and Quantum Electronics, 26, pp.S113-S134, 1994.

[2.30] K. S. Chiang, "Dual Effective Index method for the analysis of rectangular dielectric waveguides", Applied Optics, 25, pp.2169-2174, 1986.

[2.31] J. J. G. M. Van Der Tol, N. H. G. Baken, "Correction to Effective Index method for rectangular dielectric waveguides", Electronics Letters, 24, pp.207-208, 1988.

[2.32] K. S. Chiang, "Analysis of rectangular dielectric waveguides: Effective-Index method with built-in pertubation correction", Electronics Letters, 28, pp.388-390, 1992.

[2.33] T. M. Benson, R. J. Bozeat, P. C. Kendall, "Rigorous EI method for semiconductor optical rib waveguides", IEE Proc. J., 139, pp.67-70, 1992.

[2.34] W. P. Huang, (Ed), "Methods for modeling and simulation of guided wave optoelectronic devices: Part I: Modes and couplings", EMW, 1995.

[2.35] W. P. Huang, (Ed), "Methods for modeling and simulation of guided wave optoelectronic devices: Part II: Waves and interactions", EMW, 1995.

[2.36] C. Vassallo, "1993-1995 Optical mode solvers", Optical and Quantum Electronics, vol. 29, pp. 95-114, 1997.

# Chapter 3 The Spectral Index Method

The Spectral Index (SI) method forms the basis from which the work described in this thesis was developed. The SI method has traditionally been applied to the analysis of rectangular semi-conductor rib waveguides, [3.1]-[3.8], and was subsequently used to analyse multiple rib waveguide structures, [3.9]-[3.10]. Further developments led to its successful application to the analysis rib waveguide based spot-size transformers, [3.11], a subject that is given extensive coverage in chapter 4. The accuracy of the technique has also been enhanced through inclusion of the singular nature of the field at dielectric corners, [3.12]. Throughout this work the SI method is extended for the first time to the case of non-rectangular cross sections, circular geometries and three dimensional waveguide problems. In all these cases the basic underlying principles remain the same. Therefore this chapter covers, in detail, the philosophy and concepts of the SI approach to the analysis of semiconductor waveguide structures in the context of the three-layer rectangular rib waveguide, figure 3-1. Comparisons will be drawn with results from other methods where necessary indicating the advantages of the SI approach, or the method's short-comings, as appropriate.

## 3.1 The SI method – an overview

The SI method begins by modifying the physical semiconductor-air boundary in the transverse plane of the waveguide by replacing that boundary with a polarisation

dependant evanescent boundary, upon which the field is set to zero. Exact solutions to the scalar wave equation are then formulated in the upper guiding or rib region and the underlying substrate region of the waveguide. These solutions are then matched along the boundary of the two regions using a variational principle to give a simple transcendental eigenvalue equation for the longitudinal propagation constant, β.
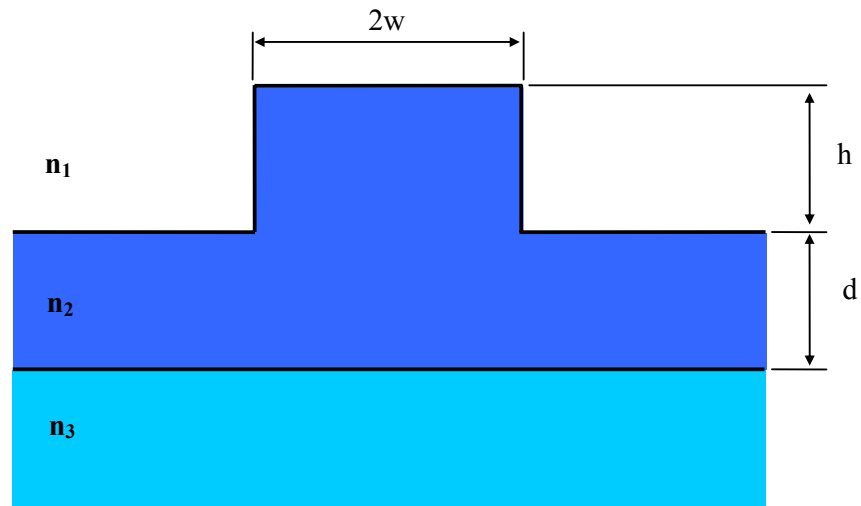


**Figure 3-1** Transverse cross section of a three-layer semiconductor rib waveguide, where $n_2 > n_3 > n_1$.

## 3.2  Theory

The SI method solves the two dimensional Helmholtz wave equation

$$\frac{\partial^2 E}{\partial x^2} + \frac{\partial^2 E}{\partial y^2} + \left[ k^2(x,y) - \beta^2 \right] E = 0 \qquad (3.1)$$

where $E(x, y, z) = E(x, y)e^{-j\beta z}$, $E(x, y)$ being the principal polarised electric field profile. $\beta$ is the longitudinal propagation constant and $k(x, y) = k_0 n(x, y)$, where $k_0$ is the free space wavenumber $\frac{2\pi}{\lambda}$ and $n(x, y)$ is the transverse refractive index profile.

## 3.3 The effective structure

As previously stated the SI method replaces the physical rib structure with an effective structure, whereby the structures physical boundary is displaced and the field set to zero along the effective boundary. This principle of effective penetration depths, as introduced in chapter 2, models the penetration of the optical field into the cladding and is most accurate when the penetration is small as is the case for air clad waveguides. For example air-clad III-V semiconductor based structures have a refractive index step, at the air/semiconductor boundary of approximately 1:3.

Figure 3-2(a) illustrates the simple case of the 3-layer rib waveguide of width $2w$, rib etch depth h and outer slab depth d. The refractive indices are such that $n_2 > n_3 \gg n_1$. Imposition of the effective penetration depths results in a rib that is slightly larger that the physical rib, Figure 3-2(b), whose effective dimension are width 2W, etch depth H and outer slab depth D. The effective dimensions are polarisation dependant and are given by

$$W = w + \Delta_n, \quad D = d + \Delta_t, \quad H = h \quad\quad (3.2)$$

for the case of TE polarisation and

$$W = w + \Delta_t, \qquad D = d + \Delta_n, \qquad H = h \tag{3.3}$$

for the case of TM polarisation, where

$$\Delta_t = \left(\beta^2 - k_1^2\right)^{-\frac{1}{2}} \qquad \text{and} \qquad \Delta_n = \left(\frac{n_1}{n_2}\right)^2 . \Delta_t \tag{3.4}$$

$\Delta_t$ and $\Delta_n$ correspond to the effective penetration depths of the tangential and normal electric field components respectively. Figure 3-2 also serves to illustrate the coordinate system adopted and the boundary between the upper rib region, $\Omega_1$ $(0 < y < H)$, and the underlying substrate region $\Omega_2$ $(y > 0)$.

(a)          (b)
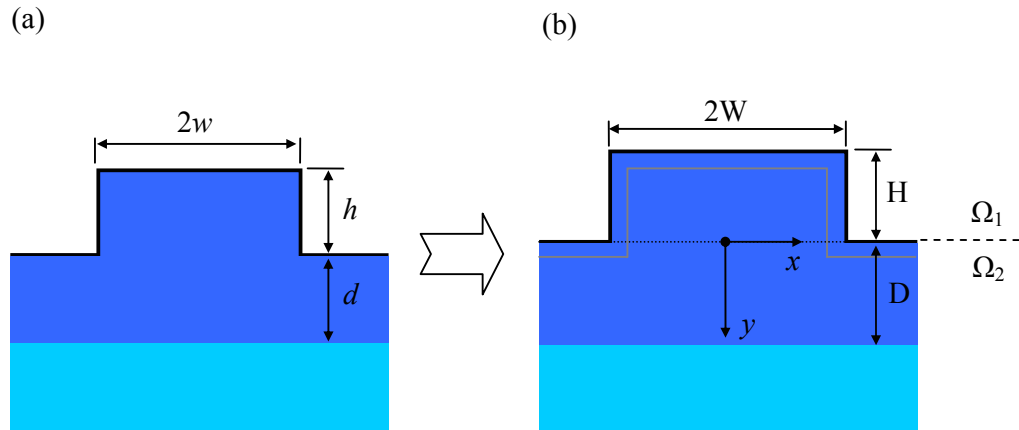


**Figure 3-2** Application of the method of effective penetration depths to a 3-layer rib waveguide illustrating; (a) physical structure and (b) effective structure together with coordinate system adopted and boundary at *y*=0.

Application of the effective structure renders equation (3.1) separable in regions $\Omega_1$

and $\Omega_2$ which greatly simplifies the analysis.

## 3.4   Field Distribution in Region $\Omega_1$

The field in region $\Omega_1$ may in general be written as a separable solution for $E$ such

that

$$E = \sum_{m=1}^{N} F_M(x) G_M(y) \tag{3.5}$$

The lateral field distribution, $F_M(x)$, may then be described by a Fourier series. It

has been shown, [3.3], that unless the mode sought is close to cut-off only the first

term of the Fourier series is necessary for accurate representation of the field within

the rib and so (3.5) may be simplified to

$$E = F(x) G(y) \tag{3.6}$$

The lateral field distribution may then be written as either

$$F(x) = \cos(s_1 x), \; s_1 = \frac{\pi}{2W} \tag{3.7}$$

for the fundamental symmetric mode or

$$F(x) = \sin(s_2 x), \; s_2 = \pi \big/ W \tag{3.8}$$

for the fundamental asymmetric mode. The corresponding functions describing the vertical field distribution, $G(y)$, are then given by

$$G(y) = \frac{\sin(\gamma_{1,2}(y+H))}{\sin(\gamma_{1,2}H)} \tag{3.9}$$

where

$$\gamma_{1,2} = \left(k_2^2 - s_{1,2}^2 - \beta^2\right)^{1/2} \tag{3.10}$$

For clarity the following discussion will be restricted to the fundamental symmetric mode. Thus the field in the rib region is totally described by

$$E = \cos(s_1 x)\frac{\sin(\gamma_1(y+H))}{\sin(\gamma_1 H)} \tag{3.11}$$

## 3.5 Field Distribution in Region $\Omega_2$

In region $\Omega_2$, the multi-layered substrate below the rib, a Fourier transform of $E$ is used to reduce the dimensionality of the wave equation, (3.1), yielding

$$\frac{\partial^2 \phi(s,y)}{\partial y^2} + \left\{ k^2(y) - s^2 - \beta^2 \right\} \phi(s,y) = 0 \tag{3.12}$$

where use has been made of the transform pair

$$\phi(s,y) = \int_{-\infty}^{+\infty} E(x,y)e^{-jsx}dx \quad \text{and} \quad E(x,y) = \frac{1}{2\pi}\int_{-\infty}^{+\infty} \phi(s,y)e^{jsx}ds \tag{3.13}$$

Comparing (3.12) to the equation of a slab waveguide whose layers have refractive indices, $n_i$

$$\frac{\partial^2 E_x}{\partial y^2} + \left( k_0^2 n_i^2 - \beta^2 \right) E_x = 0 \tag{3.14}$$

it is seen that (3.12) is of the same form as (3.14), but with 'spectral refractive indices' given by

$$n_s = \left( n^2 - \frac{s^2}{k_0^2} \right)^{1/2} \tag{3.15}$$

and so may be solved in a similar manner. Thus the original problem has been reduced in dimensionality and is now far easier to solve in term of computational effort. The solution of (3.12) is now written as

$$\phi(s,y) = f(s)g(s,y) \tag{3.16}$$

where

$$f(s) = \int_{-\infty}^{\infty} F(x) e^{-jsx} = \frac{2s_1 \cos(sW)}{s_1^2 - s^2} \tag{3.17}$$

$$g(s,y) = A \sin\{\Gamma_2(y-D)\} + B \cos\{\Gamma_2(y-D)\} \qquad (0 < y \leq D)$$
$$g(s,y) = C \exp\{-\Gamma_3(y-D)\} \qquad (y > D) \tag{3.18}$$

and

$$\Gamma_2 = \left(k_2^2 - \beta^2 - s^2\right)^{\frac{1}{2}}$$
$$\Gamma_3 = \left(\beta^2 + s^2 - k_3^2\right)^{\frac{1}{2}} \tag{3.19}$$

These expressions apply for both quasi-TE and quasi-TM modes if, for quasi-TM modes, $\Gamma_3$ is multiplied by the pre-factor

$$m_1 = \frac{k_2^2}{k_3^2} \tag{3.20}$$

## 3.6   The Variational Boundary Condition

The definitions of $f(s)$ and $g(s,y)$ ensure field continuity across $y = 0$ is achieved, but as a consequence the derivative of the field is discontinuous at $y = 0$. Maxwell's equations in a source free system are thus not satisfied along this boundary as a discontinuity in the field or its derivative would imply an energy storage mechanism and hence a source of energy. A variational technique is therefore employed which seeks to minimises the difference in the derivative of the

field across the boundary through varying the trial functions for the field. In the case of the rib waveguide the variational principle chosen is one which seeks to make $\beta$, the longitudinal propagation constant, stationary and is given by

$$\beta^2 = \frac{\iint\limits_{\Omega}\left\{k^2\left|E\right|^2 - \left|\frac{\partial E}{\partial x}\right|^2 - \left|\frac{\partial E}{\partial x}\right|^2\right\}dxdy}{\iint\limits_{\Omega}\left|E\right|^2 dxdy} \tag{3.21}$$

where $\Omega$ is taken to mean all space in the transverse plane of the waveguide. This results in the most accurate prediction of $\beta$ since first order errors in the trial functions for $E$ give rise to second order errors in $\beta$. From (3.21) the necessary variational boundary condition is derived and given by

$$\int\limits_{-\infty}^{\infty} E\left[\frac{\partial E^*}{\partial y}\right]_{y=-0}^{y=+0} dx = 0 \tag{3.22}$$

Using (3.22) to match the solution in regions $\Omega_1,\Omega_2$ and applying Parseval's theorem results in

$$\int\limits_{-W}^{W} E_-^*\left[\frac{\partial E}{\partial y}\right]_- dx = \frac{1}{2\pi}\int\limits_{-\infty}^{+\infty} \phi_+^*\left[\frac{\partial \phi}{\partial y}\right]_+ ds \tag{3.23}$$

where the subscripts $+$ and $-$ are used to denote the solution just below and just above the boundary respectively. A normalised gradient function is introduced such that, just below the rib

$$\Gamma(s) = \frac{1}{\phi} \frac{\partial \phi}{\partial y}\bigg|_{y=+0} \tag{3.24}$$

Using equation (3.11) the LHS of (3.23) may now be written as

$$\int_{-W}^{W} E_-^* \left[\frac{\partial E}{\partial y}\right]_- dx = W\gamma_1 \cot(\gamma_1 H) \tag{3.25}$$

and, through (3.24), (3.17) and (3.18) the RHS of (3.23) may be written as

$$\frac{1}{2\pi} \int_{-\infty}^{+\infty} \phi_+^* \left[\frac{\partial \phi}{\partial y}\right]_+ ds = \frac{2}{\pi} s_1^2 \int_{-\infty}^{\infty} \Gamma \frac{\cos^2(sW)}{(s_1^2 - s^2)} ds \tag{3.26}$$

Finally (3.23), (3.25) and (3.26) give the final transcendental equation for $\beta$

$$\gamma_1 \cot(\gamma_1 H) = \frac{2}{\pi} \frac{s_1^2}{W} \int_{-\infty}^{\infty} \Gamma \frac{\cos^2(sW)}{(s_1^2 - s^2)} ds \tag{3.27}$$

and is the principal result of the standard SI method.

Equation (3.27) may then be solved relatively simply by bracketing the root and employing a bisection routine. For lossless waveguides, i.e. the situation where all indices are real, the solution of the transcendental equation using the bisection method on a standard personal computer takes less than a second with negligible memory usage. Because $\beta$ is not known in advance, $\beta$ in (3.4) is initially replaced

with $k_0 n_3$. The value of β in (3.4) is then continually updated to yield the most accurate results. For systems with loss or gain, β will be complex and it will be necessary to employ a suitable complex root finding algorithm. The method as presented yields highly accurate results for β and accurate prediction of field profiles, [3.4]. Table 3-1 and figure 3-3 illustrate the accuracy of the SI method by presenting a comparison with a semi-vectorial finite difference (SV-FD) scheme of the normalised propagation constants for the fundamental quasi-TE and quasi-TM modes of a simple rib waveguide; $w = 3\mu m$, $h + d = 1\mu m$, λ=1.15μm and refractive indices of $n_1 = 1.0$ (air), $n_2 = 3.44$ (GaAs) and $n_3 = 3.40$ $(Ga_{0.9}Al_{0.1}As)$. The normalised propagation constant, b, is defined as, [3.13],

$$b^2 = \frac{\beta^2 - n_3^2}{n_2^2 - n_3^2} \tag{3.28}$$

and is sensitive to small changes in β and so proves useful when discussing accuracy. Once β has been successfully found the field profiles may be obtained in a straight forward manner. In the rib β is substituted back into (3.11). Below the rib β is substituted back into (3.16) and a Fast Fourier Transform routine being used to transform the field back into real space. Figure 3-4 illustrate the field profile for the fundamental quasi-TE mode supported by the rib waveguide of previously described with $h = 0.5\mu m$.

As previously stated, retaining only the first term in (3.5) is sufficient for an accurate analysis. Figure 3-5 further demonstrates this point through a comparison of results computed via; single term SI, multiple-term SI and a SV-FD scheme. It is seen that

56

increasing the number of terms to two, results in almost complete agreement with the

SV-FD scheme with a negligible impact on computational requirements.

| H(μm) | Spectral Index Method | | Semi-vectorial FD | |
|---|---|---|---|---|
| | quasi-TE | quasi-TM | quasi-TE | quasi-TM |
| 0.1 | 0.3842 | 0.3410 | 0.3872 | 0.3442 |
| 0.2 | 0.3617 | 0.3199 | 0.3665 | 0.3246 |
| 0.3 | 0.3459 | 0.3055 | 0.3502 | 0.3096 |
| 0.4 | 0.3337 | 0.2946 | 0.3368 | 0.2975 |
| 0.5 | 0.3239 | 0.2860 | 0.3257 | 0.2877 |
| 0.6 | 0.3161 | 0.2792 | 0.3167 | 0.2798 |
| 0.7 | 0.3099 | 0.2740 | 0.3095 | 0.2738 |
| 0.8 | 0.3052 | 0.2700 | 0.3042 | 0.2693 |
| 0.9 | 0.3018 | 0.2671 | 0.3003 | 0.2661 |
| 1.0 | 0.2994 | 0.2651 | 0.2977 | 0.2639 |

**Table 3-1** Comparison of the normalised propagation constants, b, of the fundamental quasi-TE and quasi-TM modes,calculated by the SI method and a semi-vectorial finite difference scheme for the rib waveguide of Figure 3-2(a) where W=3.0μm, D+H=1.0μm, $n_1$=1.0, $n_2$=3.44, $n_3$=3.40 and λ=1.15μm.

## 3.7  Conclusions

The SI method is an extremely efficient analysis technique that has been applied to

rib waveguides of rectangular cross section. The method accurately predicts

longitudinal propagation constants and field profiles for this class of waveguide.

This, together with the relative simplicity of the method means it is ideally suited as

a CAD tool for the analysis of the polarised modes of optical waveguides and to its

extension to a wider range of optical components and circuits, which is the subject of

the remainder of this thesis.

(a)
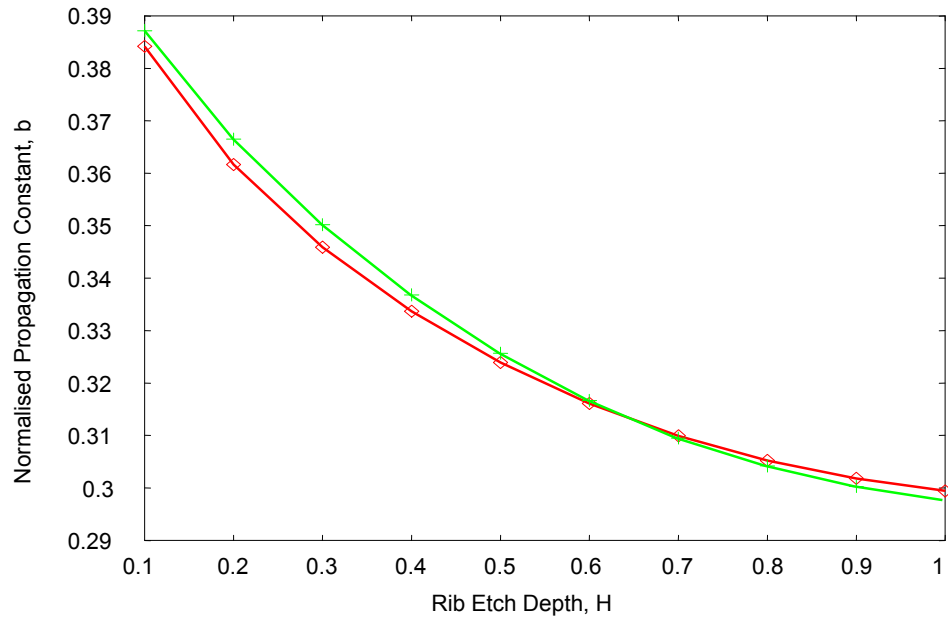


(b)
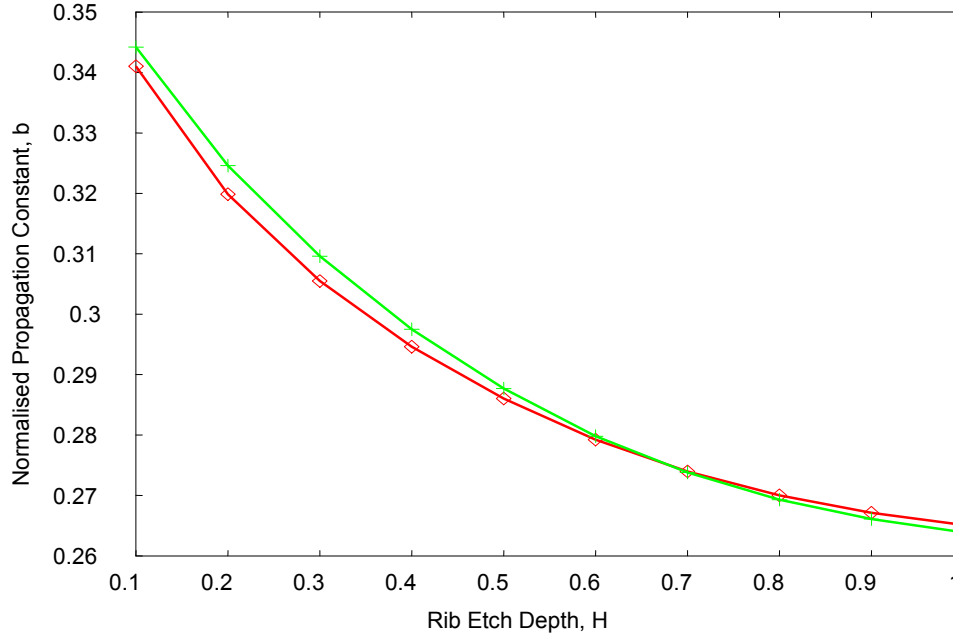


**Figure 3-3** Graphical representation of the data in table 3-1 for the (a) fundamental quasi-TE mode and (b) the fundamental quasi-TM mode.
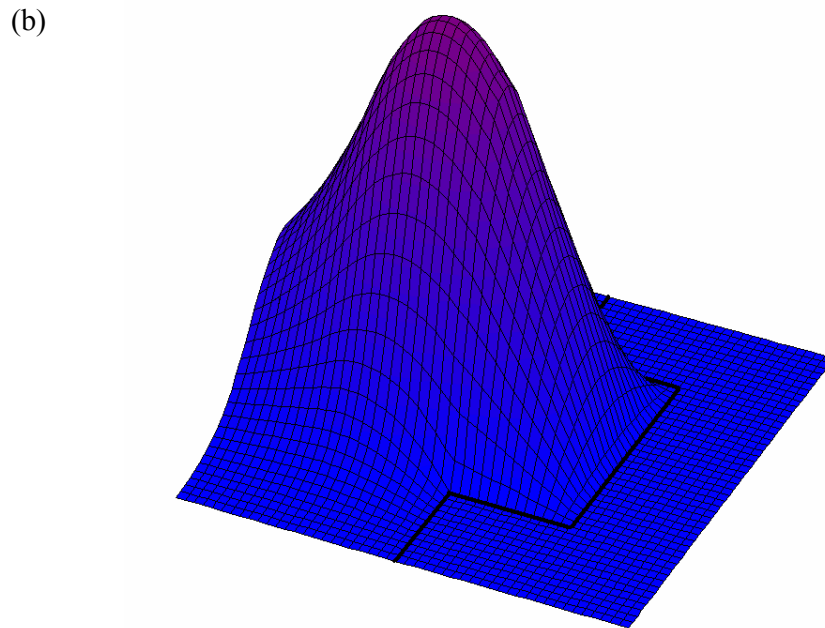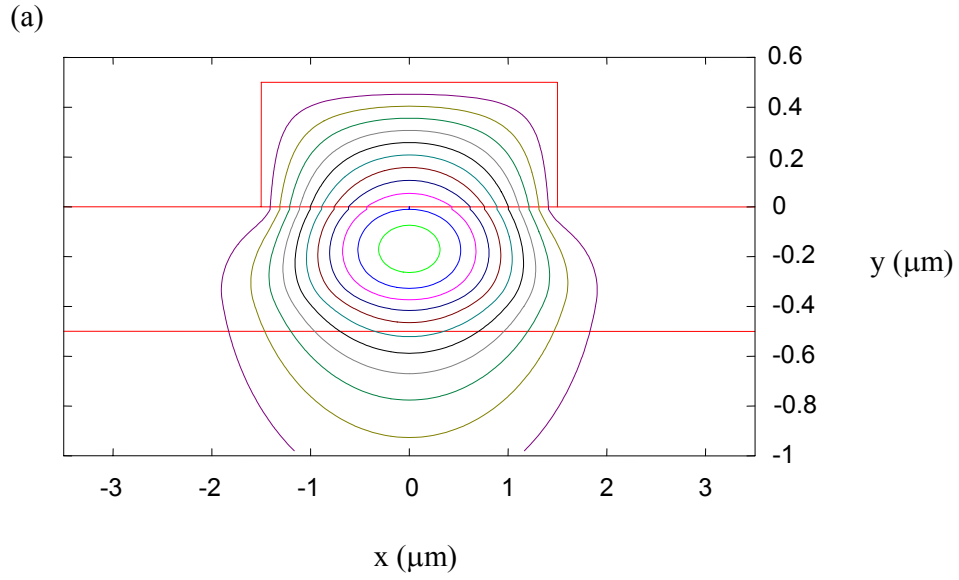
(a)



(b)



**Figure 3-4** Optical field distribution of the fundamental quasi-TE mode of the rib waveguide where; W=3.0μm, H=0.5μm, $n_1$=1.0, $n_2$=3.44, $n_3$=3.40 and λ=1.15μm; (a) Contour plot, and (b) 3D Surface plot where the bold lines indicate the physical boundary of the rib structure.
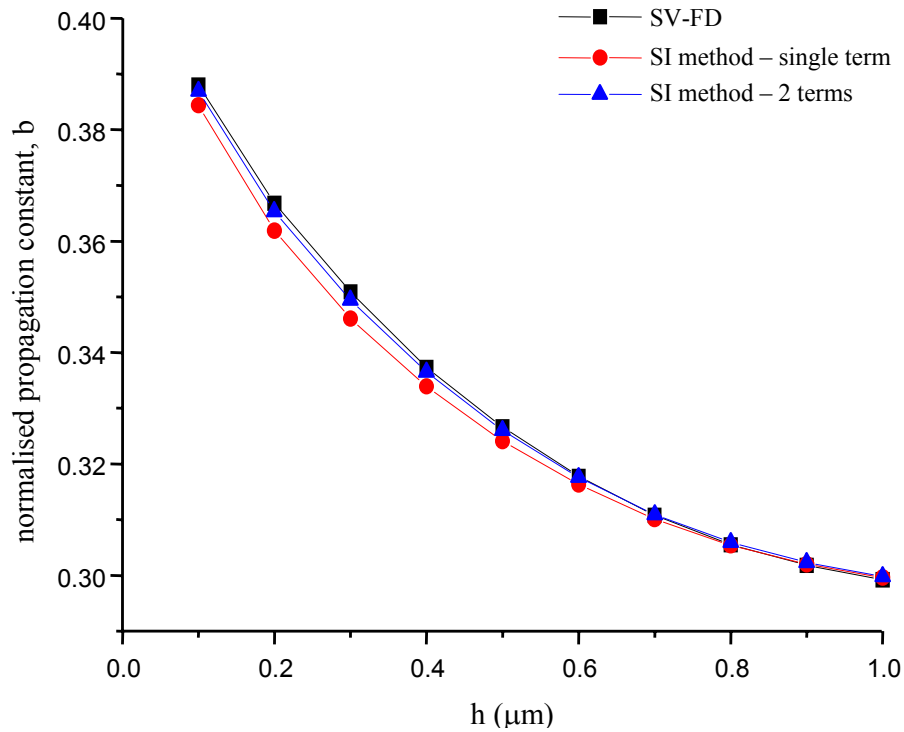
**Figure 3-5** Comparison of normalised propagation constant, b, of the fundamental quasi-TE mode computed by single and multi-term SI schemes versus a SV-FD scheme for the rib waveguide of table 3-1.

## 3.8 The SI Method: Admittance Formulation

The SI method may alternatively be formulated in terms of admittances. In this formulation the method treats the rib waveguide as a short circuited transmission line transmission line, figure 3-6. This approach is utilised in later chapters where it is applied to the analysis of optical spot size transformers, (§4.5), and rib waveguides of non-rectangular cross section, (§5.2).
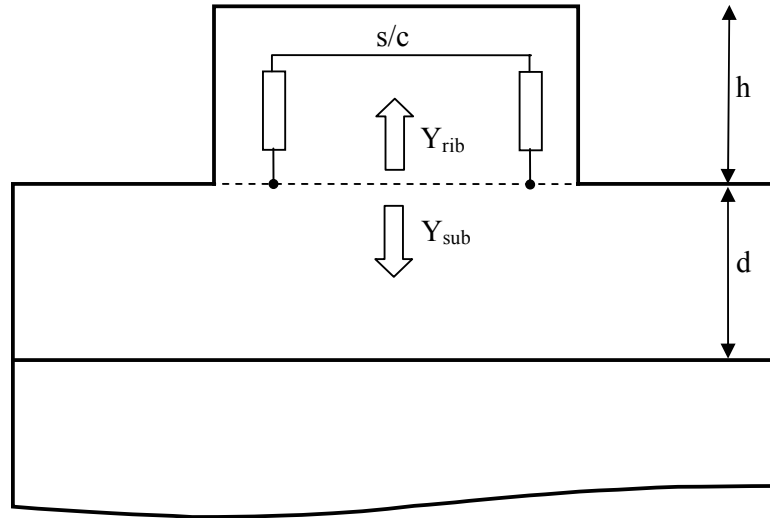
**Figure 3-6** Schematic of a rib waveguide and the representation of the rib by a short circuited transmission line.

At the base of the rib the electric field and magnetic field maybe be expressed as

$$E(x,0) = \sum_{n=1}^{N} \overline{V_0} \cos\left(\frac{(2n+1)\pi x}{2W}\right) \qquad (3.29)$$

and

$$-j\mu H(x,0) = \sum_{n=1}^{N} \overline{I_0} \cos\left(\frac{(2n+1)\pi x}{2W}\right) \qquad (3.30)$$

where use has been made of

$$\frac{\partial E}{\partial y} = -j\mu H \qquad (3.31)$$

and where $N$ is the number of terms used in the field expansion and $V$ and $I$ are unknown voltage and current like coefficients to be determined. On the top surface

of the effective rib ($y$ = -H) the field and its derivative is required to be zero (equivalent to a short circuit) and the unknown coefficients may be linked conveniently through the well known ABCD matrix notation, [3.14], such that

$$\begin{pmatrix} E_{top} \\ H_{top} \end{pmatrix} = \begin{pmatrix} \overline{\overline{A}} & \overline{\overline{B}} \\ \overline{\overline{C}} & \overline{\overline{D}} \end{pmatrix} \begin{pmatrix} \overline{V_0} \\ \overline{I_0} \end{pmatrix} = \begin{pmatrix} 0 \\ 0 \end{pmatrix} \tag{3.32}$$

where

$$A_{nm} = D_{n,n} = \cos(\gamma_{nm} H) $$

$$B_{nm} = \frac{\sin(\gamma_{nm} H)}{\gamma_{nm}} \tag{3.33}$$

$$C_{nm} = -\gamma_{nm} \sin(\gamma_{nm} H) $$

thus from (3.32)

$$\overline{\overline{A}} V_0 + \overline{\overline{B}} I_0 = 0 \tag{3.34}$$

Below the rib, define

$$\overline{I} = \overline{\overline{Y}} \overline{V} \tag{3.35}$$

where

$$Y_{i,j} = \int_0^\infty \varphi_i(s) \varphi_j(s) \Gamma(s) ds, \tag{3.36}$$

$$\varphi_i(s) = \int_0^\infty \sqrt{\frac{2}{\pi}} \cos(sx) \varphi_{i,0}(x) ds \tag{3.37}$$

and $\Gamma(s)$ is the standard plane wave response function. Combining (3.34) and (3.35) gives

$$\left( \overline{\overline{Y}} + \overline{\overline{B}}^{-1} \overline{\overline{A}} \right) \overline{V_0} = 0$$

$$\Rightarrow \left( \overline{\overline{BY}} + \overline{\overline{A}} \right) \overline{V_0} = 0$$

(3.38)

which is solved by requiring

$$\left| \overline{\overline{BY}} + \overline{\overline{A}} \right| = 0$$

(3.39)

and is equivalent to the multiple term SI transcendental equation for even modes of a rib waveguide.

## 3.9 References

[3.1]  P. C. Kendall, P. W. A. McIlroy, and M. S. Stern, "Spectral index method for rib waveguide analysis", Electronics Letters, vol. 25(2), pp. 107-108, 1989.

[3.2]  P. W. A. Mc Ilroy, M. S. Stern, and P. C. Kendall, "Spectral Index method for polarized modes in semiconductor rib waveguides", IEEE Journal of Lightwave Technology, vol. 8(1), pp. 113-117, 1990.

[3.3]  M. S. Stern, P. C. Kendall, and P. W. McIlroy, "Analysis of the spectral index method for vector modes of rib waveguides", IEE Proc. Optoelectronics, vol.137, pp. 21-26, 1990.

[3.4]  S. V. Burke, "Electromagnetic wave propagation in rib waveguide components for integrated optics", PhD Thesis, University of Sheffield, 1991.

[3.5]  P. N. Robson, and P. C. Kendall (Eds.), "Rib waveguide theory by the spectral index method", Wiley, New York, 1990.

[3.6]  P. C. Kendall, M. S. Stern, and S. V. Burke, "Planar waveguide analysis by the spectral index method. I: Rib and uniformly buried waveguides", Optical and Quantum Electronics, vol. 25, pp.771-787, 1993.

[3.7]  S. V. Burke, "Planar waveguide analysis by the spectral index method. II: Multiple layers, optical gain and loss", Optical and Quantum Electronics, vol. 26, pp.63-77, 1993.

[3.8]  S. V. Burke, "The spectral index method for semiconductor rib and ridge waveguides", Chapter 2, PIER 10, partI, EMW publishing, 1995.

[3.9]  J. R. Pujol Pola, W. Biehlig, and F. Lederer, "A generalization of the spectral index method toward multiple rib waveguides", IEEE Journal of Lightwave Technology, vol. 14(3), pp. 454-461, 1996.

[3.10]  W. C. Ng, M. S. Stern, "Analysis of multiple-rib waveguide structures by the discrete-spectral-index method", IEE Proc. Optoelectronics, vol. 145(6), pp.365-371, 1998.

[3.11]  P. Sewell, T. M. Benson, P. C. Kendall, "Rib waveguide spot-size transformers: Modal properties", IEEE Journal of Lightwave Technology, vol. 17(5), pp.848-856, 1999.

[3.12]  A. Vukovic, P. Sewell, S. Sujecki, T. M. Benson, "Singularity corrected spectral index method", IEE Proc. Optoelectronics, vol. 145(1), pp 59-64, 1998.

[3.13]  T. Tamir, "Integrated Optics", Springer-Verlag, 1979.

[3.14]  R. E. Collin, "Field theory of guided waves", IEEE Press, 1991.

# Chapter 4  SI Method Applied to the Design of a Novel SiGe Based Mode Spot Size Converter

## 4.1  Introduction

Recent years have seen the rapid evolution of silicon based optoelectronics. The absorption properties of $Si_{1-x}Ge_x$ alloys make them excellent materials for the realisation of photodetectors operating at the near-infrared wavelengths of 1.3 and 1.55µm which are important for fibre optic communication systems. An important design consideration for such systems is the efficient coupling of optical fibres to optoelectronic integrated circuits. This chapter details the design of a novel $Si_{1-x}Ge_x$ rib waveguide spot size converter (SSC), or mode transformer, that performs two essential roles; the transformation of the large spot fibre to a small spot waveguide mode and subsequently the transferral of the mode from a passive silicon waveguiding region to an active $Si_{1-x}Ge_x$ region where optical absorption may occur. This transformation is accomplished through use of a tapered waveguide structure.

In the following chapter a brief overview of silicon optoelectronics is given, which sets the requirements for the following work. Material properties that require careful consideration when working within a $Si_{1-x}Ge_x$ material system are then discussed. The concept of a SSC is introduced. Following this an analysis technique based on the SI method is used to investigate the local modal behaviour of the proposed

structure which was ultimately fabricated[1]. The SCC was then experimentally evaluated and comparisons drawn between those results and those predicted by the model.

## 4.2   Silicon Optoelectronics

Silicon (Si), being an indirect bandgap material has very poor abilities in the emission / absorption of light at room temperature (300K). Because of this Si had traditionally been overlooked for use in optical communications systems at the important wavelengths of 1.3 and 1.55μm as the material was unable to offer practical active devices, although silicon based photodetectors dominate at wavelengths of $< 1\mu m$. Silicon is transparent over the important optical communications range 1.3 and 1.55μm (its energy band gap being $\approx 1.2eV$) and low loss waveguiding over this region has been demonstrated; [4.1]-[4.4] for silicon-on-insulator waveguides, [4.5]-[4.6], and [4.7]-[4.9] for porous silicon based waveguides. The addition of Germanium (Ge), to form a SiGe alloy, has been used to enhance the refractive index of the material to produce waveguides that can be directly fabricated onto Si substrates, [4.10]-[4.14]. Furthermore the addition of Ge enhances the absorption coefficient at these wavelengths and recent years have seen the realisation of integrated SiGe based photodetectors for use over this range, [4.14]-[4.16]. Further advances have shown SiGe based light emitting diodes (LEDs)

---

[1] This work was carried out as part of Technology Group (7) of the UKMoD Corporate Research Programme.

that operate at room temperature, [4.17]. More recently, the advantages offered by silicon as a photonic medium for the large scale integration of optical components, [4.18], have led to renewed interest in silicon based microphotonic circuits, [4.19].

## 4.3   Properties of Si and Si-Ge alloys

The following outlines some of the material properties of Si and SiGe that require careful consideration throughout the design process. Several variables regarding geometry may present themselves during an iterative design process. The success of any design is therefore dependant upon the designer's awareness of material issues in order to optimise the design whilst remaining within those constraints imposed by the materials properties.

### 4.3.1   Strain

Silicon and germanium have different lattice constants (the regular spacing between the materials atoms), giving rise to a lattice mismatch of ~4% between the bulk Si and a Si-Ge alloy figure 4-1 (a). When SiGe is grown on a Si substrate the lattice symmetry of the Si-Ge becomes coherent with that of the Si substrate, figure 4-1 (b). This results in the SiGe layer becoming strained, [4.20]-[4.22]. This strain increases with epitaxial thickness until a critical layer thickness is reached at which point dislocations may form to relieve the strain in the layer, figure 4-2. These dislocations are both a loss mechanism and a cause of device failure and so need to be avoided. Dislocation free pseudomorphic growth of Si-Ge epilayers maybe achieved,

however, by ensuring that the SiGe layer thickness is kept below the critical thickness.

(a)                                      (b)



● Silicon  ● Germanium

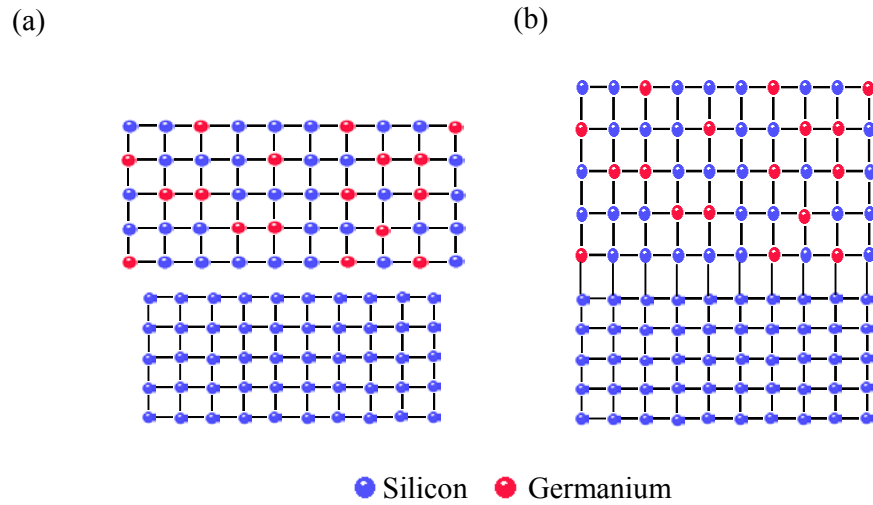**Figure 4-1** Illustration of the crystal lattice structures of (a) Si and $Si_{1-x}Ge_x$, (b) strained $Si_{1-x}Ge_x$ layer grown on Si.
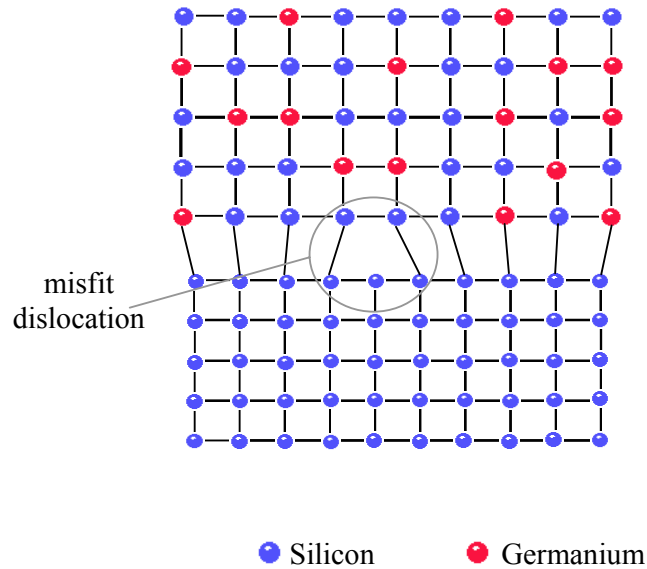


misfit
dislocation

● Silicon      ● Germanium

**Figure 4-2** Illustration of a misfit dislocation.

For non-metastable material a $Si_{1-x}Ge_x$ layer will be coherently strained if its thickness is less than a critical value, $t_c$, given by the empirical formula [4.23]

$$t_c = t_0 x^{-3.6} \tag{4.1}$$

where $t_0 = 8.2$ Å and $x$ is the germanium fraction. The formula (4.1) is illustrated in figure 4-3.
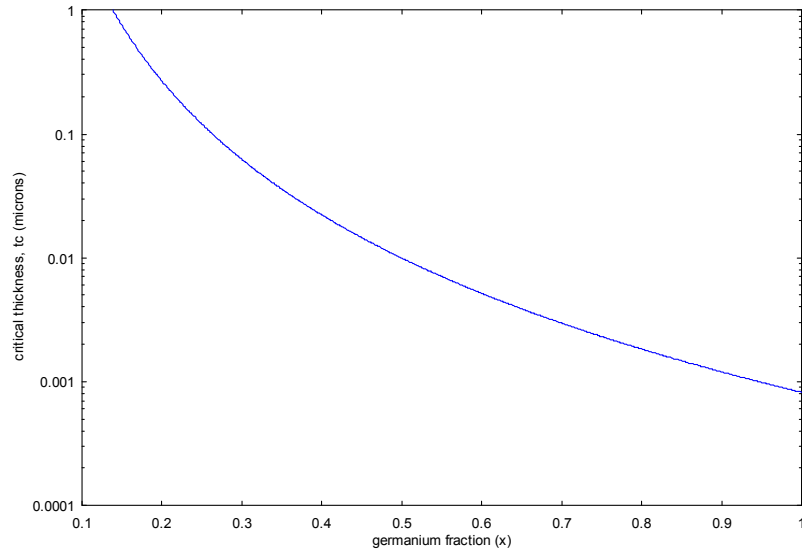


**Figure 4-3** Critical thickness as a function of germanium content.

## 4.3.2 Refractive index of Si

The room temperature (~300K) refractive index of Si at a wavelength of 1.55μm is 3.477, [4.24]. This refractive index and hence the materials waveguiding properties can be altered by changing the concentration of charge carriers within the material.

The mechanism that shall be considered here is the effect of the density of charge carriers within the material. This has been studied previously, [4.25], and figure 4-4 illustrates the change in refractive index with free carrier concentration. It should be noted though that losses increase with carrier concentration due to free carrier absorption.



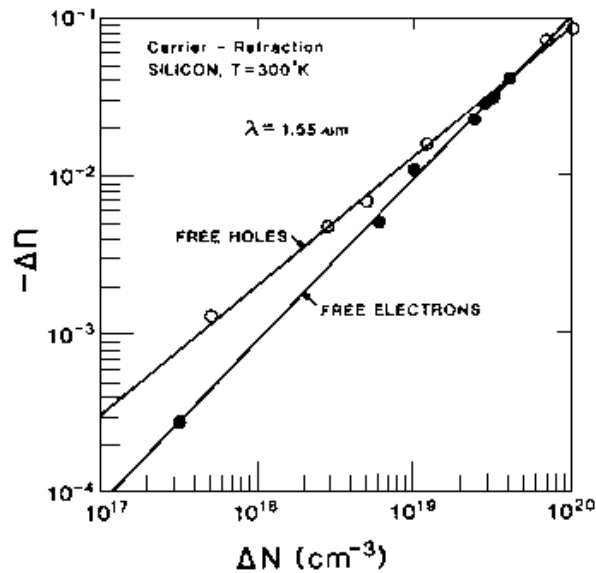**Figure 4-4** Carrier refraction at $\lambda$=1.55μm as a function of free carrier concentration, (reproduced from [4.25]).

### 4.3.3  Refractive index of $Si_{1-x}Ge_x$

The room temperature refractive indices of bulk silicon and germanium at a wavelength of 1.55μm are 3.477 and 4.275 respectively, [4.24]. Thus, as previously mentioned, Ge can be used to enhance the refractive index of Si. A relationship for

the refractive index of $Si_{1-x}Ge_x$ as a function of Ge content, $x$, has been proposed [4.26] and is given by

$$n\left(Si_{1-x}Ge_x\right) = n\left(Si\right) + \frac{\left[n\left(Ge\right) - n\left(Si\right)\right]\left[Eg\left(Si\right) - Eg\left(x\right)\right]}{\left[Eg\left(Si\right) - Eg\left(Ge\right)\right]} \qquad (4.2)$$

where, $E_g(Si)$ and $E_g(Ge)$ are the energy gaps of the unstrained bulk materials. $E_g(x)$ is the indirect gap of the strained $Si_{1-x}Ge_x$, given by [4.27]

$$Eg\left(x\right) = 1.1 - 1.02x + 0.52x^2 \qquad (@\ T=295k) \qquad (4.3)$$

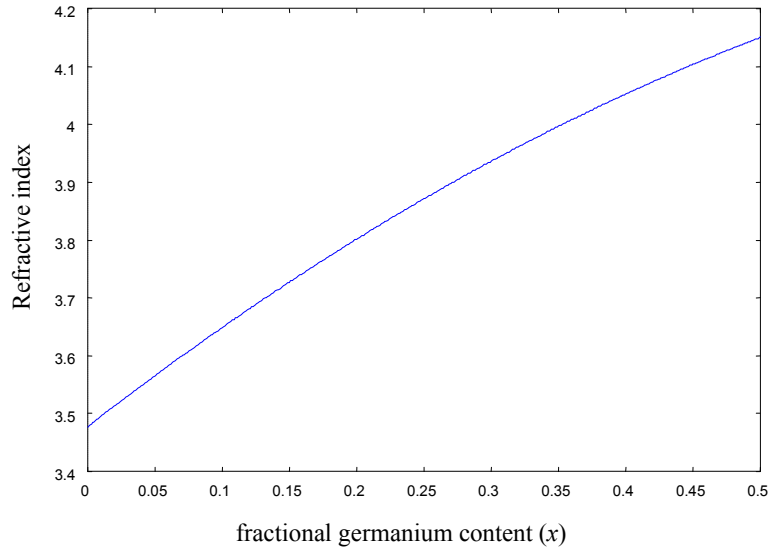Figure 4-5 presents the change in refractive index with Ge content predicted by equations (4.2) and (4.3).



**Figure 4-5** Change in refractive index with germanium content (@ T=295k, $\lambda$=1.55μm).

72

## 4.4   Mode Spot Size Converters

Active optical devices are, in general, typified by having tightly bound elliptical spot sizes of large aspect ratio that make the task of coupling to the circular and larger modes supported by single mode optical fibres inefficient and highly sensitive to alignment tolerances. The situation is illustrated in figure 4-6, and has, over recent years, received considerable attention. Mode spot-size converters (SSCs) that allow efficient coupling of fibres to active devices have been demonstrated in III-V and polymer materials, [4.28]-[4.30]. It is important to note that the specific design of these SSCs is generally dictated by the material system of the device technology and the limitations it imposes. However, typically the design comprises three common regions; a tightly confined active device region, a tapered region and a more loosely confined passive input or output region. The tapered region provides a mechanism for the adiabatic transformation of the large spot size offered by a single mode fibre to the spot size at the active device. Such tapered devices may make use of lateral or vertical taper designs or a combination of both, [4.29]. The operation of taper based SSCs are similar in that, at the input facet the upper waveguide is cut-off, whilst the underlying waveguide supports a fundamental mode similar in profile to that of a single mode fibre. As the upper rib progressively widens in the direction of propagation it becomes the dominant guiding mechanism and at some point the light will shift totally from the lower to the upper rib undergoing a spot-size transformation. Figure 4-7 illustrates the optical field profiles at the input facet and the transformed field at the output facet.

w

Optical fibre Core ∅,
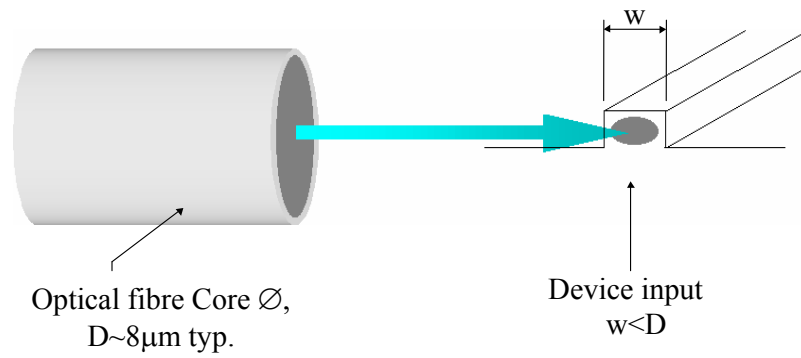D~8μm typ.

Device input
w<D

**Figure 4-6** Optical mismatch between fibre and detector input.
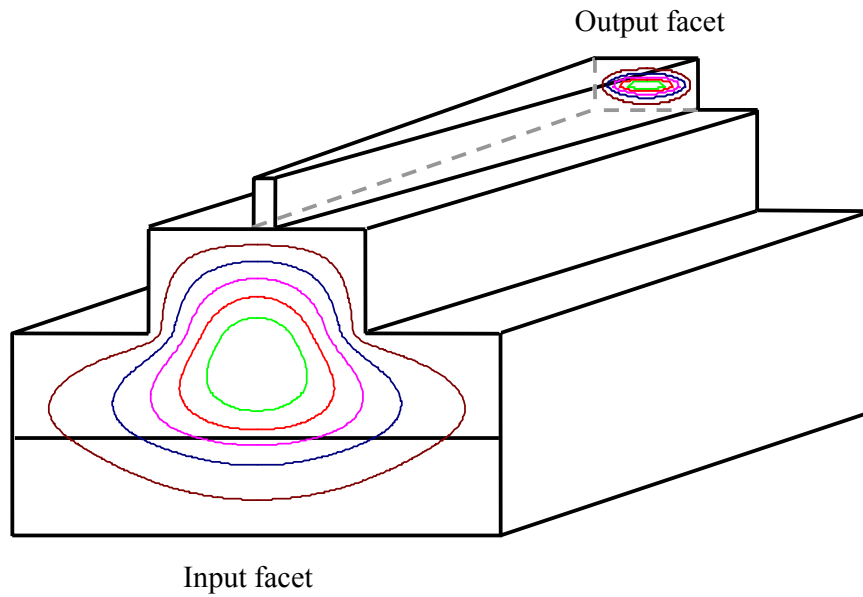


Output facet

Input facet

**Figure 4-7** Illustration of the optical fields at input and output stages of a taper based rib waveguide based SSC.

The approach adopted in this work was to use a laterally tapered rib on rib structure, figure 4-8. The active Si-Ge based device epitaxy is grown on top of a wider silicon mesa to produce the rib on rib structure. The wider mesa forms a large spot size rib waveguide in its own right, whose spot size can be optimised to closely match that of the fibre to provide the means for coupling light from the fibre source. The upper rib is tapered and as the width of this taper is increased the optical mode is driven from the lower guiding region into the upper active region as previously described.
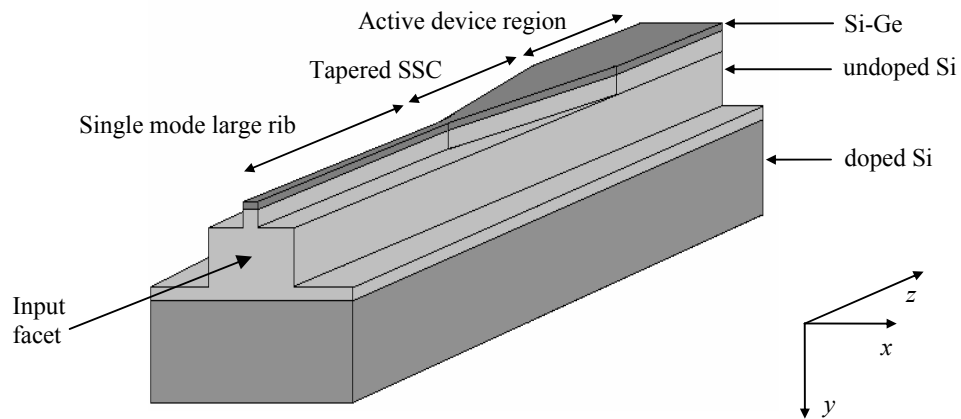
**Figure 4-8** Rib on rib/taper mode spot size converter.

The epitaxial structure being considered, figure 4-9, in this work consists of a lightly doped, 6μm thick, Si epitaxial layer which also includes a SiGe multiple quantum well (MQW) absorption region, grown on a heavily doped n$^+$ substrate. The presence of free electrons in the substrate depresses the real part of the refractive index $\left(\Delta n \sim 10^{-3}\right)$ and in doing so creates vertical confinement in the large spot waveguide

discussed above. However these free carriers also introduce an additional loss mechanism, [4.25], and so the minimisation of the field in this layer is also desirable.

The composition of the $Si/Si_{1-x}Ge_x$ MQW absorption region was modelled by an equivalent uniform layer approximately 0.7µm deep with an effective refractive index of n=3.6 at a wavelength of 1.55µm. The refractive index of the $Si_{1-x}Ge_x$ alloy was determined by the interpolation formula (4.2) with an average refractive index being taken across this region during the modelling process. The bulk Si materials were taken to have a refractive indices of n=3.477 and n=3.474, for the intrinsic and $n^+$ materials respectively, at this wavelength.



**Figure 4-9** Epitaxial structure on which the device was to be fabricated.

## 4.5  SI Methodology

An analysis technique based on the SI method described in the previous chapter was used to investigate the modal properties of the waveguiding structure.  The technique allowed for the efficient analysis of any cross-sectional refractive index profile of the rib-on-rib SSC along the length of the structure. This approach provides significant insight into the performance of the SSC whilst maintaining a high degree of computational efficiency and is well suited to an iterative design process such as that adopted here. The method is fully covered in [4.31], but an overview is given here for completeness, and is presented for the TE case only.

### 4.5.1   Derivation of the transcendental equation

With reference to the notation introduced in the previous chapter, (§3.8), the method proceeds in the same manner as the standard SI method, whereby the physical structure is replaced with another whose boundaries have been displaced and the field set to zero at these boundaries, as shown in figure 4-10. The field in each region; the upper rib (I), the underlying large rib (II) and the substrate (III), can then be represented as a superposition of local solutions of the wave equation. In region I, the principal field component, $E_x$, is well approximated by:

$$E(x, y) = \cos(s_1 x) \frac{\sin(\gamma_1 (y + h'))}{\sin(\gamma_1 h')} \tag{4.4}$$

where:

$$s_1 = \frac{\pi}{2W_1'} \quad , \quad \gamma_1^2 = n_1^2 k_o^2 - s_1^2 - \beta^2 \tag{4.5}$$

In region II the field and its derivative can be expressed as:

$$E(x,0) = \sum_{n=1}^{N} V_{1,n} \cos(t_n x) \quad , \quad \frac{\partial E_1}{\partial y}(x,0) = \sum_{n=1}^{N} I_{1,n} \cos(t_n x) \tag{4.6}$$

at the top of region II, $y=0$, and similarly along the base of region II, $y=-h'_2$:

$$E(x,h_2') = \sum_{n=1}^{N} V_{2,n} \cos(t_n x) \quad , \quad \frac{\partial E_1}{\partial y}(x,h_2') = \sum_{n=1}^{N} I_{2,n} \cos(t_n x) \tag{4.7}$$

In region III the field and its gradient can be expressed as a superposition of plane waves:

$$E(x,y) = \int_0^\infty \partial s \, V(s) \cos(sx) e^{-\gamma(y-h)}$$

$$\frac{\partial E(x,y)}{\partial y} = \int_0^\infty \partial s \, I(s) \cos(sx) e^{-\gamma(y-h)} \tag{4.8}$$

The coefficients of (4.6) and (4.7) are then related by the well known ABCD notation such that:

$$\begin{pmatrix} V_2 \\ I_2 \end{pmatrix} = \begin{pmatrix} A & B \\ C & D \end{pmatrix} \begin{pmatrix} V_1 \\ I_1 \end{pmatrix} \quad , \quad t_n = \frac{n\pi}{2W_2'} \tag{4.9}$$

78

As $\underline{V}_2$ and $\underline{I}_2$ are also related by the response function of the substrate region conveniently expressed in the form:

$$\underline{I}_2 = \underline{Y}\underline{V}_2 \tag{4.10}$$

(4.9) and (4.10) then yield the relationship:

$$\left(\underline{C} - \underline{Y}\underline{A}\right)\underline{V}_1 = \left(\underline{Y}\underline{B} - \underline{D}\right)\underline{I}_1 \tag{4.11}$$

Finally enforcing field continuity at $y=0$, (4.4) and (4.6) yield:

$$V_{1,n} = \frac{s_1 \cos\left(t_n W_1'\right)}{s_1^2 - t_n^2} \tag{4.12}$$

A variational expression is then used to match the field gradient at $y=0$ resulting in the final transcendental equation:

$$\gamma_1 \cot\left(\gamma_1 h_1\right) - \left(\frac{W_2'}{W_1'}\right)\underline{V}_1^H \underline{I}_1 = 0 \tag{4.13}$$

In practice the solution to (4.13) is obtained by evaluating $\underline{Y}$, $\underline{A}$, $\underline{B}$, $\underline{C}$ then $\underline{D}$ and then using (4.11) to obtain $\underline{I}_1$, which is in turn substituted into (4.13). The values of the propagation constant, $\beta$, that satisfy (4.13) are those of the modal solutions of the structure. In order to ensure numerical stability during the solution of (4.13) the

concept of accessible modes is utilised, a more detailed description of which is given
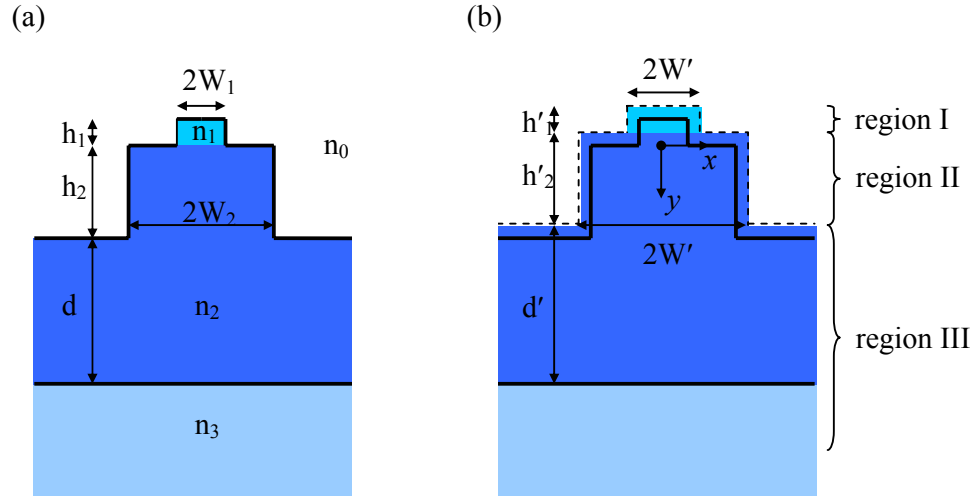
in [4.31].



**Figure 4-10** Diagram illustrating; (a) general structure, (b) use of effective boundaries, co-ordinate system, and separate regions considered during the SI analysis of a rib-on-rib waveguide

## 4.6   Spectral Index Method Results

Throughout the theoretical analysis it was assumed that the mode transformation occurs adiabatically, i.e. without power loss. The starting point for the design process was to identify the modal profiles at the start and finish of the tapered section, which are required to match the modes supported by the fibre and SiGe regions respectively. The composition of the $Si_{1-x}Ge_x$ absorption region was fixed, as was its position in the epitaxial structure. This still allowed for a great degree of freedom during the design process, with the ability to completely specify the upper and lower rib geometries. The efficiency of the theoretical model could therefore be fully exploited by evaluating several designs in as short a time as possible.

The modal profiles shown in Figure 4-11 show the theoretical fields, of the final design, for three widths; the large spot input profile, the point at which the mode begins to move up into the tapered region and the small spot output profile. Figure 4-12 depicts the variation in the propagation constant, $\beta$, with taper width, W. It is clearly seen that a rapid change in the guiding characteristics occurs around W = 1.2μm as the mode is transformed between the two guiding extremes. In order to facilitate adiabatic mode size transformation, it is required that this change takes place as gradually as possible around this critical width. Specifically, an initial design that achieves this is one in which $\dfrac{d\beta}{dz} = \left(\dfrac{d\beta}{dW}\right)\left(\dfrac{dW}{dz}\right)$ is kept constant along the taper, [4.31]. It is also noted that once below this critical point the width of the taper may be reduced more rapidly, facilitating a shorter device. A similar approach, considering fibre coupling to a semiconductor laser, has been demonstrated in ref [4.32]. Although the aim is adiabatic performance, initial designs focused upon linear tapers.
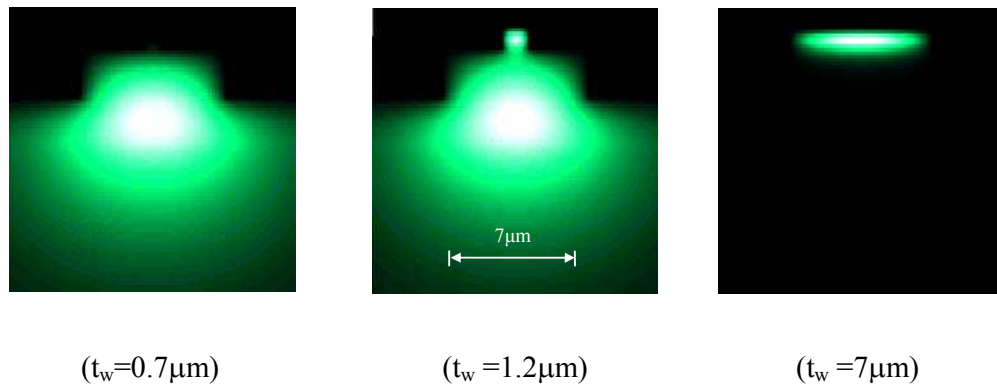


(t$_w$=0.7μm)                    (t$_w$ =1.2μm)                    (t$_w$ =7μm)

**Figure 4-11** Theoretical Field profiles (E$_x$) of the fundamental TE mode taper widths; t$_w$ = 0.7μm, t$_w$ = 1.2μm and  t$_w$ = 7 μm .
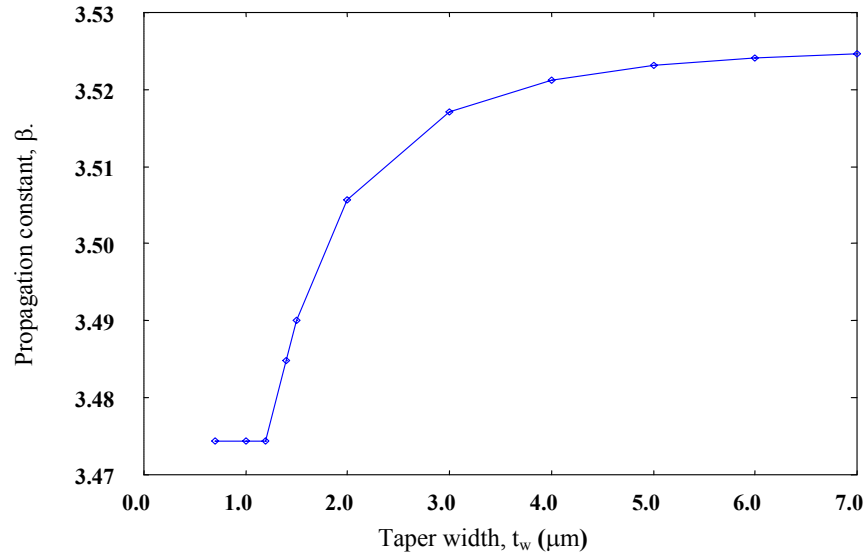
**Figure 4-12 Variation in propagation constant with taper width, $t_w$.**

## 4.7   Experimental evaluation

Investigations into the performance of the SSC were carried out through experimental evaluation of a 100μm long linear taper, figure 4-13. The position and intensity of the light emerging at the output facet of the SSC being determined experimentally using the arrangement shown in figure 4-14. A He-Ne laser of $\lambda = 1.52$μm was used as the incident light source which was focused to a spot size of ~4μm onto the large rib input face. The output from the SSC was then focused onto a near infrared (NIR) sensitive camera. The output from this camera was, in turn, processed by a personal computer and a digital storage oscilloscope (DSO) to enable image and data capture. The resulting modal profile and intensity distributions, in both the horizontal and vertical planes are shown in figure 4-15, and are seen to be in excellent agreement with theoretical predictions.

**Figure 4-13** Image captured with a CCD camera mounted on a microscope at x100 magnification showing the tapered rib on rib device.
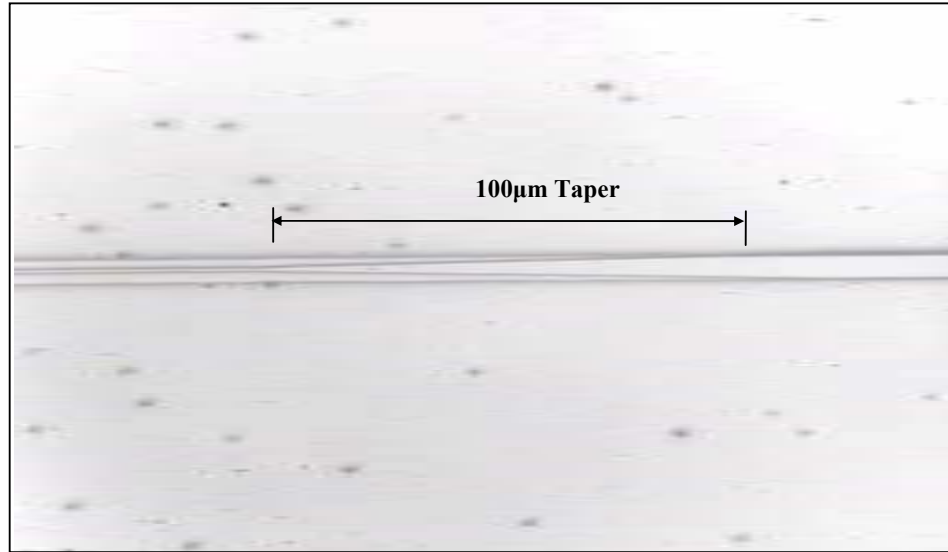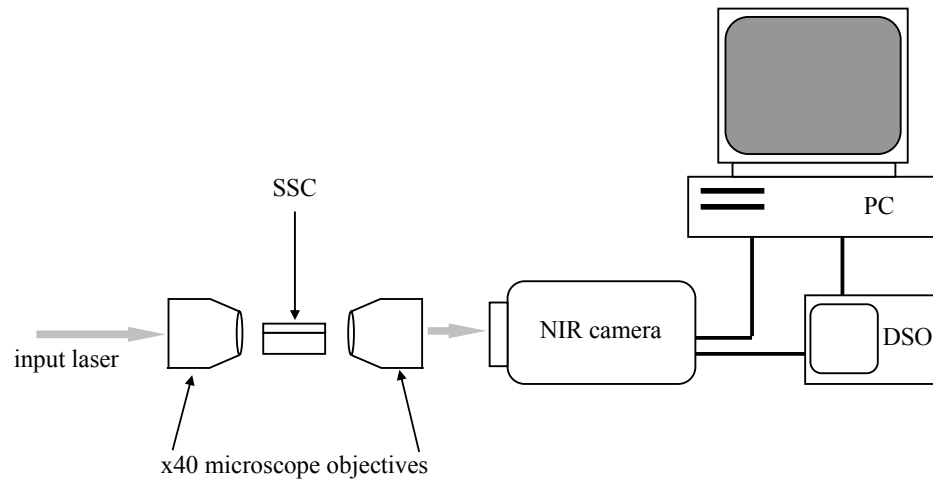


**Figure 4-14** Experimental set up used to obtain the modal profiles and intensity of the output of the SSC.
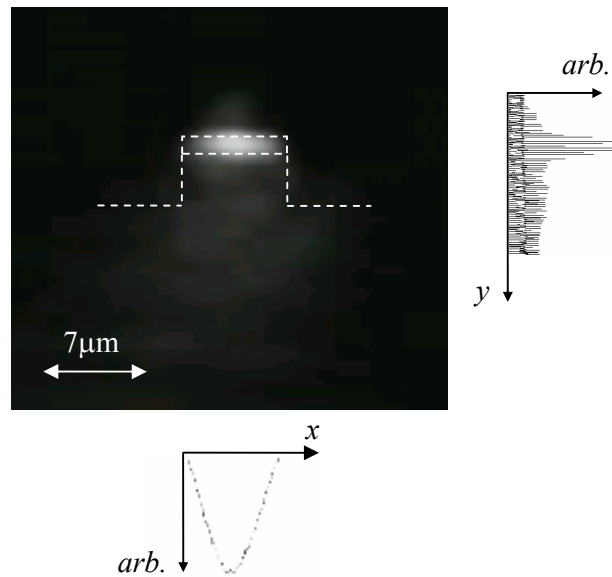
**Figure 4-15** Experimentally determined mode (taken through the points of maximum intensity) and intensity profiles. A schematic representation of the output face of the SSC is drawn over the mode profile to indicate the boundaries of the upper and lower rib regions.

## 4.8   SI method as an Optimisation Tool

Whilst maintaining an input spot size equivalent to that of a single mode fibre, it was also required of the SSC that the field in the lossy substrate be minimised. During the design process efforts were made to minimise the field in the substrate. But, as can be seen from the simulations of the final SSC there is significant penetration of the field into the substrate at the input of the device, figure 4-16, and was unavoidable within the constraints of the first device run. The material composition and dimensions of the epitaxy were already determined prior to the commencement of the work previously described.
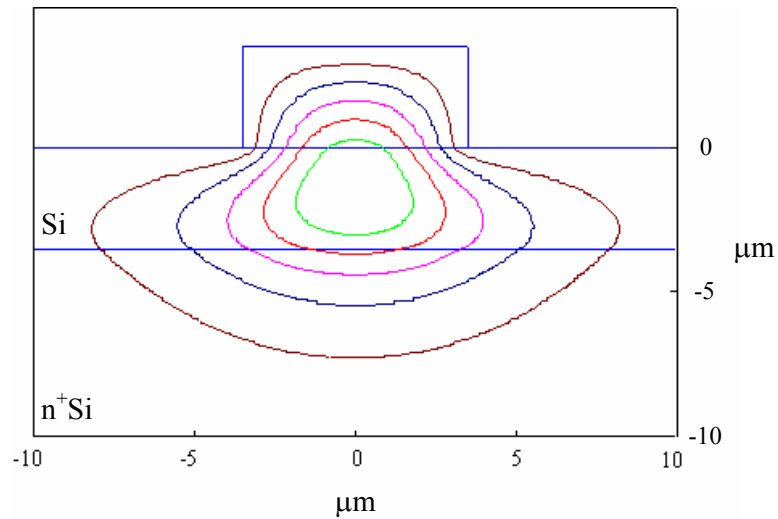
**Figure 4-16** Optical field at the input of the SSC.

In order to further reduce the field in the substrate it is necessary to increase the refractive index contrast between it and the guiding region. One approach is to use a low index substrate compatible with the fabrication process namely Bonded and Etched back Silicon on Insulator (BE-SOI). Another is to load the rib with an additional SiGe layer that effectively lifts the mode upwards into the rib region and away from the lossy substrate. Figure 4-17 and figure 4-18 illustrate the field profiles for the fundamental quasi-TE mode, implementing the two approaches. Both are seen to successfully reduce the field present in the substrate. This also further illustrates the suitability of the SI approach as its efficiency allowed for the rapid evaluation of proposed solutions to a problem targeted towards the optimisation of the design. At the time of the work the proposals where unable to be implemented due to the constraints of the project.
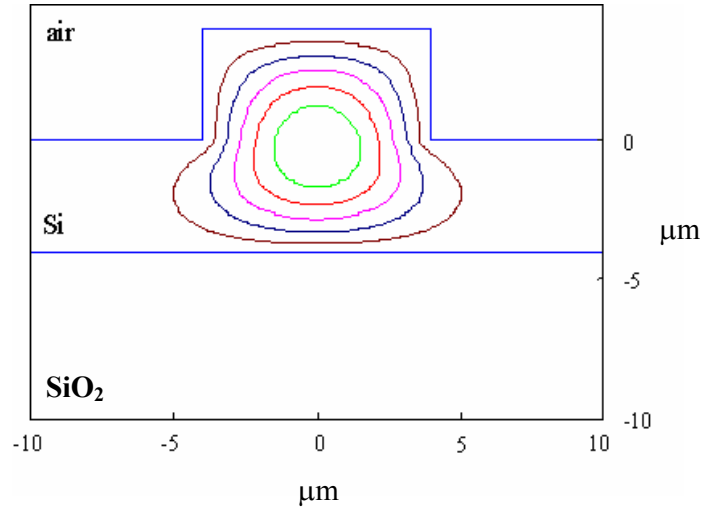
**Figure 4-17** Optical field at the input of the SSC fabricated on a BESOI wafer.

## 4.9   Conclusions

Theoretical and experimental results have been presented illustrating the operation, and hence the suitability, of a $Si_{1-x}Ge_x$ based mode spot size converter. To the best of the author's knowledge this was the first demonstration of the principle in this material technology that had been published, [4.33]. The process used to arrive at a suitable design within the material constraints was an iterative one, benefiting fully from the computational efficiency of the theoretical design method, namely the SI.

Excellent agreement is shown between the theoretical and experimental results further illustrating the suitability in adopting such a design methodology in establishing the basis of a good design.
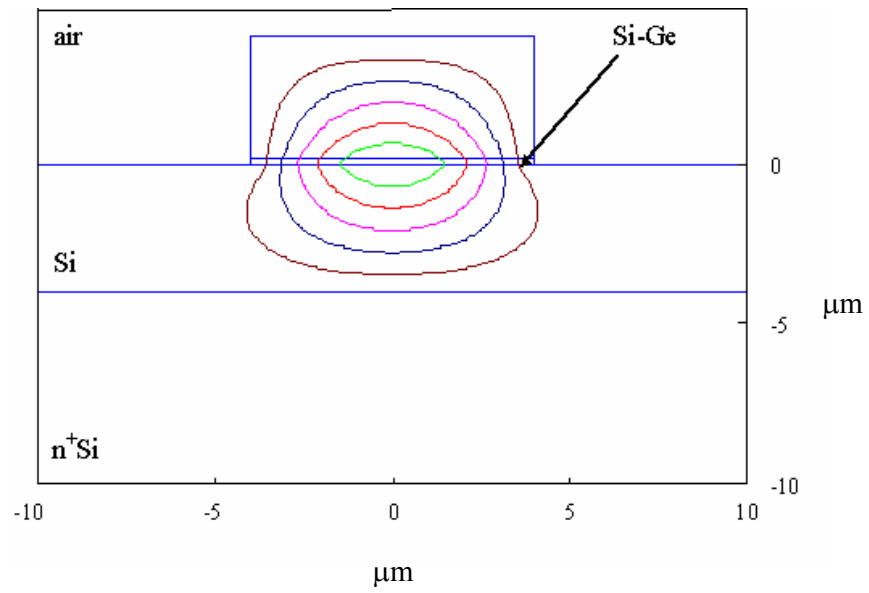
**Figure 4-18** Optical field at the input of the SSC for a SiGe strip loaded rib.

## 4.10 References

[4.1]   J. S. Richard, R. A.  Soref, K. Petermann, "Large Single-Mode Rib Waveguides in GeSi-Si and Si-on-SiO2," IEEE Journal of Quantum Electronics, vol. 27, pp. 1971-1974, 1991.

[4.2]   R. A.  Soref, J. Schmidtchen, and K. Petermann, "Low loss single mode optical waveguides with large cross section in silicon-on-insulator", Electronics Letters, vol. 27, pp. 1486-1488, 1991.

[4.3]   Y. L. Liu, E. K. Lui, G. Z. Li, S. L. Zhang, and J. S. Luo, "Novel silicon waveguide switch based on total internal reflection", Applied Physics Letters, vol. 64, pp. 2079-2080, 1994.

[4.4]   A. G. Rickman, G. T. Reed, and F. Navamar, "Silicon-on-insulator optical rib waveguide loss and mode characteristics", IEEE Journal of Lightwave Technology, vol. 12, pp. 1771-1776, 1994.

[4.5]   U. Fischer, T. Zinke, J. –R. Kropp, F. Arndt, and K. Petermann, "0.1 dB/cm waveguide losses in single mode SOI rib waveguides", IEEE Photonics Technology Letters, vol. 8, pp. 647-649, 1996.

[4.6]   A. Splett *et al*., "Integration of waveguides and photodetectors in SiGe for 1.3µm operation", IEEE Photonics Technology Letters, vol. 6, pp. 59-61, 1994.

[4.7]   N. Vorozov, L. Dolgyi, V. Yakovtseva, V. Bondarenko, M. Balucani, G. Lamedica, A. Ferrari, G. Vitrant, J. E. Broquin, T. M.  Benson, H. F. Arrand, and P.  Sewell, "Self-aligned oxidised porous silicon optical waveguides with reduced loss", Electronics Letters, Vol. 36(8), pp. 722-723, 2000 .

[4.8] H. F. Arrand, T. M. Benson, P. Sewell, A. Loni, R. J. Bozeat, R. Arens-Fischer, M. Kruger, M. Thonissen, and H Luth, "The application of porous silicon to optical waveguiding technology", IEEE Journal on Selected Topics in Quantum Electronics, vol. 4(6), pp. 975-982, 1998.

[4.9] H. F. Arrand, T. M. Benson, A. Loni,  M. Kruger, M. Thoenissen, and H Lueth, "Self-aligned porous silicon optical waveguides", Electronics Letters , vol. 33(20), pp. 1742-1725, 1997.

[4.10] R. A. Soref, F. Navamar, and J. P. Lorenzo, "Optical waveguiding in single-crystal layer of germanium silicon grown on silicon", Optoelectronics Letters, vol. 15, pp. 270-272, 1990.

[4.11] S. F. Pesarik, G. V. Treyz, S. S. Iyer, and J. M. Halbout, "SiGe optical waveguides with 0.5db/cm losses for single mode fibre optic systems", Electronics Letters, vol. 28, pp. 159-160, 1990.

[4.12] A. Splett, J. Schmidtchen, B. Schüppert, and K. Petermann, "Low loss optical ridge waveguides in a strained GeSi epitaxial layer grown on silicon", Electronics Letters, vol. 26, pp. 1035-1036, 1990.

[4.13] Y. M. Liu, and P. R. Prucnal, "Deeply etched singlemode SiGe rib waveguides for Si based optoelectronic integration", Electronics Letters, vol. 28, pp. 1434-1435, 1990.

[4.14] B. Schüppert, , J. Schmidtchen, , A. Splett, , U. Fischer, , T. Zinke, , R. Moosburger, and K. Petermann, "Integrated Optics in Silicon and SiGe-Heterostructures", IEEE Journal of Lightwave Technology, vol. 14(10), no. 10, pp.2311-2323, 1996.

[4.15] L. Naval, , B. Jalali, , L. Gomelsky, and J. M. Lui, "Optimization of $Si_{1-x}Ge_x$/Si Waveguide Photodetectors Operating at $\lambda=1.3$ $\mu$m", IEEE Journal of Lightwave Technology, vol. 14(5), pp.787-797, 1996.

[4.16] B. Li, , G. Li, , E. Lui, , Z. Jiang, , J. Qie, and X. Wang, "Monolithic integration of a SiGe/Si modulator and multiple quantum well photodetector for 1.55 $\mu$m operation", Applied Physics Letters, vol. 73(24), pp. 3504-3505, 1998.

[4.17] T. Stoica, L. Vescan, and M. Goryll, "Electroluminescence of strained SiGe/Si selectively grown above the critical thickness for plastic relaxation", Journal of Applied Physics, vol. 83, pp. 3367-3373, 1998.

[4.18] L. C. Kimerling, "Silicon Microphotonics", Integrated Photonics Research (IPR), IFB1, 2002.

[4.19] O. Bisi, S. U. Campisano, L. Pavesi, and F. Priolo, "Silicon based microphotonics: from basics to application", IOS Press, 1999.

[4.20] H. Temkin, T. P. Pearsall, J. C. Bean, R. A. Logan, and S. Luryi, "$Ge_xSi_{1-x}$ strained layer superlattice waveguide photodetectors operating near 1.3$\mu$m", Applied Physics Letters, vol. 48, pp. 963-965, 1986.

[4.21] T. P. Pearsall, "Silicon-Germanium Alloys an Heterostructures: Optical and Electronic Properties, "CRC Critical Reviews in Solid State and Materials Sciences", vol. 15, pp. 551-600, 1989.

[4.22] E. Kasper, "Properties of strained and relaxed silicon germanium", INSPEC, 1995.

[4.23] R. A. Soref, and C. H, Perry, "Predicted band-gap of the new semiconductor SiGeSn", Journal of Applied Physics, vol. 69, pp539, 1991.

[4.24] E. D. Palik, (Editor).: 'Handbook of Optical Constants of Solids', Academic Press, 1985.

[4.25] B. R. B. Richard. A. Soref, "Electrooptical Effects in Silicon", IEEE Journal of Quantum Electronics, vol. QE-23, pp. 123-129, 1987.

[4.26] L. F. R. D. Lareau, L. Friedman, and R. A. Soref,: 'Waveguided electro-optical intensity modulation in a Si/Si1-xGex /Si heterojunction bipolar transistor', IEEE Electronics Letters, vol. 26(20), pp.1653-1655, 1990.

[4.27] T. P. Pearsall, "Silicon-Germanium Alloys an Heterostructures: Optical and Electronic Properties, "CRC Critical Reviews in Solid State and Materials Sciences", vol. 15, pp. 551-600, 1989.

[4.28] R. S. Fan, and R. B. Hooker, "Tapered Polymer Single-Mode Waveguides for Mode Transformation", IEEE Journal of Lightwave Technology, vol. 17(3), pp. 466-474, 1999.

[4.29] I. Moerman, P. Van Daele, and P. M. Demeester, "A Review on Fabrication Technologies for the Monolithic Integration of Tapers with III-V Semiconductor Devices", IEEE J. Selected Topics in Quantum Electronics, vol. 3(6), pp.1308-1320, 1997.

[4.30] G. Allen, C. T. Sullivan, J. R. Wendt, R. E. Smith, H. Q. Hou, and J. F. Klem, "Tapered Rib Adiabatic Following Fiber Couplers in Etched GaAs Materials for Monolithic Spot-Size Transformation", IEEE J. Selected Topics in Quantum Electronics, vol. 3(6), pp.1361-13201371, 1997.

[4.31] P. Sewell, T. M. Benson, and P. C. Kendall, "Rib Waveguide Spot-Size Transformers: Modal Properties", IEEE J. Lightwave Technology, vol. 17(5), pp. 848-856, 1999.

[4.32] S. S. Saini, V. Vusirikala, R. Whaley, F. G. Johnson, D. Stone, and M. Dagenais, "Compact Mode Expanded Lasers Using Resonant Coupling Between a 1.55 μm InGaAsP Tapered Active Region and an Underlying Coupling Waveguide", IEEE Photonics Technology Letters, vol. 10(9), pp. 1232-1234, 1998.

[4.33] S. C. Greedy, H. F. Arrand, P. D. Sewell, and  T. M. Benson, "Fibre Coupling to SiGe Optoelectronic Devices",  IEE Proceedings – part J, vol. 147(6), pp. 391-394, 2000.

# Chapter 5    Analysis  of  Waveguides  of  Non-Rectangular  Cross Section

The ubiquitous rib waveguide is now found in almost all modern OEICs. In its simplest form the rib waveguide is a symmetrical, passive and longitudinally invariant device performing the task of a basic signal carrier. Using the rib waveguide as a base geometry has led to the development of passive and active devices performing a variety of roles that readily lend themselves to integration. The removal of symmetry in the transverse plane allows the rib to perform as a passive polarization rotator, [5.1]-[5.3].The inclusion of active layers in the rib region allow for the realization of photodetectors, [5.4]-[5.9], and lasers, [5.10]-[5.11].

In this chapter a novel implementation of the SI method is developed for the analysis of rib waveguides of arbitrary cross section. Two approaches are presented; the first, employing a stair-case approximation to the non-rectangular rib wall and the second treating the rib wall exactly.

## 5.1   Introduction

The optical characteristics of rib waveguides have been considered extensively in the literature and are generally considered to be ideal, i.e. rectangular with vertical side walls, for analysis purposes. However the fabrication process may lead to a physical device with a transverse cross section that is non-rectangular, [5.12]-[5.15]. The

resulting real waveguide generally has sloped walls resulting in a trapezoidal cross section. Figure 5-1 illustrates the transverse profiles of semiconductor rib waveguides that are typically produced by various etching solutions on GaAs. Rib waveguides of non-rectangular cross sections may also be required by design for the provision of beneficial electronic effects in active devices, such as reducing the threshold current of a laser device through a reduction in the waveguide width, [5.16]. The analysis of non-rectangular geometries, although seemingly important, has received little attention in the literature. A few results have been published, [5.17]-[5.19], the former employing an equivalent circuit approach and the latter an effective index method. However, these approaches suffer when the device is close to cut-off in the outer slab regions.
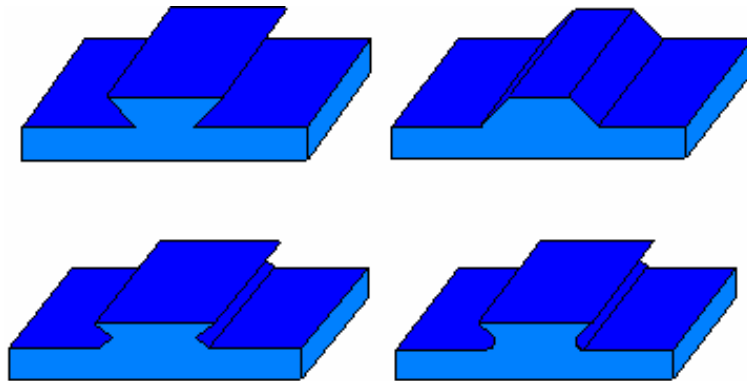


**Figure 5-1** Waveguide profiles produced by various etching solutions on GaAs.

## 5.2   Theoretical Development

In developing the theory, the trapezoidal rib waveguide of figure 5-2 will be used as an illustrative example. In chapter 3, the following expression
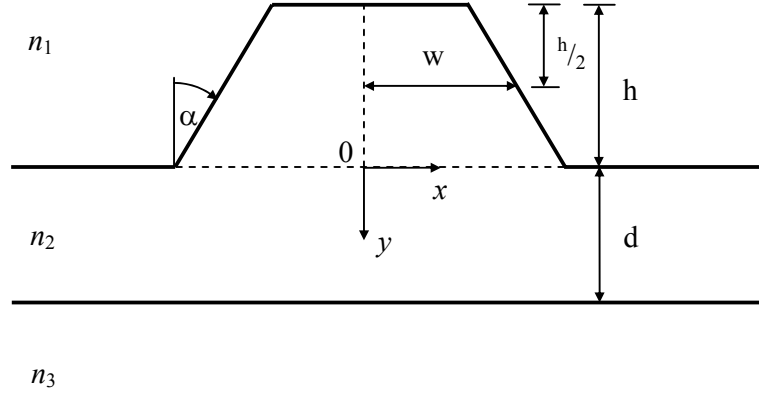
**Figure 5-2** Trapezoidal rib waveguide geometry.

$$\int_{-W}^{W} E_-^* \left[ \frac{\partial E}{\partial y} \right]_- dx = \frac{1}{2\pi} \int_{-\infty}^{+\infty} \phi_+^* \left[ \frac{\partial \phi}{\partial y} \right]_+ ds \qquad (5.1)$$

followed as a result of the application of the variational boundary condition, equation (3.21, §3.6). With reference to the circuit analogues introduced earlier (§3.8), the left hand side of equation (5.1)can be re-written as

$$\int_{-W}^{W} E_-^* \left[ \frac{\partial E}{\partial y} \right]_- dx = \int_{-W}^{W} E_-^* H_- dx = \int_{-W}^{W} E_-^* E_- \frac{H_-}{E_-} dx = \int_{-W}^{W} E_-^* E_- Y = Y^{rib} \qquad (5.2)$$

Equation (5.2) now effectively represents the admittance looking upwards into the base of the rib section of the waveguide. The rib may now be thought of as a non-uniform terminated transmission line. Two formulations to the problem are described

95

in the following two sections. The first uses a stair-case approximation to the rib wall and treats the rib in a manner analogous to that of a multi-section transmission line. The second uses an exact representation of the rib wall avoiding the need for discretisation, and the rib is treated as a tapered transmission line that models the continuous variation found in the practical structure.

## 5.2.1  Stair-cased Formulation

A stair-case approximation to the sloped wall of the rib waveguide is illustrated in figure 5-3(a) and is used to represent the true transverse profile of the rib waveguide . The rib is now treated as a multi-section transmission line of *n* sections, figure 5-3(b).
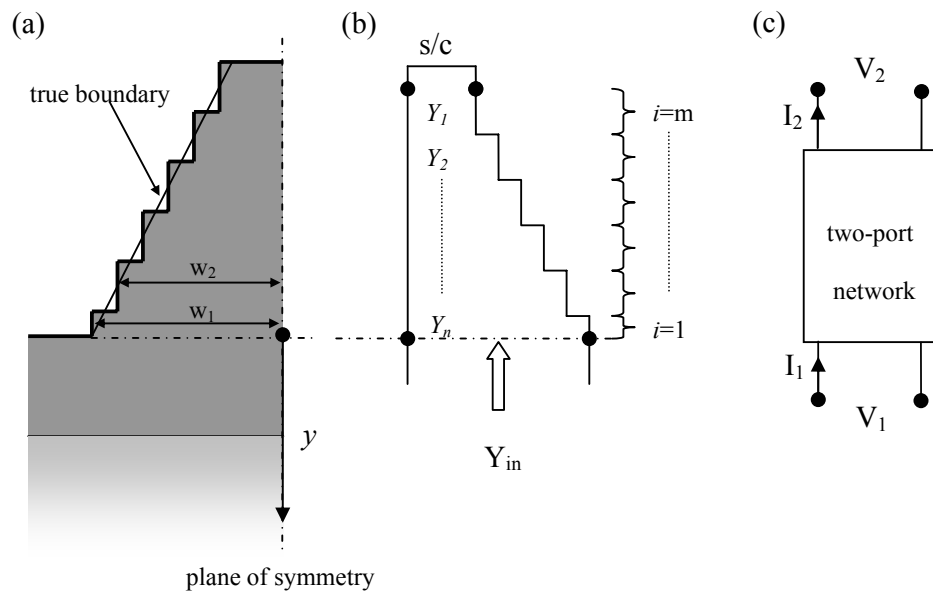


**Figure 5-3** Trapezoidal rib waveguide and its transmission line equivalent.

Each section may be described by a four port, two terminal network representation, as shown in Figure 5-1(c), where $V_1I_1$ and $V_2I_2$ represent the equivalent modal voltages/currents on the input and output ports respectively, i.e. the bottom and top surfaces of each section. The equivalent voltage and current at the input may then be related to those at the output by a transfer matrix, such that

$$\begin{bmatrix} V_1 \\ I_1 \end{bmatrix} = \begin{bmatrix} A & B \\ C & D \end{bmatrix} \cdot \begin{bmatrix} V_2 \\ I_2 \end{bmatrix}$$
(5.3)

At the discontinuities between the waveguide/transmission line sections TE-TM mode conversion is known to be small, [5.20] and so is ignored. The effect of each discontinuity can then be modelled by an equivalent transformer network, [5.21]-[5.23]. Considering the case of only a forward travelling (-ve $y$ direction) field, figure 5-4, illustrates a transformer network representation of one discontinuity, with section 1 supporting $m$ modes and section 2 supporting $n$ modes. The V's represent the equivalent modal voltages and the I's the equivalent modal currents. The turn's ratio, T, of the primary and secondary of each equivalent transformer is effectively the overlap between each mode in section 1 with all modes in section 2 such that

$$T_{1,2} = \langle \varphi_1 \varphi_2 \rangle = \int_{-w_2}^{+w_2} \varphi_1 \varphi_2 \ dx$$
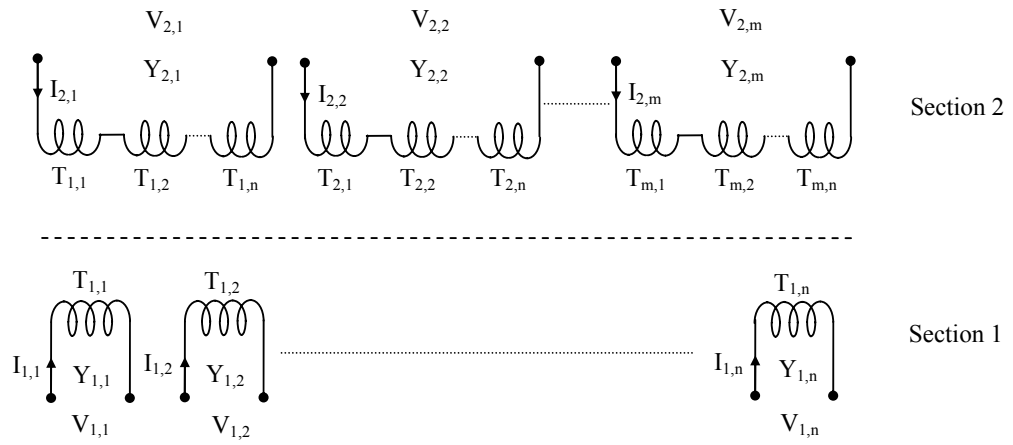(5.4)

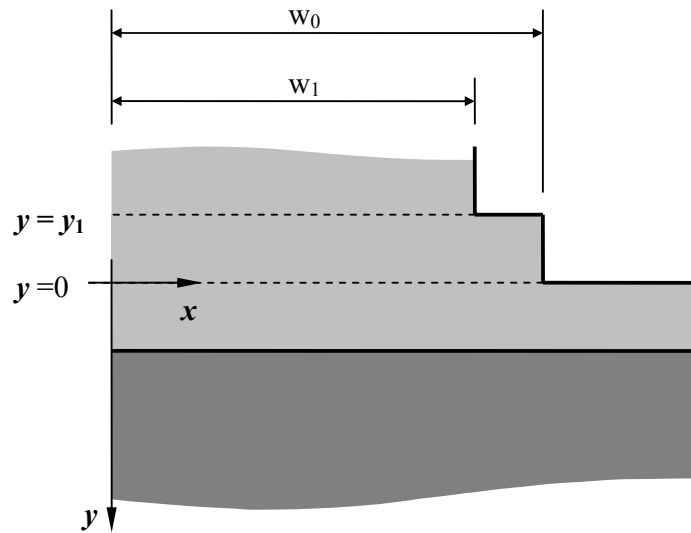**Figure 5-4** Transformer representation of a step discontinuity.



**Figure 5-5** Schematic illustration of the first step junction at the base of the rib.

where $\pm w_2$ denote the width of the narrower section and $\varphi_1, \varphi_2$ the voltage distributions in the respective section.

Consider now the case of a sloped wall rib waveguide that has been stair-cased with $m$ steps. Figure 5-5 illustrates the first step junction at the base of the rib with the electric field distribution across the base of the rib, $E(x,0)$, being given by

$$E(x,0) = \overline{\varphi}_0^{\ \mathbf{T}}(x,\mathbf{w}_0)\overline{\mathbf{V}}_0 \qquad (5.5)$$

and the derivative of the field with respect to $y$ is then given by

$$\frac{\partial E}{\partial y}(x,0) = \overline{\varphi}_0^{\ \mathbf{T}}(x,\mathbf{w}_0)\overline{\mathbf{I}_0} \qquad (5.6)$$

In (5.5) and (5.6) the vector of $N$ basis terms, $\overline{\varphi}_0$, used in the field expansion has elements

$$\varphi_{n,0} = \sqrt{\frac{2}{\mathbf{w}_0}}\cos\left(\frac{(2n+1)\pi x}{2\mathbf{w}_0}\right) \qquad (5.7)$$

where $n$ is the $n^{th}$ term, $\overline{\mathbf{V}}_0$ and $\overline{\mathbf{I}}_0$ are the vectors of equivalent voltage and current amplitudes at $y=0$ and $w_0$ is the width at the base of the rib. $\overline{\mathbf{V}}_1$ and $\overline{\mathbf{I}}_1$ on the top of the first step at $y = y_1$ are then obtained through the application of (5.3) such that

$$\begin{bmatrix} \overline{V}_1 \\ \overline{I}_1 \end{bmatrix} = \begin{bmatrix} \overline{\overline{\mathbf{A}}} & \overline{\overline{\mathbf{B}}} \\ \overline{\overline{\mathbf{C}}} & \overline{\overline{\mathbf{D}}} \end{bmatrix} \cdot \begin{bmatrix} \overline{V}_0 \\ \overline{I}_0 \end{bmatrix} \qquad (5.8)$$

$\overline{\overline{A}}, \overline{\overline{B}}, \overline{\overline{C}},$ and $\overline{\overline{D}}$ are diagonal matrices, derived from standard transmission line theory, whose elements are given by

$$A_{n,n} = D_{n,n} = \cos\left(\gamma_{n,0}\Delta_0\right)$$

$$B_{n,n} = \frac{\sin\left(\gamma_{n,0}\Delta_0\right)}{\gamma_{n,0}} \tag{5.9}$$

$$C_{n,n} = -\gamma_{n,0}\sin\left(\gamma_{n,0}\Delta_0\right)$$

where

$$\gamma_{n,0} = k_0^2 - \beta^2 - \left(\frac{(2n+1)\pi}{2w_0}\right)^2 \tag{5.10}$$

$E(x, y_1)$ and $\dfrac{\partial E}{\partial y}(x, y_1)$ at the top of the first step are thus given by

$$\begin{bmatrix} E(x, y_1) \\ \dfrac{\partial E}{\partial y}(x, y_1) \end{bmatrix} = \begin{bmatrix} \overline{\varphi_0}^T & 0 \\ 0 & \overline{\varphi_0}^T \end{bmatrix} \begin{bmatrix} \overline{\overline{A}} & \overline{\overline{B}} \\ \overline{\overline{C}} & \overline{\overline{D}} \end{bmatrix} \cdot \begin{bmatrix} \overline{V_0} \\ \overline{I_0} \end{bmatrix} \tag{5.11}$$

Applying the overlap given in (5.4) results in

$$\begin{bmatrix} E(x,y_1) \\ \dfrac{\partial E}{\partial y}(x,y_1) \end{bmatrix} = \begin{bmatrix} \overline{\varphi_1}^T & 0 \\ 0 & \overline{\varphi_1}^T \end{bmatrix} \begin{bmatrix} \overline{\overline{T_{1,0}}} \\ \overline{\overline{T_{1,0}}} \end{bmatrix} \begin{bmatrix} \overline{\overline{A}} & \overline{\overline{B}} \\ \overline{\overline{C}} & \overline{\overline{D}} \end{bmatrix} \cdot \begin{bmatrix} \overline{V_0} \\ \overline{I_0} \end{bmatrix} \tag{5.12}$$

Therefore applying the process recursively for all steps gives

$$\begin{bmatrix} E(x,y_m) \\ \dfrac{\partial E}{\partial y}(x,y_m) \end{bmatrix} = \begin{bmatrix} \overline{\varphi_m}^T & 0 \\ 0 & \overline{\varphi_m}^T \end{bmatrix} \begin{bmatrix} \overline{\overline{A_m}} & \overline{\overline{B_m}} \\ \overline{\overline{C_m}} & \overline{\overline{D_m}} \end{bmatrix} \begin{bmatrix} \overline{\overline{T_{m,m\text{-}1}}} \\ \overline{\overline{T_{m,m\text{-}1}}} \end{bmatrix} \cdots$$

$$\cdots \begin{bmatrix} \overline{\overline{A_1}} & \overline{\overline{B_1}} \\ \overline{\overline{C_1}} & \overline{\overline{D_1}} \end{bmatrix} \begin{bmatrix} \overline{\overline{T_{m,m\text{-}1}}} \\ \overline{\overline{T_{m,m\text{-}1}}} \end{bmatrix} \begin{bmatrix} \overline{\overline{A_0}} & \overline{\overline{B_0}} \\ \overline{\overline{C_0}} & \overline{\overline{D_0}} \end{bmatrix} \begin{bmatrix} \overline{V_0} \\ \overline{I_0} \end{bmatrix} \tag{5.13}$$

$$= \begin{bmatrix} \overline{\varphi_m}^T & 0 \\ 0 & \overline{\varphi_m}^T \end{bmatrix} \begin{bmatrix} \overline{\overline{\alpha}} & \overline{\overline{\beta}} \\ \overline{\overline{\gamma}} & \overline{\overline{\delta}} \end{bmatrix} \cdot \begin{bmatrix} \overline{V_0} \\ \overline{I_0} \end{bmatrix}$$

But it is required that $E(x,y_m)=0$, therefore

$$\overline{\overline{\alpha}}\,\overline{V_0} + \overline{\overline{\beta}}\,\overline{I_0} = 0 \tag{5.14}$$

Below the base of the rib the current and voltage are related through

$$\overline{I} = \overline{\overline{Y}}\,\overline{V} \tag{5.15}$$

where

$$Y_{i,j} = \int_0^\infty \varphi_i(s)\varphi_j(s)\Gamma(s)\,ds \tag{5.16}$$

and

$$\varphi_i(s) = \int_0^\infty \sqrt{\frac{2}{\pi}} \cos(sx)\varphi_{i,0}(x)\,ds \tag{5.17}$$

$\Gamma(s)$ is the standard plane wave response function of the layered substrate, (§3.6).

From (5.14) and (5.15)

$$\left(\overline{\overline{Y}} + \overline{\overline{\beta}}^{-1}\overline{\overline{\alpha}}\right)\overline{V_0} = 0$$

$$\Rightarrow \left(\overline{\overline{\beta Y}} + \overline{\overline{\alpha}}\right)\overline{V_0} = 0 \tag{5.18}$$

(5.18) is thus solved for $\beta$ for the condition

$$\left|\overline{\overline{\beta Y}} + \overline{\overline{\alpha}}\right| = 0 \tag{5.19}$$

and forms the principal result of this section.

## 5.2.2 Exact Formulation

The following presents the theoretical development of an SI based approach whereby the sloping wall of the waveguide is treated in an exact manner and w is now a continuous function of $y,\ w(y)$.

Defining

$$E(x,y) = \overline{\varphi}^{\mathrm{T}}\left(x, w(y)\right)\overline{A(y)} \tag{5.20}$$

and

$$\frac{\partial E}{\partial y}(x,\mathrm{w}) = \overline{\varphi}^{\mathrm{T}}\left(x, w(y)\right)\left(\overline{\overline{-j\gamma}}\right)^{\mathrm{D}}\overline{A(y)} \tag{5.21}$$

where the superscript D is taken to denote a diagonal matrix

$$\varphi_n(x,\mathrm{w}) = \sqrt{\frac{2}{w(y)}}\cos\left(\frac{n\pi x}{2w(y)}\right) \tag{5.22}$$

and

$$\gamma_n^2 = k^2(y) - \beta^2 - \left(\frac{n\pi}{2w(y)}\right)^2 \tag{5.23}$$

where, again, where $n$ is the $n^{th}$ term of the field expansion. It is required that $E$ be a solution to the scalar wave equation such that

$$\left(\nabla^2 + k^2\right)E = 0 \tag{5.24}$$

From (5.21)

$$\frac{d^2 E}{dy^2} = \frac{d}{dy}\left( \overline{\varphi}^{\mathrm{T}}\left(x, w(y)\right)\left(\overline{\overline{-j\gamma}}\right)^{D}\overline{A(y)}\right)$$

(5.25)

$$= \overline{\varphi'}^{\mathrm{T}}\left(\overline{\overline{-j\gamma}}\right)^{D}\overline{A} + \overline{\varphi}^{\mathrm{T}}\left(\overline{\overline{-j\gamma}}\right)^{\prime D}\overline{A(y)} + \overline{\varphi}^{\mathrm{T}}\left(\overline{\overline{-j\gamma}}\right)^{D}\overline{A'(y)}$$

and

$$\left(k^2 - \beta^2 + \frac{d^2}{dx^2}\right)E = \varphi^{\mathrm{T}}\left(x, w\right)\left(\overline{\overline{-\gamma^2}}\right)^{D}\overline{A(y)}$$

(5.26)

which implies that

$$\overline{\varphi'}^{\mathrm{T}}\left(\overline{\overline{-j\gamma}}\right)^{D}\overline{A} + \overline{\varphi}^{\mathrm{T}}\left(\overline{\overline{-j\gamma}}\right)^{\prime D}\overline{A(y)} + \overline{\varphi}^{\mathrm{T}}\left(\overline{\overline{-j\gamma}}\right)^{D}\overline{A'(y)} = 0$$

(5.27)

Applying the test function

$$\int_{0}^{w(y)} \overline{\varphi}\left(x, w(y)\right)dx$$

(5.28)

to (5.27) yields

$$\overline{P(y)}\left(\overline{\overline{-j\gamma}}\right)^{D}\overline{A} + \left(\overline{\overline{-j\gamma'}}\right)^{D}\overline{A} + \left(\overline{\overline{-j\gamma}}\right)^{D}\overline{A'} = 0$$

(5.29)

where P(y) is a square matrix whose elements are given by

$$P_{nm} = \int\limits_{0}^{w(y)} \varphi_n\left(x, w(y)\right) \cdot \frac{d}{dy} \varphi_m\left(x, w(y)\right) dx \tag{5.30}$$

Equations (5.20) and (5.21)

$$\overline{\varphi}^{\mathrm{T}} \left(\overline{\overline{-j\gamma}}\right)^{\mathrm{D}} \overline{\mathrm{A}} = \overline{\varphi'}^{\mathrm{T}} \overline{\mathrm{A}} + \overline{\varphi}^{\mathrm{T}} \overline{\mathrm{A}'} \tag{5.31}$$

implying that

$$\left(\overline{\overline{-j\gamma}}\right)^{\mathrm{D}} \overline{\mathrm{A}(y)} = \overline{\overline{\mathrm{P}(y)}}\,\overline{\mathrm{A}(y)} + \overline{\mathrm{A}'(y)} \tag{5.32}$$

Separating forward and backward modes, equation (5.29) gives

$$\overline{\overline{\mathrm{P}(y)}} = \left[ \left(\overline{\overline{-j\gamma}}\right)^{\mathrm{D}} \overline{\mathrm{A}_{\mathrm{f}}} + \left(\overline{\overline{+j\gamma}}\right)^{\mathrm{D}} \overline{\mathrm{A}_{\mathrm{r}}} \right] + \left[ \left(\overline{\overline{-j\gamma'}}\right)^{\mathrm{D}} \overline{\mathrm{A}_{\mathrm{f}}} + \left(\overline{\overline{+j\gamma'}}\right)^{\mathrm{D}} \overline{\mathrm{A}_{\mathrm{f}}} \right] \\ + \left[ \left(\overline{\overline{-j\gamma}}\right)^{\mathrm{D}} \overline{\mathrm{A}'_{\mathrm{f}}} + \left(\overline{\overline{+j\gamma}}\right)^{\mathrm{D}} \overline{\mathrm{A}'_{\mathrm{f}}} \right] \tag{5.33}$$

and similarly equation (5.31) gives

$$\left(\overline{\overline{-j\gamma}}\right)^{\mathrm{D}} \overline{\mathrm{A}_{\mathrm{f}}} + \left(\overline{\overline{+j\gamma}}\right)^{\mathrm{D}} \overline{\mathrm{A}_{\mathrm{r}}} = \overline{\overline{\mathrm{P}(y)}}\left(\overline{\mathrm{A}_{\mathrm{f}}} + \overline{\mathrm{A}_{\mathrm{r}}}\right) + \overline{\mathrm{A}'_{\mathrm{f}}} + \overline{\mathrm{A}'_{\mathrm{r}}} \tag{5.34}$$

Combining (5.33) and (5.34) results in the matrix equation

$$\left( \begin{array}{cc} \left(\overline{\overline{-j\gamma}}\right)^{D} & \left(\overline{\overline{+j\gamma}}\right)^{D} \\ \overline{\overline{I}} & \overline{\overline{I}} \end{array} \right) \left( \begin{array}{c} \overline{A'_{f}} \\ \overline{A'_{r}} \end{array} \right) =$$

$$\left( \begin{array}{cc} -\overline{\overline{P(y)}}\left(\overline{\overline{-j\gamma}}\right)^{D} -\left(\overline{\overline{-j\gamma}}\right)^{D} -\left(\overline{\overline{\gamma}}\right)^{D} & -\overline{\overline{P(y)}}\left(\overline{\overline{+j\gamma}}\right)^{D} -\left(\overline{\overline{+j\gamma}}\right)^{D} -\left(\overline{\overline{\gamma}}\right)^{D} \\ -\overline{\overline{P(y)}}+\left(\overline{\overline{-j\gamma}}\right)^{D} & -\overline{\overline{P(y)}}+\left(\overline{\overline{+j\gamma}}\right)^{D} \end{array} \right) \tag{5.35}$$

Further, defining the equivalent voltage and current amplitude vectors $\overline{V}$ and $\overline{I}$ such that

$$\overline{V}(y) = \overline{A_{f}(y)} + \overline{A_{r}(y)} \quad \text{and} \quad \overline{I}(y) = \left(\overline{\overline{-j\gamma}}\right)^{D} \left(\overline{A_{f}(y)} + \overline{A_{r}(y)}\right) \tag{5.36}$$

Equation (5.35) may be re-written as

$$\left( \begin{array}{cc} \overline{\overline{0}} & \overline{\overline{I}} \\ \overline{\overline{I}} & \overline{\overline{0}} \end{array} \right) \left( \begin{array}{c} \dfrac{d}{dy}\overline{V} \\ \dfrac{d}{dy}\overline{I} \end{array} \right) = \left( \begin{array}{cc} -\left(\overline{\overline{\gamma^{2}}}\right)^{D} & -\overline{\overline{P(y)}}-\left(\overline{\overline{\gamma'/\gamma}}\right)^{D} \\ -\overline{\overline{P(y)}} & \overline{\overline{I}} \end{array} \right) \left( \begin{array}{c} \overline{V(y)} \\ \overline{I(y)} \end{array} \right) \tag{5.37}$$

and subsequently as

$$\left( \begin{array}{c} \dfrac{d}{dy}\overline{V(y)} \\ \dfrac{d}{dy}\overline{I(y)} \end{array} \right) = - \left( \begin{array}{cc} \overline{\overline{P(y)}} & -\overline{\overline{I}} \\ \left(\overline{\overline{\gamma^{2}}}\right)^{D} & -\overline{\overline{P(y)}}-\left(\overline{\overline{\gamma'/\gamma}}\right)^{D} \end{array} \right) \left( \begin{array}{c} \overline{V(y)} \\ \overline{I(y)} \end{array} \right) \tag{5.38}$$

(5.38) further implies that

$$\begin{pmatrix} \overline{V(y)} \\ \overline{I(y)} \end{pmatrix} = e^{-\int \left( \frac{\overline{\overline{P(y)}}}{(\overline{\gamma^2})^D} \ \frac{\overline{\overline{i}}}{\overline{P(y)} + \left(\overline{\gamma'}/\gamma\right)^D} \right) dy} \begin{pmatrix} \overline{V(0)} \\ \overline{I(0)} \end{pmatrix}$$

(5.39)

Finally giving at the top of the rib $(y = H)$

$$\begin{pmatrix} \overline{V(y)} \\ \overline{I(y)} \end{pmatrix} \bigg|_{y=H} = \begin{pmatrix} \overline{\overline{\alpha}} & \overline{\overline{\beta}} \\ \overline{\overline{\gamma}} & \overline{\overline{\delta}} \end{pmatrix} \begin{pmatrix} \overline{V(0)} \\ \overline{I(0)} \end{pmatrix}$$

(5.40)

It is required required that $E(x, y = H) = 0$, therefore (5.40) may finally be expressed as

$$\overline{\overline{\alpha}}\overline{V_0} + \overline{\overline{\beta}}\overline{I_0} = 0$$

(5.41)

in a manner that exactly mimics (5.14). Below the rib the problem is treated in exactly the same manner as for the stair-cased approach described in the previous section, resulting in the final matrix equation

$$\left| \overline{\overline{\beta}}\overline{\overline{Y}} + \overline{\overline{\alpha}} \right| = 0$$

(5.42)

which is the principal result of this section.

The following section will apply and compare the two approaches described above as well as drawing comparisons with results provided by a purely numerical approach.

## 5.3   Numerical Results

Throughout the following the rib waveguide of figure 5-2 was used for analysis purposes. The waveguide is a typical example of a rib waveguide fabricated in a GaAs/AlGaAs material system, with $n_2 = 3.44$ and $n_3 = 3.40$ at a wavelength of $\lambda=1.15\mu m$. The wet etching processes employed in the fabrication of these guides typically result in non-rectangular cross sections as described earlier (§5.1). When determining the effect of the angle of slope, ($\alpha$), the width of the rib at half its height was fixed. Using this approach the cross-sectional area of the rib remains constant with side wall slope and so only the effects on the optical properties of the guide due to change in wall slope are modelled.

An initial vectorial finite difference simulation was carried out in order to ascertain the validity of the polarisation assumptions at the imposition of the effective penetration depths. Figure 5-6 depict the optical field distributions for the major and minor field components. The analysis was implemented with a rectangular mesh and hence the sloped wall was approximated in a stair-cased manner. As well as the singularities present at the re-entrant corners, singular fields are also observed along the stair-cased side walls and are a result of the approximation to the true structure.
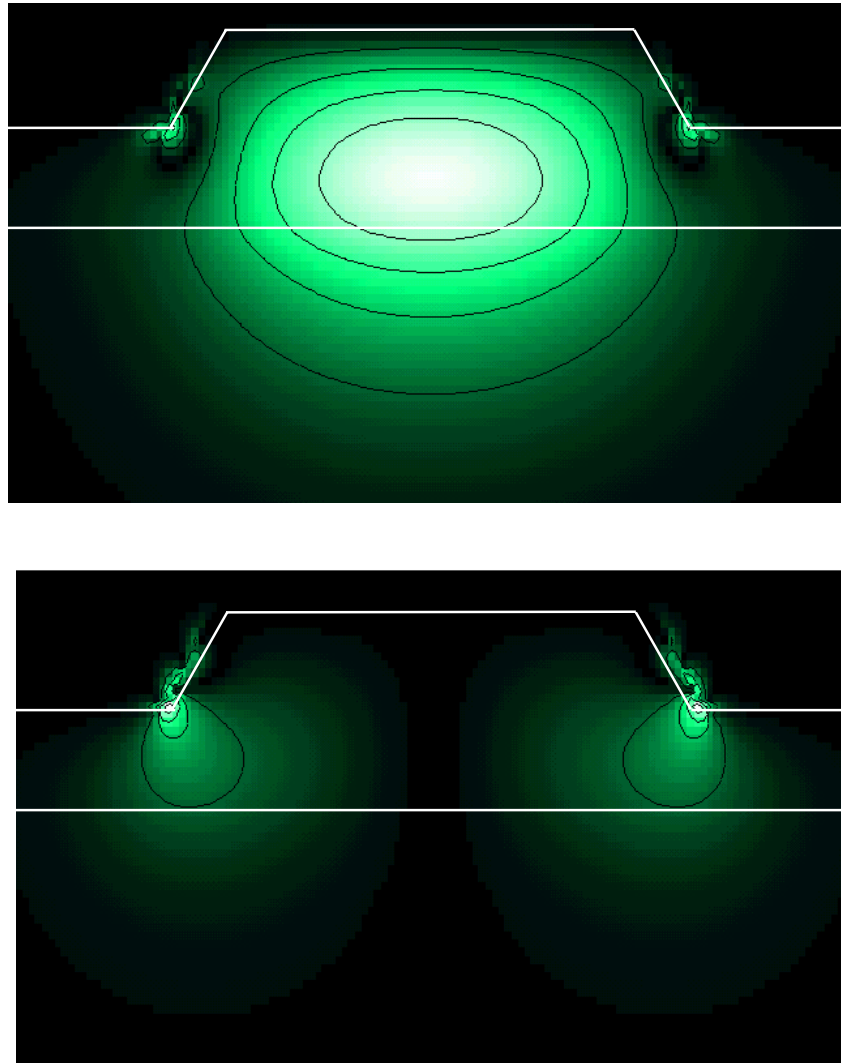
**Figure 5-6** Optical field distributions for the fundamental mode of a trapezoidal rib waveguide with a 30° side wall slope; (a) principal field component and (b)minor field component. The white lines outline the true physical boundaries of the structure where H=0.5μm, D=0.5μm and the mid-height width = 3.0μm.

The vectorial analysis revealed that the fields supported are essentially polarised and so further comparisons will be drawn with a semi-vectorial finite difference scheme. For the case of the stair-cased SI approach, the convergence of the normalised propagation constant, b, with the number of steps used in the stair-case

109

approximation was examined. Figure 5-7 illustrates the results and the difference in

b between computed for 10 steps and 10000 steps equate to a difference in the fifth

decimal place of β, well within the accuracy of the standard SI method.

Computational times for the rib approximated by 100 stair-case steps were <10

seconds. For the following SI simulations the rib was therefore approximated with

100 steps retaining computational efficiency without loss of accuracy.

Table 5-1 gives a comparison of the normalised propagation constants, b, for the

fundamental quasi-TE of the rib waveguide described above. Two sets of results are

given, those obtained by the SI method and those computed with two SV-FD

schemes of increasing accuracy. Good agreement is observed between the SI method

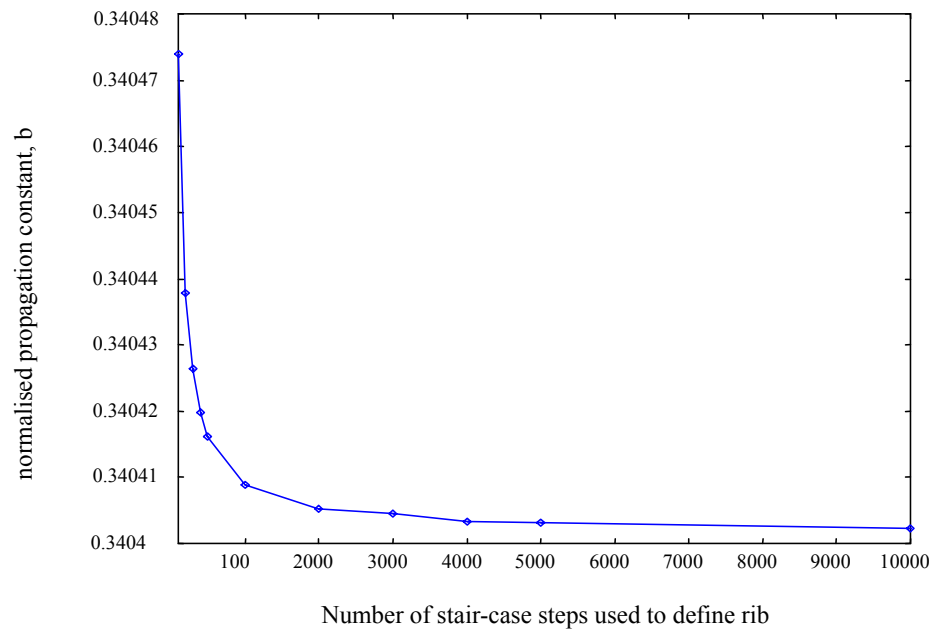and those obtained by the more accurate SV-FD scheme.



**Figure 5-7** Convergence of the normalised propagation constant, b, with number of steps used to

stair-case the sloping side wall as computed by the SI method. The rib waveguide is as depicted in

figure 5-2 with; h=0.5μm, d=0.5μm, w=3.0μm, $n_2$=3.44, $n_3$=3.40, λ=1.15μm and α=45°.

| Slope $\alpha°$ | SI method | mesh size | |
|---|---|---|---|
| | | 200x0.02μm | 400x0.01μm |
| 0 | 0.3247 | 0.3272 | 0.3265 |
| 10 | 0.3278 | 0.3297 | 0.3291 |
| 20 | 0.3310 | 0.3319 | 0.3314 |
| 30 | 0.3343 | 0.3338 | 0.3333 |
| 40 | 0.3382 | 0.3354 | 0.3349 |

**Table 5-1** Comparison of the normalised propagation constants, b, obtained via the SI method versus two semi-vectorial finite differences schemes of increasing accuracy. The rib waveguide is as depicted in figure 5-2 with; h=0.5μm, d=0.5μm, w=3.0μm, $n_2$=3.44, $n_3$=3.40 and λ=1.15μm.

Figure 5-8 illustrates the normalised propagation constants versus side wall slope obtained by single and multi-term SI methodologies and compared to those obtained using a semi-vectorial finite difference scheme good agreement is obtained between the SV-FD scheme and the SI approaches using several terms in the field expansion in the rib.

Figure 5-9 depicts the variation in the normalised propagation constant, b, with the overall rib height, H, such that $D+H = 1.0\mu m$ for side wall slopes of 0°, 10°, 20° and 30°. The effect of increasing the height of the rib leads to a reduction in b as expected. The effect of increasing the side wall slope, α, is to widen the base of the rib and as the field is predominant in the region of the rib base the field effectively sees more of the higher index material resulting in an overall increase in b. Finally, figure 5-10 illustrates the optical field distributions predicted by the SI method for the cases of $\alpha = 0°$, 30° and 50°.
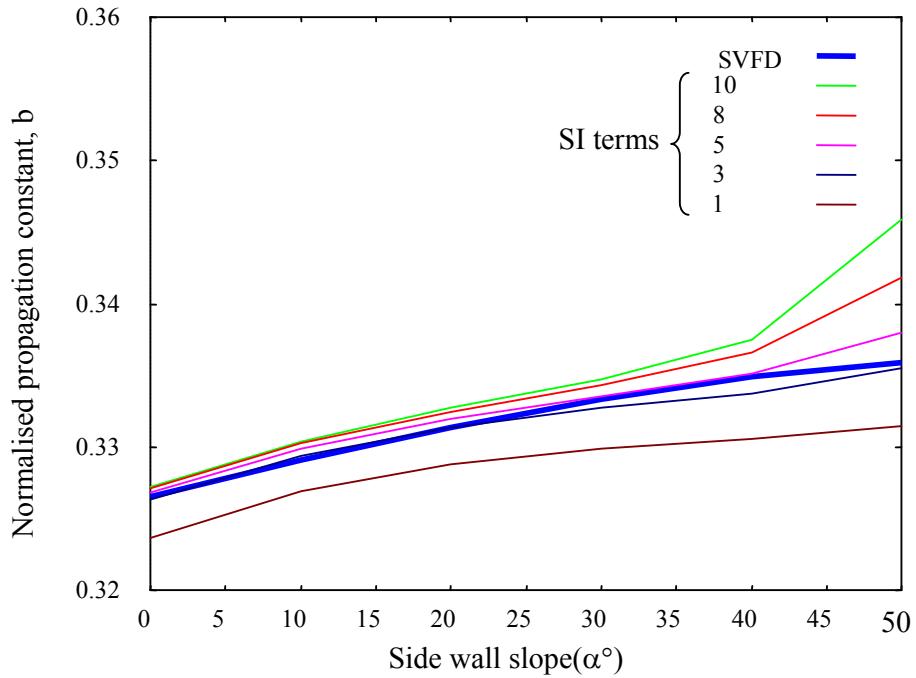
**Figure 5-8** Normalised propagation constants for the fundamental quasi-TE mode of the waveguide of Figure 5-2, versus side wall slope; where H=0.5μm, D=0.5μm and the mid-height width = 3.0μm.
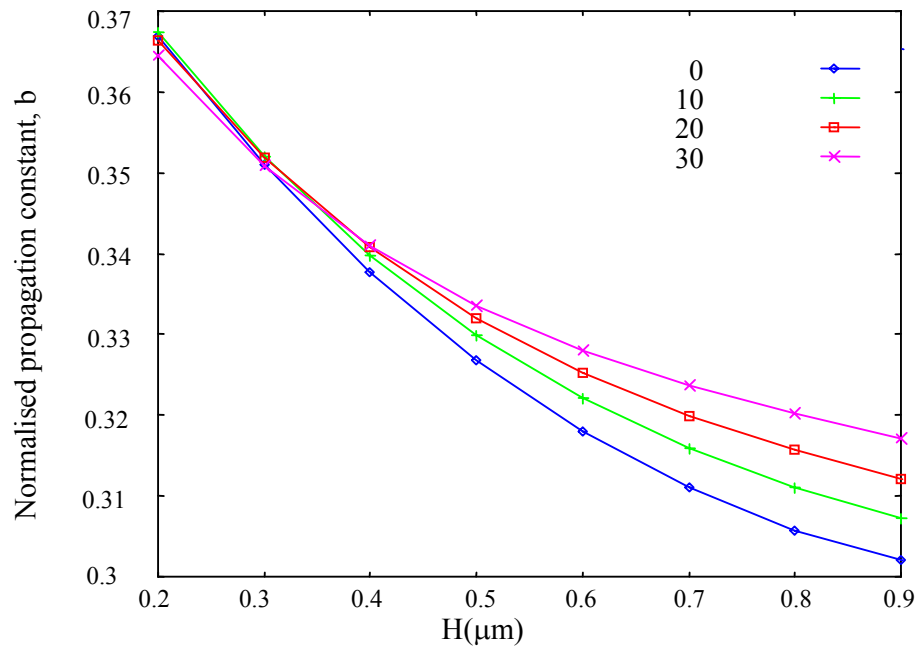


**Figure 5-9** Normalised propagation constants for the fundamental quasi-TE mode of the waveguide, of Figure 5-2, versus the full height of the rib; where H+D = 1.0μm and the mid-height width = 3.0μm.
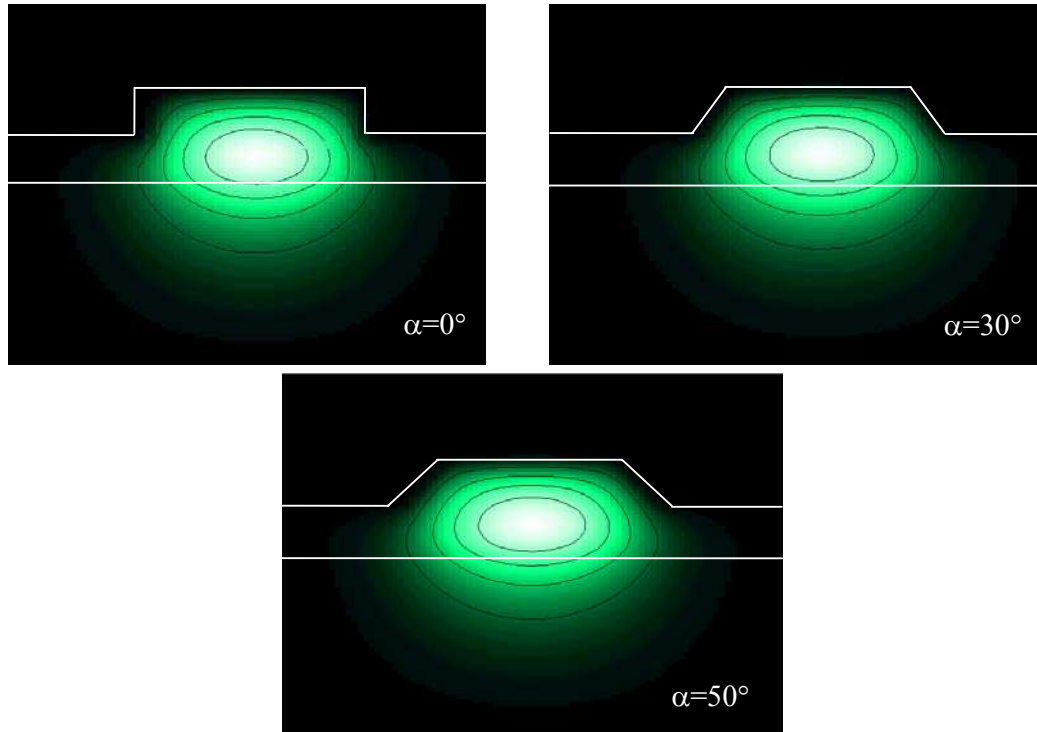
**Figure 5-10** Optical field distributions of the fundamental quasi-TE mode for side wall slopes of $\alpha=0°$, 30°, 50°. The solid white lines schematically illustrate the physical structure.

## 5.4  Conclusions

This chapter has introduced a novel extension to the standard SI method that generalises it to the analysis of rib waveguides of non-rectangular cross section. The approach is shown to be accurate, for those cases where the field remains essentially polarised, through comparison with benchmark numerical methods whilst remaining computationally efficient. Although restricted to problems possessing lateral symmetry, the approach provides for a highly practical tool for the analysis of trapezoidal rib waveguides that are commonly found in optoelectronic integrated circuits.

## 5.5 References

[5.1] B. M. A. Rahman, N. Somasiri, M. Rajarajan, and K. T. V. Grattan, "Compact passive polarization converter using slanted semiconductor rib waveguides", Proc. Integrated Photonics Research Conf., Québec, Canada, pp. 60-62, 2000.

[5.2] B. M. A. Rahman, S. S. A. Obayya, M. Rajarajan, K. T. V. Grattan, and H. A. El-Mikathi, "Design and characterization of compact single-section passive polarization rotator", IEEE Journal of Lightwave Technology, vol. 19(4), pp. 512-519, 2001.

[5.3] N. Somasiri, B. M. A. Rahman, and S. S. A. Obayya, "Fabrication tolerance stucy of a compact passive polarization rotator", IEEE Journal of Lightwave Technology, vol. 20(4), pp. 751-757, 2002.

[5.4] S. Luryi, T. P. Pearsall, H. Temkin, and J. C. Bean, "Waveguide infrared photodetectors on a silicon chip", IEEE Electronics Device Letters, vol. 7, pp. 104-107, 1986.

[5.5] H. Temkin, T. P. Pearsall, J. C. Bean, R. A. Logan, and S. Luryi, "Ge$x$Si1-$x$ strained layer superlattice waveguide photodetectors operating near 1.3μm", Applied Physics Letters, vol. 48(15), pp. 963-965, 1986.

[5.6] B. Jalali, A. F. J. Levi, F. Ross, and E. A. Fitzgerald, "SiGe waveguide photodetectors grown by rapid thermal chemical vapour deposition", Electronics Letters, vol. 28(3), pp. 269-271, 1992.

[5.7] B. Jalali, L. Naval, and A. F. J. Levi, "Silicon based receivers for optical data links", IEEE Journal of Lightwave Technology, vol. 12, pp. 930-935, 1994.

[5.8] A. Densmore, and P. E. Jessop, "A quantum-well waveguide photodetector for high-precision wavelength monitoring about 1.55μm", IEEE Photonics Technology Letters, vol. 11(12), pp. 1653-1655, 1999.

[5.9] G. S. Kinsey, J. C. Campbell, and A. G. Dentai, "Waveguide avalanche photodiode operating at 1.55μm with a gain-bandwidth product of 320 GHz", IEEE Photonics Technology Letters, vol. 13(8), pp. 842-844, 1999.

[5.10] G. Vawter, R. E. Smith, H. Hou, J. R. Wendt, "Semiconductor laser with tapered-rib adiabatic-folowing fiber coupler for expanded output-mode diameter", IEEE Photonics Technology Letters, vol. 9(4), pp. 425-427, 1997.

[5.11] S. Sujecki, L. Borruel, J. Wykes, G. Erbert, I. Esquivias, P. Sewell, T.M. Benson, E.C. Larkins, J. Arias, B. Romero, H. Wenzel and B. Sumpf, "Quasi-3D optoelectronic modelling of 730nm Tapered Laser Diodes", CLEO Technical Digest, pp. 598-599, 2002.

[5.12] S. Adachi, and K. Oe, "Chemical etching characteristics of (001) GaAs", Journal of the Electrochemical Society, vol. 130(12), pp. 2427-2435, 1983.

[5.13] J. Schmidtchen, A. Splett, B. Schüppert, and K. Petermann, "Low loss single mode optical waveguides with large cross-section in silicon-on-insulator", Electronics Letters, vol. 27(16), pp. 1486-1488, 1991.

[5.14] T. Zinke, U. Fischer, A. Splett, B. Schüppert, and K. Petermann, "Comparison of optical waveguide losses in silicon-on-insulator", Electronics Letters, vol. 29(23), pp. 2031-2032, 1993.

[5.15] J. Lee, H. Cho, D. C. Hays, C. R. Cammy, R. Abernathy, S. J. Pearton, R. J. Shul, and G. A. Vawter, "Dry etching of GaN and related materials: Comparison of Techniques", IEEE Journal of Selected Topics in Quantum Electronics, vol. 4(3), 1998.

[5.16] M. Aoki, M. Komori, T. Tsuchiya, H. Sato, K. Nakahara, and K. Uomi, "InP-based reversed-mesa ridge-waveguide structure for high-performance long-

wavelength laser diodes", IEEE Journal of Selected Topics in Quantum Electronics, vol. 3(2), pp. 672-683, 1997.

[5.17]  P. Vandenbulcke, and P. E. Lagasse, "Eigenmode analysis of anisotropic optical fibres or integrated optical waveguides", Electronics Letters, vol. 12, pp. 120-122, 1976.

[5.18]  P. M. Pelosi, P. Vandenbulcke, C. D. W. Wilkinson, and R. M. De La Rue, "Propagation characteristics of trapezoidal cross-section ridge optical waveguides: an experimental and theoretical investigation", Applied Optics, vol. 17, pp. 1187-1193, 1978.

[5.19]  J. G. Gallagher, "Mode dispersion of trapezoidal cross-section rib waveguides by the effective-index method", Electronics Letters, vol. 15(23), pp. 734-736, 1979.

[5.20]  M. Koshiba, M. Suzuki, "Vectorial wave analysis of dielectric waveguides for optical-integrated circuits using equivalent network approach", IEEE Journal Lightwave Technology, vol. 4(6), pp. 656-664, 1986.

[5.21]  N. Dagli, and C. G. Fonstad, "Microwave equivalent circuit representation of rectangular dielectric waveguides", Applied Physics Letters, vol. 49(6), pp. 308-310, 1986.

[5.22]  N. Dagli, and C. G. Fonstad, "Analysis of rib dielectric waveguides", IEEE Journal of Quantum Electronics, vol. 21(4), 1990.

[5.23]  N. Dagli, "Equivalent circuit representation of open guided-wave structures", IEEE Journal of Quantum Electronics, vol. 26(1), 1990.

# Chapter 6   The SI Method: Modelling the Slab Loss Mechanism

The standard SI method as described in  [6.1] can be directly applied to the analysis of the complex propagation characteristics of optical rib waveguides, taking into account loss or gain. Rib waveguides that support leaky modes have been successfully analysed using the SI method, albeit in its discrete form, in [6.2]-[6.3]. In this chapter a discussion of application of the SI this method to the analysis of slab leakage waveguide losses is presented. The approach allows for the direct analysis and design of rib waveguides taking into account both substrate and, for the first time in the context of the SI method, slab loss mechanisms, where present, that previously required more numerically intensive approaches.

## 6.1   Introduction

The rib waveguide, is found in almost all semiconductor based integrated optical devices where it, in its most basic form, acts as a simple signal carrier. For low loss applications single mode rib waveguides are required and, for practical reasons, it is preferable that these waveguides have a relatively large cross section for ease of coupling to say, single mode fibres, [6.8]. Careful design allows the use of low loss mono-modal propagation in the oversized rib waveguides, whilst utilising loss mechanisms    to    rapidly    attenuate    the    higher    order    modes,    [6.3]-[6.8].

117

Several techniques are commonly used for the analysis of the propagation characteristics of rib waveguides that were discussed in chapter 2, but to summarise; numerical approaches, such as finite difference techniques, allow for the accurate and complete analysis of all the propagation regimes but are computationally intensive, semi-analytical techniques such have been successfully used, but are restricted in their range of application. The SI Method is one of the semi-analytical approaches that has, in its discrete form, previously been applied to the design of single mode rib waveguide incorporating substrate leakage in the realisation of mono-mode low loss rib waveguides, [6.3], but this work neglected the leakage due to slab modes. The inclusion of the slab mode leakage mechanism has received coverage in the microwave literature, [6.4]-[6.7], but has received little theoretical attention in the field of optical waveguides, yet it is necessary for the accurate prediction of waveguide losses and is discussed in the remainder of this chapter.

## 6.2   Theoretical Background

Consider the transcendental equation, (§3.6), for the fundamental quasi-TE mode

$$\gamma_1 \cot \gamma_1 = \frac{2}{\pi} \frac{s_1^2}{W} \int_{-\infty}^{+\infty} \Gamma \frac{\cos^2(sW)}{\left(s_1^2 - s^2\right)^2} ds \qquad (6.1)$$

The integrand of (6.1) is generally smooth and of the form depicted in  figure 6-1. If the waveguide possess a slab mode, in this case accomplished by increasing the depth D to 1.0μm, Γ (effectively the substrate response function) becomes singular
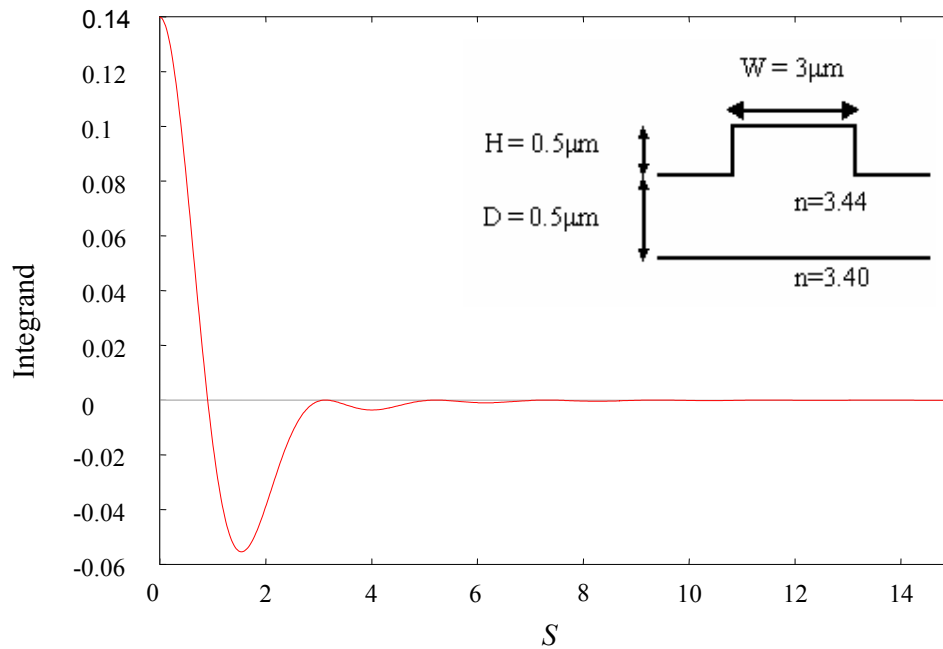
**Figure 6-1** The integrand of equation (6.1). The outer slab regions do not support a guided mode and hence the integrand is smooth.

for values of $\beta$ corresponding to the surface modes of the outer slab regions, $\beta_{slab}$.

Figure 6-2 illustrates the nature of the integrand when the outer slab regions support a mode. The integrand becomes singular in at a values of $s$ that correspond to the quasi- TE modes supported by the outer slab regions. The slab modes introduce a loss mechanism into an otherwise lossless system, for the case illustrated in figure 6-2 or contribute to other losses present in the system, such as substrate leakage.

Figure 6-3(a) illustrates the pole locations in the $S$-plane for lossless guided modes, i.e. real $k$ and real $\beta$, located on the top sheet of the Riemann surface. The integral in (6.1) is then simply evaluated along the real axis. For the situation where the system
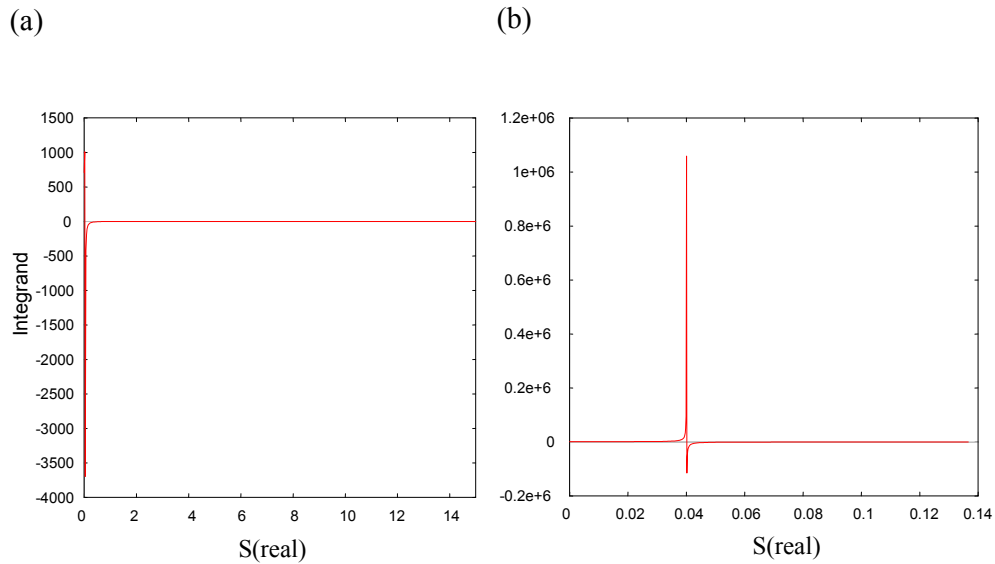
(a)                                                          (b)



**Figure 6-2** The integrand of equation 1, when the outer slab regions of the rib waveguide support a guided mode, $D = 1.0\mu m$. (a) shown over full range of integration, (b) restricted range.

is lossy, these poles migrate across the real axis. Figure 6-3(b) illustrates this situation on the $2^{nd}$ sheet of the Riemann surface. The contour of integration must remain on the same side of the poles and not cross them to ensure that the integrand remains continuous and hence the integration can no longer be carried out purely along the real axis. The solution is therefore to deform the path of integration as depicted in figure 6-3 (c).

In order to accurately evaluate analyse the loss contribution due to the slab modes of the rib waveguide the exact nature of the leaky poles have to be found and the calculation of the residue performed in order to evaluate the integral in equation (6.1) correctly, which will allow for the accurate determination of the complex propagation constants of the structure. We proceed by identifying the slab mode
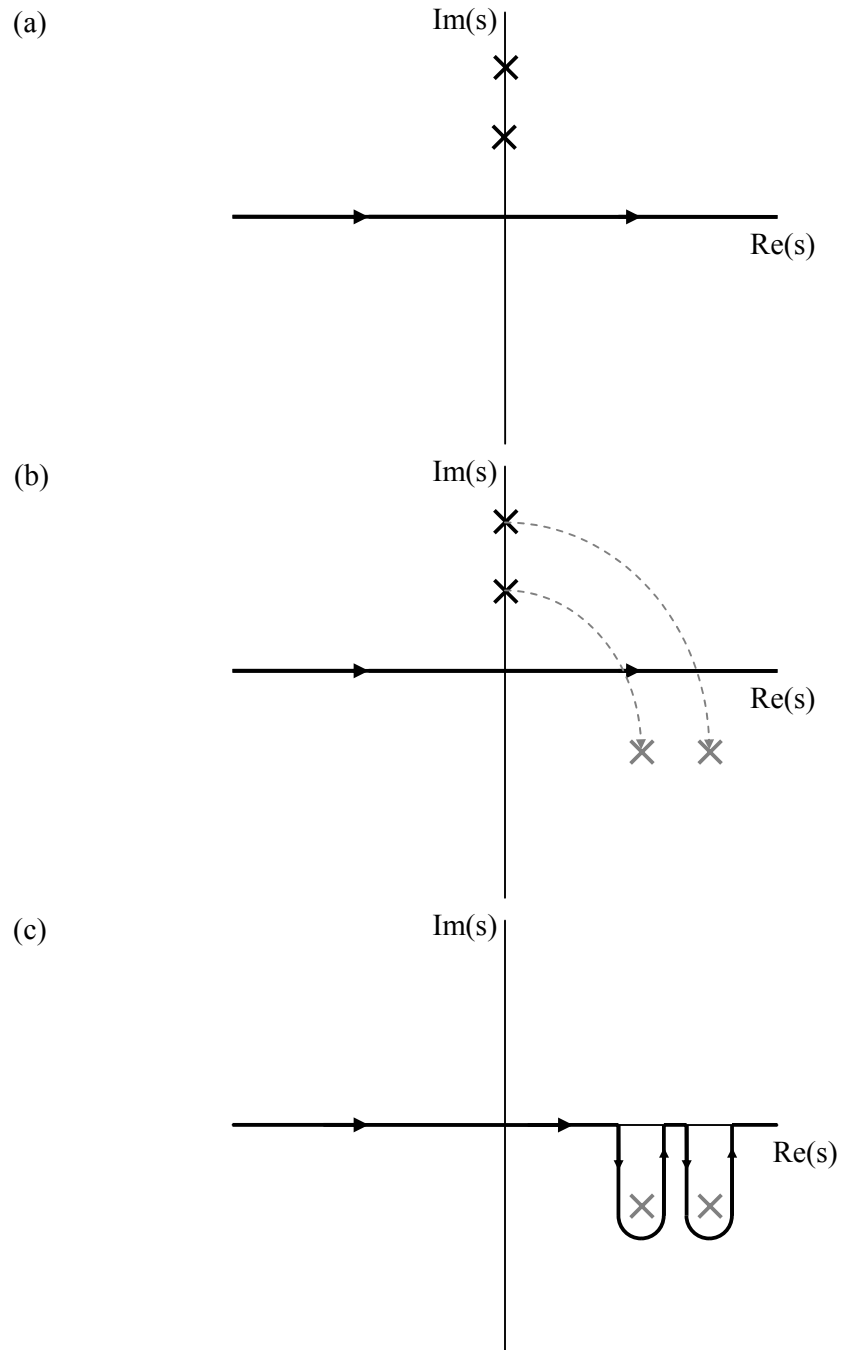
**Figure 6-3** Complex s-plane and the integration contour; (a) purely guided modes, (b) migration of poles across real axis as sytem becomes lossy, and (c)  leaky modes.

propagation constants so that the position of the poles in the *S*-plane may be identified via the relationship

$$s_{pole}^2 = \beta_{slab}^2 k_0^2 - \beta_{rib}^2 k_0^2 \tag{6.2}$$

where $\beta_{rib}$ is the propagation constant of a guided rib mode, $\beta_{slab}$ is the propagation constant of a guided slab mode and $k_0$ is the wave number $2\pi/\lambda$ .The guided modes of the outer slab waveguides, as they are lossless, will possess purely real propagation constants, $\beta_{slab}$ and so the pole will initially lie on the real axis. But as the solution of (6.1) is an iterative process the value of $s_{pole}$ will in general be complex.

Once the position of the poles in the *S*-plane has been identified the domain of integration is divided up in order to isolate the singular parts of the integrand. For the simplified case of a single slab mode i.e. a single pole at $s = \alpha$, the integral in equation (6.1) may be re-written as

$$\int_0^\infty f(s)ds = \int_0^{\alpha-d} f(s)ds + \int_{\alpha-d}^{\alpha+d} f(s)ds + \int_{\alpha+d}^\infty f(s)ds \tag{6.3}$$

where

$$f(s) = \Gamma \frac{\cos^2(sW)}{\left(s_1^2 - s^2\right)^2} \tag{6.4}$$

The integral over the first and third sub-domains remains smooth and is evaluated numerically in the normal manner. However, the integral in the second sub-domain contains the singularity and requires careful evaluation. Here we evaluate the integral by extracting the singularity at $s = \alpha$. The integral in the second sub-domain may be written as

$$\int_{\alpha-d}^{\alpha+d} f(s)ds = \int_{\alpha-d}^{\alpha+d} f(s) - \frac{A}{s-\alpha} + \int_{\alpha-d}^{\alpha+d} \frac{A}{s-\alpha} \tag{6.5}$$

Due to symmetry

$$\int_{\alpha-d}^{\alpha+d} \frac{A}{s-\alpha} = 0 \tag{6.6}$$

and thus

$$\int_{\alpha-d}^{\alpha+d} f(s)ds = \int_{\alpha-d}^{\alpha+d} f(s) - \frac{A}{s-\alpha} \tag{6.7}$$

where $A$ is the residue of $f(s)$ evaluated at $s = \alpha$ and is given by

$$A = \operatorname*{Res}_{s=\alpha} f(s) = \frac{p(s)}{q'(s)} \tag{6.8}$$

where $p(s) = \Gamma_{numerator} \cos^2(sW)$, $q(s) = \Gamma_{denominator} \left(s_1^2 - s^2\right)^2$ and $s_1 = \pi/2W$.

## 6.3   Numerical Results

The method presented above was applied to the rib waveguide that is schematically depicted in figure 6-4. The waveguide is based upon a Silicon on Insulator (SOI) device, [6.9], such that; $n_{guide} = 3.5$ and $n_{substrate} = 1.45$ at $\lambda=1.546\mu m$, $h=1.7\mu m$, $d=3.3\mu m$ and $w=4.0\mu m$. Such waveguides are designed to be mono-modal, relying on leakage mechanisms to suppress the higher order modes. The waveguides presented in [6.10] relied upon the slab leakage mechanism to attenuate higher order vertical modes that possessed effective indices (neff) lower than that of the fundamental slab mode. Thus, for mono-modal operation it is required that all rib modes other than the fundamental have an neff lower than the neff of the fundamental slab mode. The first five TE modes of the rib (calculated by the standard SI method) and outer slab regions of the waveguide depicted in figure 5 are given in Table 6-1.
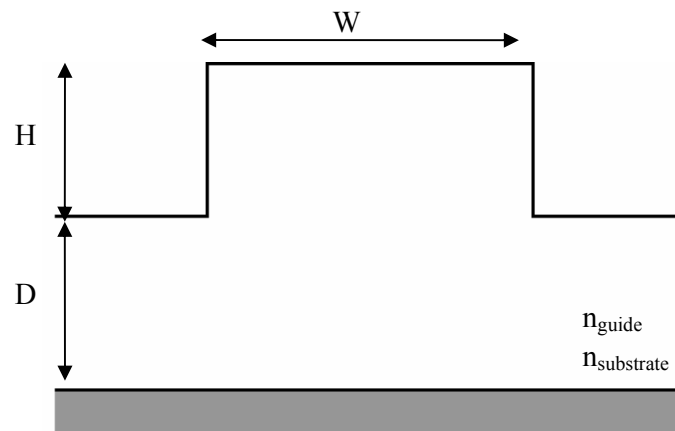


**Figure 6-4** Transverse cross section of a SOI air clad rib waveguide.

| Rib Waveguide | | Outer Slab Waveguide | |
|---|---|---|---|
| $TE_{0,0}$ | 3.4951127 | $TE_0$ | 3.4927883 |
| $TE_{1,0}$ | 3.4842093 | $TE_1$ | 3.4710696 |
| $TE_{2,0}$ | 3.4672937 | $TE_2$ | 3.4345872 |
| $TE_{3,0}$ | 3.445187 | $TE_3$ | 3.382897 |

**Table 6-1** Effective indices of the first four TE modes of an SOI rib waveguide and its associated slab modes, for the rib waveguide of figure 6-4; $n_{guide\ =}$ 3.5 and $n_{substrate=}$ 1.45 at $\lambda$=1.546μm, h=1.7μm, d=3.3μm and w=4.0μm.

As is seen from table 6-1 all the TE rib modes, except the fundamental have neff's lower than that of the fundamental slab mode. However no information on the losses attributable to the slab leakage mechanism is provide. The SI approach as previously described in this chapter was used to analyse the same waveguide and the results for the first four modes are given below in table 6-2.

| Rib Waveguide | | Loss dB/cm |
|---|---|---|
| $TE_{0,0}$ | 3.4942 | 0.0 |
| $TE_{1,0}$ | 3.4854 | 0.1339 |
| $TE_{2,0}$ | 3.4686 | 0.4254 |
| $TE_{3,0}$ | 3.4452 | 0.9308 |

**Table 6-2** Predicted effective indices of the first four TE modes computed by the SI method modified to account for the slab leakage mechanism. The rib waveguide is as figure 6-4 with; $n_{guide\ =}$ 3.5 and $n_{substrate=}$ 1.45 at $\lambda$=1.546μm, h=1.7μm, d=3.3μm and w=4.0μm.

As table 6-2 shows, the SI method predicts that the fundamental mode is, as expected lossless. The losses of the higher order modes are seen to increase, again as expected, as higher order slab modes begin to contribute to the overall loss of the rib modes.

## 6.4   Conclusions

A numerical analysis of rib waveguide losses using the Spectral Index method has been presented. It has been shown that careful consideration of the nature of the integrand in the SI formulation is essential for the accurate prediction of waveguide losses attributable to the surface waves of the outer slab regions of a rib waveguide. This is particularly significant when oversized guides are used, relying on such losses to effectively provide mono-modal behaviour. Furthermore, accurate prediction of this loss mechanism is important for avoiding cross-talk, especially in the case of densely integrated optoelectronic circuits.

## 6.5   References

[6.1]   S. V. Burke, "Planar waveguide analysis by the spectral index method: II. Multiple layers, optical gain and loss", Optical and Quantum Electronics, vol. 26, pp. 63-77, 1994.

[6.2]   G. M. Berry, S. V. Burke, and J. M. Heaton, "Analysis of multilayered semiconductor leaky rib waveguides", Computation in Electromagnetics, Second International Conference on, pp. 32-35, 1994.

[6.3]   J. M. Heaton, M. M. Bourke, S. B. Jones, B. H. Smith, K. P. Hilton, G. W. Smith, J. C. Birbeck, G. Berry, S. V. Dewar, and D. R. Wright, "Optimization of depp etched, single-mode GaAs/AlGaAs optical waveguides using controlled leakage into the substrate", IEEE Journal of Lightwave Technology, vol. 17(2), pp. 267-281, 1999.

[6.4]   T. Rozzi, F. Moglie, A. Morini, E. Marchionna, and M. Politi, "Hybrid modes, substrate leakage and losses of slotline at millimetre-wave frequencies", IEEE Transactions on Microwave Theory and Techniques, vol. 38(8), pp. 1069-1078, pp. 941-943, 1990.

[6.5]   J. M. Grimm, and D. P. Nyquist, "Spectral analysis considerations relevant to radiation and leaky modes of open-boundary microstrip transmission lines", IEEE Transactions on Microwave Theory and Techniques, vol. 41(1), pp. 150-153, 1993.

[6.6]   J. S. Bagby, C, -H Lee, D. P. Nyquist, and Y. Yuan, "Identification of propagation regimes on integrated microstrip transmission lines",  IEEE Transactions on Microwave Theory and Techniques, vol. 41(11), pp.1887-1894, 1993.

[6.7]    L. O. Mc. Millan, N. V. Shuley, and P. W. Davis, "Leaky fields on microstrip", Progress in Electromagnetic Research, PIER, 17, pp. 323-337, 1997.

[6.8]    P. Souren, L. V. Pogossian, and A. Vonsovici, "The single mode Condition for Semiconductor Rib Waveguides with Large Cross Section", IEEE Journal of Lightwave Tech., vol. 16(10), pp. 1851-1853, 1998.

[6.9]    A. G. Rickman, G. T. Reed, and F. Namavar, "Silicon-on-insulator optical rib waveguide loss and mode characteristics", IEEE Journal of Lightwave Technology, vol. 12(10), pp. 1771-1776, 1994.

[6.10]  R. A. Soref, J. Schmidtchen, K. Petermann, "Large   Single Mode Rib Waveguides in GeSi-Si and Si-on-SiO$_2$", IEEE Journal of  Quantum Electronics, vol. 27(8), pp.1971-1974, 1991.

# Chapter 7  Spectral Index Analysis of Dielectric Resonators

## 7.1  Introduction

In this chapter the spectral index approach is used in the development of a novel method for the analysis of the modes supported by resonant dielectric structures of circular geometry. The structures of interest are illustrated in figure 7-1 below.



**Figure 7-1** Schematci illustration of dielectric structures of circular geometry; (a) disc and (b) ring.

Such structures are of particular interest as they yield high $Q$ factors for a relatively small device and may be realised with dimensions comparative to the wavelength of operation, [7.1]-[7.3]. One implementation of circular resonators that has received much attention involves their use to provide a frequency dependant coupling mechanism between parallel rib waveguides, [7.4]-[7.9]. Figure 7-2 illustrates such a device in the form of a channel dropping filter. Light, at a resonance of the ring, is evanescently coupled from the input guide to the ring resulting in a resonant

field that further couples, drops, to the output guide. Complete power transfer from the input guide to the output can be obtained using such a device. Such structure are typified by large core/cladding refractive index contrasts that allow for a small radius of curvature ensuring a low bending loss and as such are generally air clad devices or clad with low index oxides, see for example [7.6].
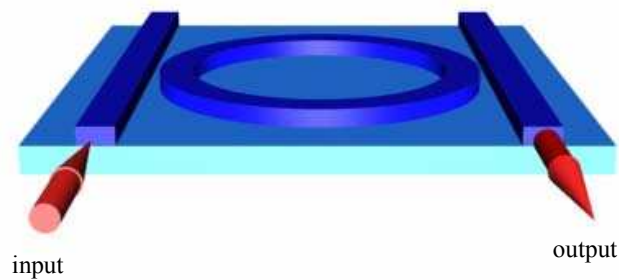


**Figure 7-2** Illustration of a channel dropping filter**.**

A variety of methods exist with which to study the natural frequencies and scattering characteristics of dielectric disk resonators (DRs), and broadly fall into one of the three classes; analytical, semi-analytical or numerical. Among them are radial and axial mode-matching methods [7.10]-[7.11], effective dielectric constant method (EDC) [7.12]-[7.13], finite-element method (FEM) [7.14], frequency and time domain finite difference methods [7.15]-[7.16], surface and volume integral equation techniques [7.17]-[7.18]. Though being of some interest for remote sensing and antenna applications, knowledge of the resonant frequencies of isolated DRs is of little importance for practical optical applications. Optical DRs are commonly building blocks of complex structures, which include mechanisms for tuning and coupling to guiding or supporting surfaces. The resonant frequencies of a loaded DR

may differ significantly from those of the isolated DR making the standard perturbation techniques inapplicable in this case. Therefore, for accurate calculations of the microwave and optical properties of practical structures efficient and versatile approaches are needed.

In [7.19] an equivalent circuits approach was applied to study the characteristics of DRs coupled to transmission lines or to each other. Although simple, this method does not directly give the resonant frequencies and its application is limited to coupled modes with constant or linear coupling coefficients. Some attempts have been made to study the complex frequencies of DRs in a shielded microwave integrated circuit (MIC) environment and to estimate the degradation of the Q-factors due to conductor loss. For example, a perturbation method was proposed in [7.20] for the indirect determination of the conductor Q-factors of DRs by computing the relative difference between perturbed and unperturbed resonant frequencies, however, these were required to be evaluated beforehand by using more rigorous methods. Resonant frequencies and field patterns for DRs located on a microstrip substrate or in a cavity have also been studied by the EDC method, [7.12]-[7.13], and the generalized impedance boundary conditions method (GIBC), [7.21]. Furthermore, the mode matching technique was widely applied to the investigation of DRs in a MIC environment [7.22].

For integrated optics applications, it is necessary to study the characteristics of DRs in a non-shielded layered environment. In this case the analysis becomes even more complicated since it requires consideration of the conditions at infinity. Surface integral equations techniques (IEs) were applied in [7.23] to study the resonant

frequencies of a dielectric disc on a dielectric substrate. In [7.24] the problem of optimizing the matching between the transmission lines and whispering gallery-mode DRs was considered by using an approximate method based on the interpretation of the DR modes as a superposition of plane waves. A combination of the volume IE method and Galerkin technique was used to analyze DRs in an inhomogeneous environment, [7.25], for resonators with separable geometries.

Although, as mentioned above, a number of accurate numerical methods exist, the computational requirements of these methods are high for studying the optical properties of dielectric resonators. The remainder of this chapter describes a semi-analytical approach based on the SI method for the analysis of  a class of modes supported by circular dielectric resonators namely, the whispering gallery modes.

## 7.2   Definition and classification of whispering gallery modes

The resonances of interest in this work are those that fall into the category of whispering gallery modes (WGMs). Acoustic WGMs were first described by Lord Rayleigh, [7.26], when it was observed that high frequency sound waves tend to remain bound to concave surfaces. Likewise, the optical modes supported by dielectric resonators exhibit the same behaviour whereby, due to the mechanism of total internal reflection, the majority of the modal energy remains confined between boundaries defined by the concave circular wall of the resonator, $r_2$, and an inner modal caustic, $r_1$. Figure 7-3 (a) illustrates this from a ray optics view, while in figure 7-3(b) the field distribution of a WGM is shown schematically. In general, the guided WGMs of dielectric resonators are hybrid, and thus, the full vectorial

eigenvalue problem must be solved. However, as an initial approximation, it is often sufficient to regard them as either $WGE^{\pm}_{m,n,l}$ (electric field being essentially transverse $E_y = 0$ ) or $WGH^{\pm}_{m,n,l}$ (electric field being essentially axial, $H_y = 0$ ). Such an approximation simplifies the wave equations for the electric and magnetic fields so that only a single scalar Helmholtz equation for either radial electric or radial magnetic field component need be solved, [7.1]. The subscripts *n,m,l* denote the number of radial, azimuthal and axial field variations, respectively. The superscripts $\pm$ denote the two possible rotating senses of the mode but, due to the axial symmetry the modal solutions are doubly degenerate and so there is no discrimination between the natural frequencies of each sense of rotation and so no further distinction is made between these two cases.
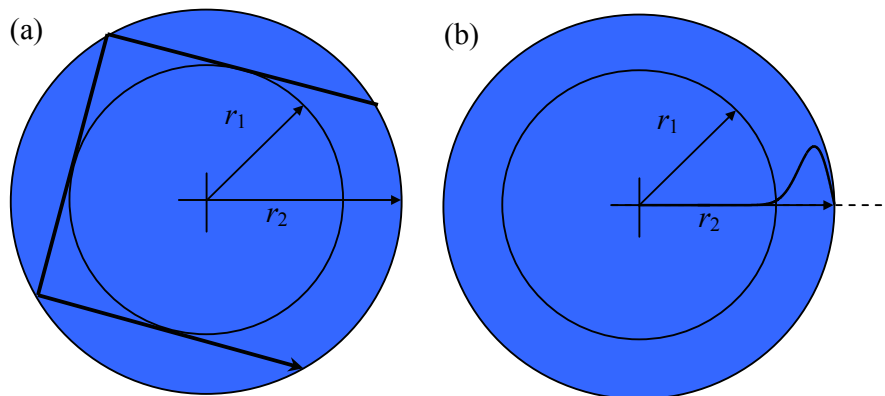


**Figure 7-3** (a) WGM ray diagram, (b) typical WGM field pattern.

It is known that WGMs are leaky, [7.27], thus the natural frequencies of the structure will be complex in nature, $\omega = \omega_{real} + j\omega_{imag}$, where $\omega_{real}$ is the resonant frequency of the mode and $\omega_{imag}$ is a decay constant of the mode.
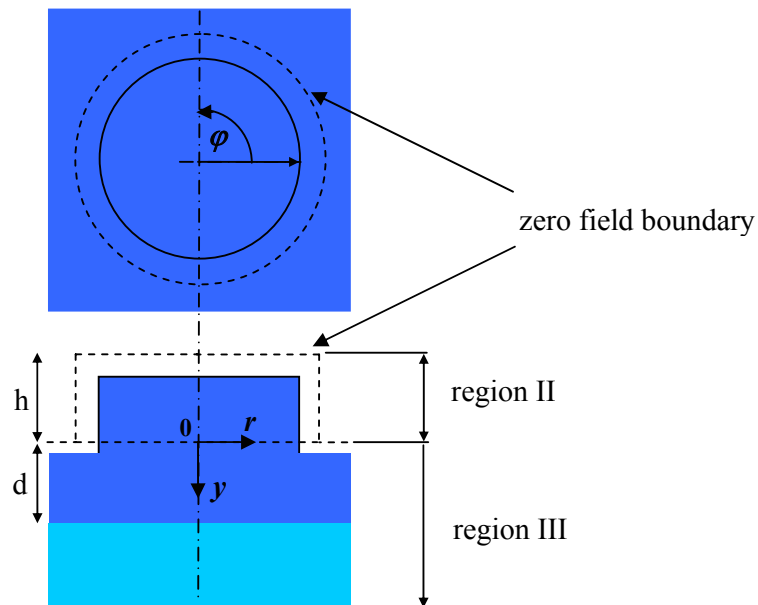


**Figure 7-4** Cross-section of a resonator structure illustrating use of effective boundaries.

## 7.3 Theory

With reference to figure 7-4 the method proceeds in a manner similar to that detailed in chapter 3, that describes the SIM applied to the analysis of rectangular rib waveguides. Firstly the true boundaries of the structure are displaced by an amount determined from physically consistent arguments. On these displaced boundaries the field is set to zero yielding an equivalent problem that is significantly easier to solve. The problem space is then divided into 3 regions; (i) the air cladding, (ii) the disc

and (iii) the multi-layered substrate. The field in each region of the equivalent structure is then expressed as a superposition of local solutions of the wave equation. The solutions are then matched with a variational expression to yield a transcendental equation for the natural frequencies of the structure.

### 7.3.1 Solution of the wave equation

Chapter 2 introduced the vector wave equation in cylindrical coordinates (§2.4), which expanded into its component parts is given by

$$
\begin{aligned}
\hat{r}\left[\nabla^2 E_r - \frac{2}{r^2}\frac{\partial E_\phi}{\partial \phi} - \frac{E_r}{r^2} - \frac{\partial}{\partial r}\left(\frac{1}{r}\frac{\partial (rE_r)}{\partial r} + \frac{1}{r}\frac{\partial E_\phi}{\partial \phi} + \frac{\partial E_y}{\partial y}\right) + k^2 E_r\right] & \\
\hat{\phi}\left[\nabla^2 E_\phi + \frac{2}{r^2}\frac{\partial E_r}{\partial \phi} - \frac{E_\phi}{r^2} - \frac{1}{r}\frac{\partial}{\partial \phi}\left(\frac{1}{r}\frac{\partial (rE_r)}{\partial r} + \frac{1}{r}\frac{\partial E_\phi}{\partial \phi} + \frac{\partial E_y}{\partial y}\right) + k^2 E_\phi\right] & = 0 \\
\hat{y}\left[\nabla^2 E_y - \frac{\partial}{\partial y}\left(\frac{1}{r}\frac{\partial (rE_r)}{\partial r} + \frac{1}{r}\frac{\partial E_\phi}{\partial \phi} + \frac{\partial E_y}{\partial y}\right) + k^2 E_y\right] &
\end{aligned}
\quad (7.1)
$$

As discussed earlier WGMs are essentially polarised and so we assume either; $E_y = 0$ for WGE modes or $H_y = 0$ for WGH modes. Equation (7.1) therefore polarises under these assumptions and, in each homogenous region, may be simplified to

$$
\frac{1}{r}\frac{\partial}{\partial r}\left(r\frac{\partial \psi}{\partial r}\right) + \frac{1}{r^2}\frac{\partial^2 \psi}{\partial \theta^2} + \frac{\partial^2 \psi}{\partial y^2} + k^2\psi = 0
\tag{7.2}
$$

where $\psi$ is to be understood to represent $rE(r)$ for WGE modes and $E(y)$ for

WGM modes respectively. A process of separation of variables yield solutions of the

form

$$\psi = R(r)\Phi(\theta)Y(y) \tag{7.3}$$

Substituting (7.3) in (7.2)

$$\frac{\Phi Y}{r}\frac{d}{dr}\left(r\frac{dR}{dr}\right) + \frac{RY}{r^2}\frac{d^2\Phi}{d\theta^2} + R\Phi\frac{d^2Y}{dy^2} + k^2\psi = 0 \tag{7.4}$$

Dividing equation (7.4) by (7.3) and separating $k^2$ into its component parts gives

$$\frac{1}{Rr}\frac{d}{dr}\left(r\frac{dR}{dr}\right) + \frac{1}{\Phi r^2}\frac{d^2\Phi}{d\theta^2} + \frac{1}{Y}\frac{d^2Y}{dy^2} + \left(k_r^2 + k_y^2\right) = 0 \tag{7.5}$$

Considering only the $y$ dependence only

$$\frac{1}{Y}\frac{d^2Y}{dy^2} = -k_y^2 \tag{7.6}$$

Substituting (7.6) into (7.5) yields

$$\frac{1}{Rr}\frac{d}{dr}\left(r\frac{dR}{dr}\right) + \frac{1}{\Phi r^2}\frac{d^2\Phi}{d\theta^2} + k_r^2 = 0 \tag{7.7}$$

Rearranging and multiplying (7.7) by $r^2$

$$\frac{r}{R}\frac{d}{dr}\left(r\frac{dR}{dr}\right)+k_r^2 r^2 = -\frac{1}{\Phi}\frac{d^2\Phi}{d\theta^2} \tag{7.8}$$

For the process of the separation of variables to be valid then the left hand side of (7.8) (a function of $r$ only) must be equal to the right hand side (a function of $\theta$ only) for all values of $r$ and $\theta$. Thus both sides must be equal to a constant, denoted as $v^2$. Equation (7.8) can therefore be written as two differential equations

$$\frac{r}{R}\frac{d}{dr}\left(r\frac{dR}{dr}\right)+k_r^2 r^2 = v^2 \tag{7.9}$$

and

$$\frac{1}{\Phi}\frac{d^2\Phi}{d\theta^2} = -v^2 \tag{7.10}$$

Rewriting (7.9) gives

$$\frac{d^2 R}{dr^2}+\frac{1}{r}\frac{dR}{dr}+\left(k_r^2-\frac{v^2}{r^2}\right)R = 0 \tag{7.11}$$

which describes the radial dependence of the optical field. Equation (7.11) is the general Bessel equation with solutions $J_v(k_r r)$, $N_v(k_r r)$, $H_v^{(1)}(k_r r)$ and $H_v^{(2)}(k_r r)$; where $J_v$ and $N_v$ are Bessel functions of the first and second kind respectively and $H_v^{(1)}$ and $H_v^{(2)}$ are Hankel functions of the first and second kind respectively. The

constant $v$ denotes the order of the equation which, in general, may be real, imaginary or complex. The solutions to equation (7.11) can be written as

$$R = AJ_v\left(k_r r\right) + BN_v\left(k_r r\right) \tag{7.12}$$

or

$$R = CH_v^{(1)}\left(k_r r\right) + DH_v^{(2)}\left(k_r r\right) \tag{7.13}$$

Equations (7.6) and (7.10) have solutions of the form

$$Y = e^{-j\gamma y} \tag{7.14}$$

and

$$\Phi = e^{-jv\theta} \tag{7.15}$$

respectively. Thus from equations (7.3) and equations (7.12)-(7.15) the complete solutions of the scalar wave equation in cylindrical coordinates are

$$\psi = \left(AJ_v\left(k_r r\right) + BN_v\left(k_r r\right)\right)e^{-jv\theta}e^{-j\gamma y} \tag{7.16}$$

or

$$\psi = \left(CH_v^{(1)}\left(k_r r\right) + DH_v^{(2)}\left(k_r r\right)\right)e^{-jv\theta}e^{-j\gamma y} \tag{7.17}$$

Considering the dielectric resonator structures we require a solution that is circularly coherent, i.e. $\Phi(0) = \Phi(2\pi) = \Phi(4\pi).... = \Phi(2n\pi)$ where n = (1, 2, 3, 4…). Hence $v$ is required to be a positive real integer, $n$, for the case of WGMs.

Further, for WGMs it is required that the radial field within the disc is oscillatory in nature and that the field outside of the resonator decays rapidly with radial distance. Thus it is obvious from the functional behaviour of the Bessel and Hankel functions that the field within the disc must be of the form given by (7.16) and outside of the disc solutions must be of the form given by (7.17).

## 7.3.2  Determination of the Effective Structure

As previously discussed the SIM relies heavily on the fact that the field outside of the guiding structure decays very rapidly away from the physical boundary of the guide. The resonant modes of the dielectric disc structures are, by their very nature, tightly confined to the guide with very little penetration of the optical field into the air cladding. Thus the use of effective penetration depths, as discussed in chapter 3 is justified.

Within the structure the radial field dependence is represented solely in terms of the oscillatory Bessel functions and outside of the boundary of the disc by Hankel functions (as a rapidly decaying field is assumed), equations (7.12) and (7.13). It is now required that the small field penetration beyond the boundary of the resonator is suitably taken into account for by displacing the physical boundary a distance $\Delta_r$, at which point the optical field is set to zero. To accomplish this, the amplitude and gradient of the Bessel and Hankel functions are matched at the physical boundary while the Bessel function is chosen such that it is zero at the effective boundary.
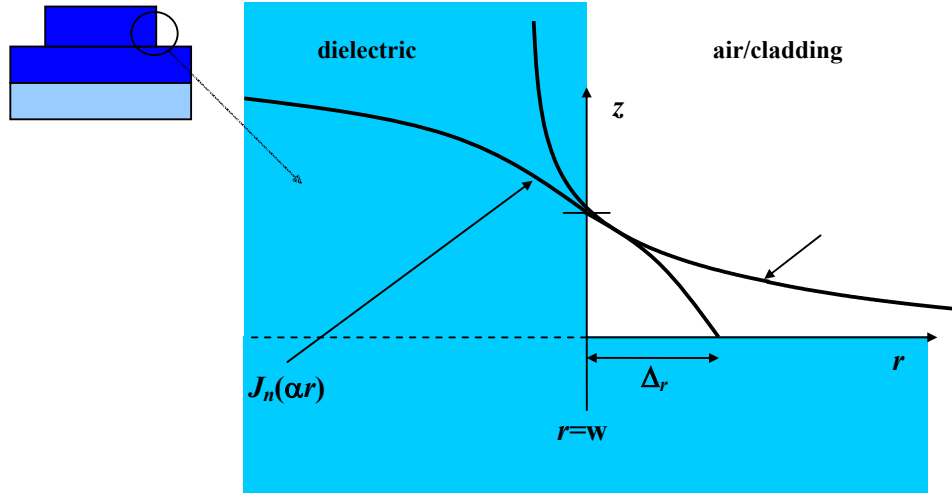
**Figure 7-5** Determination of effective penetration depths.

Figure 7-5 illustrates the WGH case where the principal field component is tangential to the dielectric interface, the vertical curved wall. The normalised field amplitudes are matched at the dielectric/air boundary ($r = w$) such that

$$\frac{J_n(\alpha r)}{J_n(\alpha w)} = \frac{H_n^{(2)}(\beta r)}{H_n^{(2)}(\beta w)} \tag{7.18}$$

In (7.18), $\alpha$ and $\beta$ are understood to represent the radial wavenumbers inside and outside of the dielectric disc respectively. Subsequently matching the normalised field gradients at this point gives

$$\alpha \frac{J_n'(\alpha w)}{J_n(\alpha w)} = \beta \frac{H_n^{(2)\prime}(\beta w)}{H_n^{(2)}(\beta w)} \tag{7.19}$$

In (7.18) it is required that $J_n(\alpha r) = 0$ for $r = w + \Delta r_t$, applying this condition to (7.19) gives

$$\alpha \frac{J_n'(\alpha(w + \Delta r_t))}{J_n(\alpha w)} - \beta \frac{H_n^{(2)'}(\beta(w + \Delta r_t))}{H_n^{(2)}(\beta w)} = 0 \tag{7.20}$$

Equation (7.20) can now be solved for the effective penetration depth, $\Delta r_t$, where the subscript $t$ is used to denote the penetration depth due to the field component that is tangential to the interface. For the WGE case, principal field component normal to the interface, the discontinuity of the dielectric leads to a jump in the optical field relative to the change in refractive index. Following a similar process gives

$$\frac{\alpha}{n_{disc}^2} \frac{J_n'(\alpha(w + \Delta r_n))}{J_n(\alpha w)} - \beta \frac{H_n^{(2)'}(\beta(w + \Delta r_n))}{H_n^{(2)}(\beta w)} = 0 \tag{7.21}$$

where $n_{disc}$ is the refractive index of the dielectric disc. Equation (7.21) can then be solved for $\Delta r_n$. On the top surface of the disc the effective penetration depths remain the same as those for the standard rectangular rib case and are

$$\Delta_n = \frac{1}{n_g^2} \frac{1}{\sqrt{k_0^2 + \alpha^2}} \quad \text{and} \quad \Delta_t = \frac{1}{\sqrt{k_0^2 + \alpha^2}} \tag{7.22}$$

for the WGH and WGE modes respectively. These lead to an effective structure with dimensions

$$w = r + \Delta r_t, \quad H = h, \quad D = d + \Delta_n$$

for the WGH modes and

$$w = r + \Delta r_n, \quad H = h, \quad D = d + \Delta_t$$

for the WGE modes.

### 7.3.3 Formulation of the Transcendental Equation – Dielectric Disc

The problem of the dielectric disc, as illustrated in figure 7-6, can now be approached in the same manner as that of the standard rectangular rib discussed in chapter 3. The problem space is thus divided into 3 regions; (i) the air cladding, (ii) the disc ($y < 0$) and (iii) the substrate ($y > 0$).

In the air/cladding region the optical field is everywhere set to zero. In the disc, region (ii), solutions to equation (7.2) are sought that identify the resonant modes of the structure, the solutions being of the form indicated by equations (7.16) and (7.17)
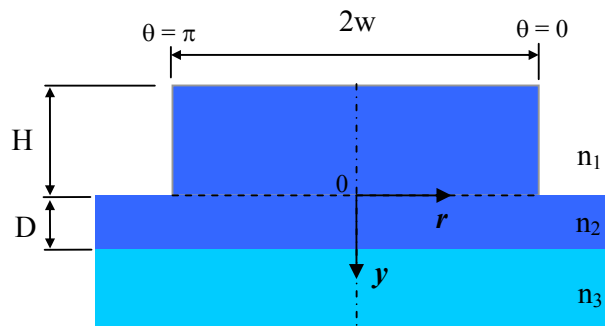


**Figure 7-6** Cross section of a dielectric resonator, where all dimension are understood to be that of the effective structure.

Considering the radial dependence of the optical field, $R$, given by equation (7.12) within the dielectric disc, Bessel functions of the second kind are singular at $r = 0$ and thus cannot form part of the solution. The radial dependence of the optical field within the dielectric disc is therefore reduced to

$$R(r) = J_n(k_r r) \tag{7.23}$$

In equation (7.23) $n$ deontes the order of the Bessel function (which is a real integer) and $k_r$ is chosen such that $R(r)$ is zero for $r = w$ in order to satisfy the requirement for the optical field to be zero at the boundary of the effective disc.

The azimuthal dependence is given by

$$\Phi(\theta) = e^{-jn\theta} \tag{7.24}$$

and the $y$ dependence being of the same form as that for the rectangular rib

$$Y(y) = \frac{\sin k_y (y + H)}{\sin(k_y H)} \tag{7.25}$$

which ensures a zero optical field across the top of the disc.

Below the disc, region (iii), the Hankel transform of $\psi$ is taken. In general, for a function $f(x)$ the transform pair is given by

$$g_v(s) \equiv H_v\{f(x)\} \equiv \int_0^\infty f(x) J_v(sx) x\, dx$$

$$\text{(7.26)}$$

$$g_v(s) \equiv H_v^{-1}\{g_v(s)\} \equiv \int_0^\infty g(s) J_v(sx) s\, ds$$

Therefore for the case in question the transform pair is given by

$$\psi(s) = \int_0^\infty \psi(r) J_n(sr) r\, dr$$

$$\text{(7.27)}$$

$$\psi(r) = \int_0^\infty \psi(s) J_n(sr) r\, ds$$

Using the variational boundary condition

$$\int_{-w}^{w} r\psi_r \left[ \frac{\partial \psi_r}{\partial y} \right]_-^+ dr = 0 \qquad \text{(7.28)}$$

to match the solutions in regions (ii) and (iii) either side of $y = 0$, yields the final transcendental equation for the WGMs

$$k_y \tan k_y H = \int_{-\infty}^{\infty} s|\psi(s)|^2 \Gamma(s)\, ds \qquad \text{(7.29)}$$

where

$$\psi(s) = \int_0^w r J_n(k_r r) J_n(sr) \, dr \qquad (7.30)$$

and $\Gamma(s)$ is given by the standard plane wave response function of the layered medium for $y > 0$

$$\Gamma(s) = \Gamma_2 \left[ \frac{\Gamma_2 \sin(\Gamma_2 D) - \Gamma_3 \cos(\Gamma_2 D)}{\Gamma_2 \cos(\Gamma_2 D) + \Gamma_3 \sin(\Gamma_2 D)} \right] \qquad (7.31)$$

where

$$\Gamma_2 = \left(k_2^2 - s^2\right)^{\frac{1}{2}} \quad , \quad \Gamma_3 = \left(k_3^2 - s^2\right)^{\frac{1}{2}} \qquad (7.32)$$

Equation (7.30) may be evaluated thus

$$\psi(s) = \left[ r \frac{\left(s J_n(k_r r) J_{n-1}(sr) + k_r J_{n-1}(k_r r) J_n(sr)\right)}{k_r^2 - s^2} \right]_0^w$$

$$\psi(s) = w \frac{\left(s J_n(k_r w) J_{n-1}(sw) + k_r J_{n-1}(k_r w) J_n(sw)\right)}{k_r^2 - s^2} \qquad (7.33)$$

The zero field condition requires that

$$J_n(k_r w) = 0 \qquad (7.34)$$

hence

$$\psi(s) = w \frac{\left(k_r J_{n-1}(k_r w) J_n(sw)\right)}{k_r^2 - s^2}$$

(7.35)

where $k_r$ is known from (7.34) and $k_y$ is given by

$$k_y = \sqrt{k^2 - k_r^2} \quad \text{and} \quad k = \frac{2\pi}{\lambda}$$

(7.36)

In (7.29) only the first zero of the Bessel function is used to represent the radial field distribution (this should be compared with the use of only the fundamental transverse term used in the standard SIM). Higher order zeros may be included in the same manner as the standard SIM in order to increase the accuracy of the method. The expression for the field across the base of the resonator, omitting the θ dependence for clarity, then becomes

$$\psi = \sum_{m=1}^{N} A_m J_n\left(k_r^m r\right) \frac{\sin k_y (y + H)}{\sin\left(k_y H\right)}$$

(7.37)

where $m$ is the number of terms and $A_m$ is the amplitude of the $m^{\text{th}}$ term. Equation (7.29) is therefore replaced by a matrix equation of the form

$$\left|\underline{\underline{M}}\right| = 0$$

(7.38)

where $\underline{\underline{\mathbf{M}}}$ is a square matrix of order m, whose elements $\mathbf{M}_{mm}$ are given by

$$k_{ym'} \tan k_{ym'} H = \int_{-\infty}^{\infty} s\psi(s)_m^* \psi(s)_{m'} \Gamma(s) \ ds \tag{7.39}$$

In (7.29) and (7.39) $k_y$ and $\Gamma(s)$ are functions of angular frequency, $\omega$, which is the only free variable. As stated earlier WGMs are complex in nature and so values of $\omega$ are sought in the complex frequency plane for which (7.29) and (7.39) are satisfied.

### 7.3.4  Formulation of the transcendental equation – dielectric ring

In the case of a dielectric ring, figure 7-7, the axis $r = 0$ is no longer part of the dielectric disc. Therefore the radial field dependence now includes the Bessel functions of the second kind that were previously omitted due to them being infinite at $r = 0$. The radial field dependence is thus given by

$$R = AJ_v(k_r r) + BN_v(k_r r) \tag{7.40}$$
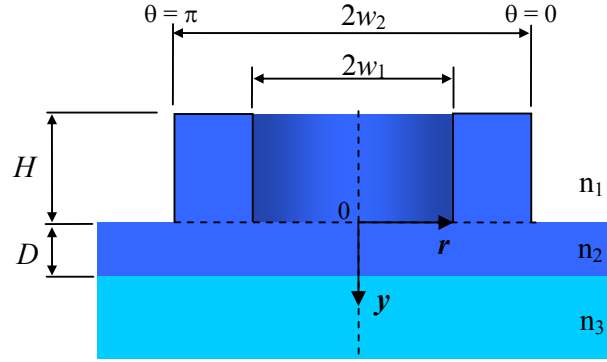
**Figure 7-7** Cross section of a dielectric ring resonator, where all dimension are understood to be that of the effective structure.

where

$$AJ_v\left(k_r r\right) + BN_v\left(k_r r\right) = 0 \quad \text{for} \ \ r = w_1 \ \ \text{and} \ \ r = w_2 \tag{7.41}$$

For $r = w_1$, rearranging (7.41) for $B$ and substituting in (7.40) gives

$$R = J_n\left(k_r r\right) - N_n\left(k_r r\right)\frac{J_n\left(k_r w_1\right)}{N_n\left(k_r w_1\right)} \tag{7.42}$$

which, for $r = w_1$, ensures that the zero field boundary condition, $R = 0$, is satisfied.

For $r = w_2$

$$R = J_n\left(k_r w_2\right) - N_n\left(k_r w_2\right)\frac{J_n\left(k_r w_1\right)}{N_n\left(k_r w_1\right)} \tag{7.43}$$

Rearranging and imposing the requirement that $R = 0$ at $r = w_2$ gives

$$R = J_n\left(k_r w_2\right) N_n\left(k_r w_1\right) - N_n\left(k_r w_2\right) J_n\left(k_r w_1\right) \tag{7.44}$$

The solutions of (7.44) provide the values for $k_r$ and their subsequent substitution in (7.41) gives the constant $B$. The transcendental equations are then formulated in the same manner as that for the dielectric disc in the previous section where $\psi(s)$ is now given by

$$\psi(s) = w\left[\frac{\left(k_r R(r)_{n-1} R(sr)_n\right)}{k_r^2 - s^2}\right] \tag{7.45}$$

### 7.3.5   Solution of the transcendental equation

The following will consider the solution of the transcendental equations derived in the preceding section with particular emphasis paid to the evaluation of the numerical integrals.

For clarity, the case of using a single basis term to describe the field in the disc is considered throughout the following and so the natural resonant frequencies of the cylindrical resonator structures are sought as the complex roots of the transcendental equation (7.29), which are of the form $\omega = \omega_{real} + j\omega_{imag}$. Once the complex frequency has been determined the Q, or Q-factor, of the resonator given by

$$Q = \frac{|\omega_{real}|}{2|\omega_{imag}|} \tag{7.46}$$

The field profiles may then be obtained though substitution of the calculated frequency back into the relevant expressions in a manner similar to that for the standard rectangular rib detailed in chapter 3.

Equation (7.29) contains an integral that is to be evaluated numerically in the complex *s*-plane and requires careful consideration due to the nature of the integrand function. Figure 7-8 illustrates the integration path for a purely real resonant frequency, $\omega$, in an open system with a slight material loss. In this case a branch cut of the Sommerfeld kind is chosen such that the upper Riemann surface has all outgoing waves decaying at infinity.

Considering the case of WGMs, the natural resonant frequencies are now complex and the SI approach introduces a closed system preventing access to $y = -\infty$. Therefore only two branch points at $s = \pm k_0 n_s$ are present, the situation now being as illustrated in figure 7-9(a).

In figure 7-9(a) the branch cut shown is equivalent to that of the Sommerfeld branch cut illustrated in figure 7-8, ensuring all waves decay at $y = \infty$. In this case performing the integral along the real axis results in a discontinuous behaviour of the integrand and thus the integral is no longer analytic.  The branch cuts are therefore

modified whilst obeying the necessary conditions that; (i) they start form $\pm k_0 n_s$ and

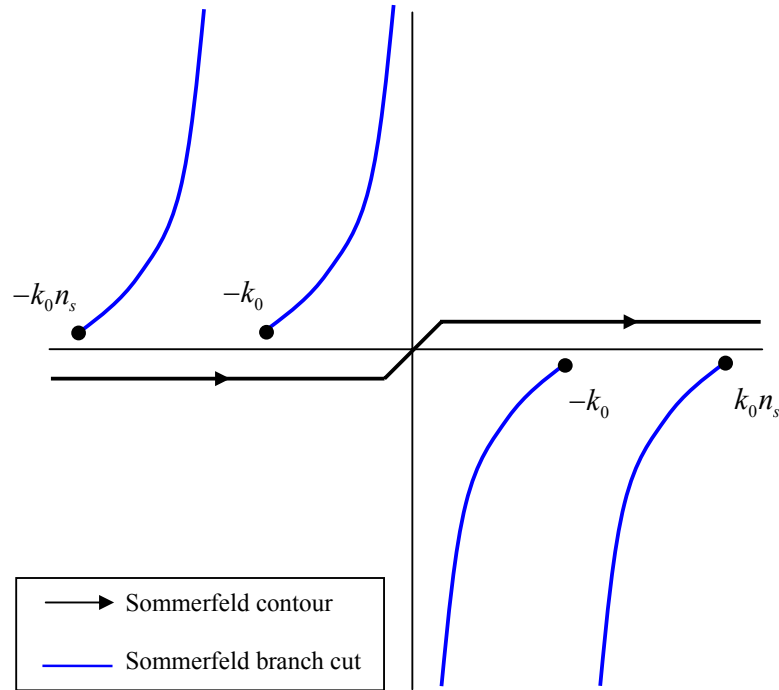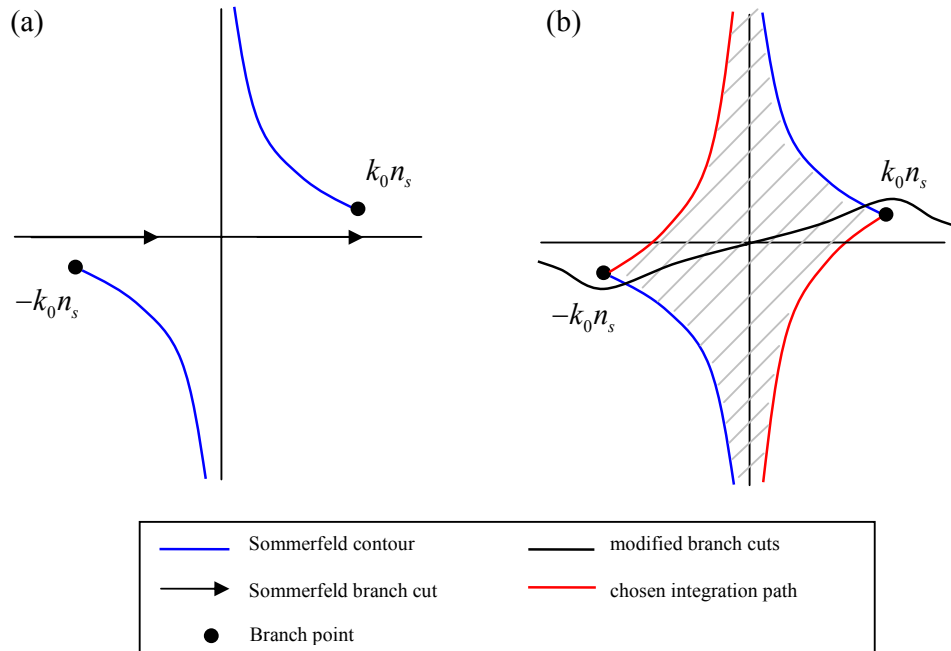(ii) they meet at $\infty$. The situation is now illustrated in figure 7-9(b).



**Figure 7-8.** Complex *s*-plane and the contour of integration for an open system with a slight material loss, with real natural frequency.

In figure 7-9(a) the branch cut shown is the equivalent to that of the Sommerfeld branch cut illustrated in figure 7-8, ensuring all waves decay at $y = \infty$. In this case performing the integral along the real axis results in a discontinuous behaviour of the integrand and thus the integral is no longer analytic. The branch cuts are therefore modified whilst obeying the necessary conditions that; (i) they start from $\pm k_0 n_s$ and

(ii) they meet at $\infty$. The situation is now illustrated in figure 7-9(b).

In figure 7-9 the branch cut shown is the equivalent to that of the Sommerfeld branch cut illustrated in figure 7-8, ensuring all waves decay at $y = \infty$. In this case performing the integral along the real axis results in a discontinuous behaviour of the integrand and thus the integral is no longer analytic. The branch cuts are therefore modified whilst obeying the necessary conditions that; (i) they start form $\pm k_0 n_s$ and (ii) they meet at $\infty$. The situation is now illustrated in figure 7-9(b).



**Figure 7-9** Complex *s*-plane and the contour of integration imposed under the SI

This ensures that the integral now remains smooth as $k_0$ moves across the real axis. Two regions have now been defined that depict the energy leakage regions. The shaded region in figure 7-9(b) has waves of the form $e^{-j\gamma_r y + |\gamma_i| y}$ and can therefore be said to represent outgoing and increasing waves, figure 7-10(a). The remainder of the

*s*-plane has waves of the form $e^{j\gamma_r y - |\gamma_i|y}$ and are thus incoming and decaying, figure 7-10(b).

(a)                                                    (b)
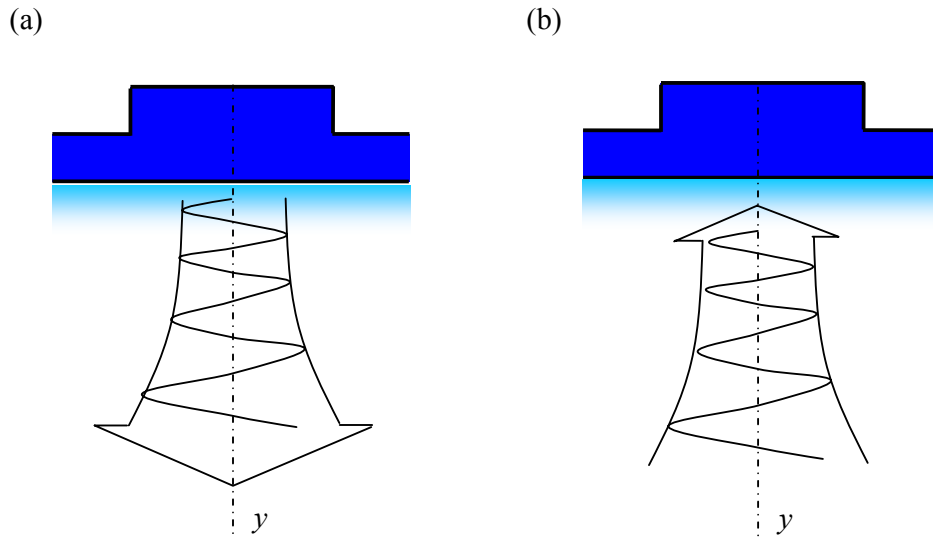


**Figure 7-10** Illustration of wave behaviour on corresponding to; (a) the shaded and (b) the non shaded regions of figure 7-9(b).

In practice there is no explicit need to follow the integration path as depicted in figure 7-9(b), instead the path as depicted in figure 7-11 is chosen. This allows for a simpler representation of the contour in the numerical algorithm.

## 7.4   Numerical Results

The following section is illustrates the effectiveness of the SI approach in the analysis of cylindrical dielectric structures. Because of the lack of suitable results in the literature at the present time, comparisons are drawn with semi-vectorial and
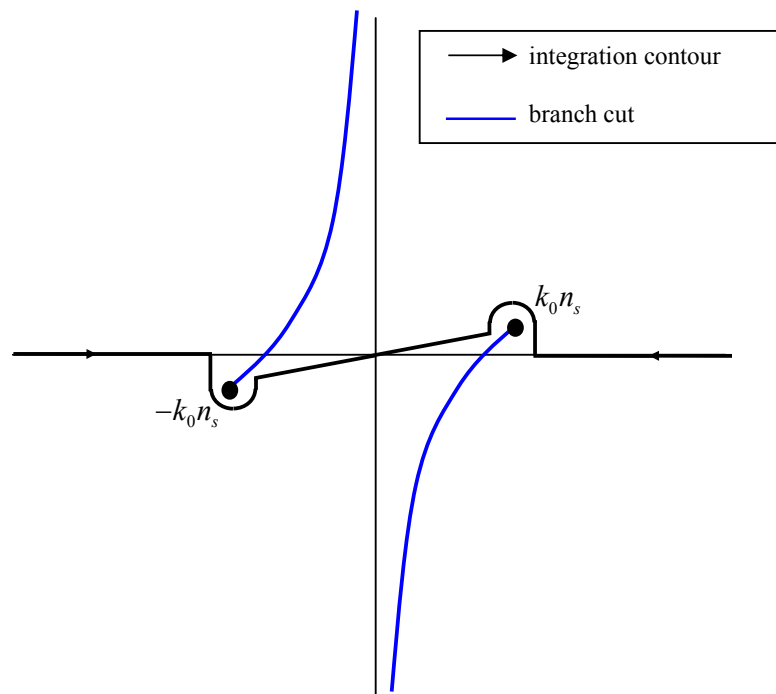
**Figure 7-11** Complex *S*-plane and the numerically evaluated contour of integration.

vectorial finite difference approaches, the later primarily being used to justify the polarised assumptions that are central to the SI methodology.

### 7.4.1  The dielectric disc resonator

Figure 7-12 illustrates the geometry of an air-clad circular dielectric resonator initially considered, consisting of a resonator of radius 4.5μm and height 4.5μm that has been etched into a layered substrate. The refractive indices of the disc and underlying substrate regions are 3.44 and 3.4 respectively, which are typical for an GaAs/AlGaAs material system at λ=1.15μm.
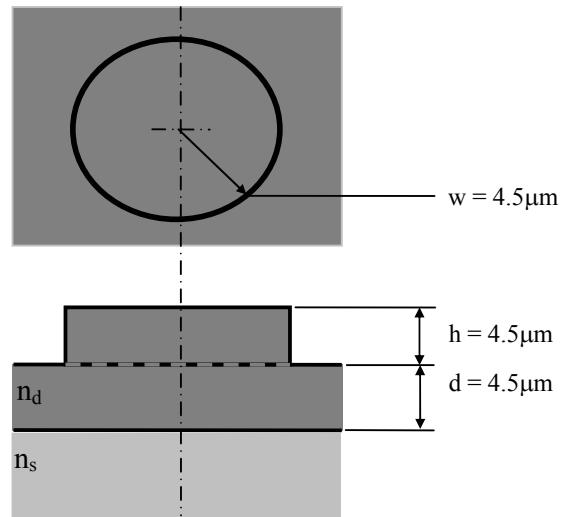
**Figure 7-12** Geometry of a dielectric micro-disc resonator; $n_d$=3.44 and $n_s$=3.40.

In order to justify the polarised assumptions used in the SI method and the semi-vectorial finite difference (SVFD) method, a vectorial finite difference scheme was used to examine the field distributions and the extent of the hybrid nature of the $WG_{15}$ mode. Figure 7-13 shows the resulting optical field distributions for the principal field component, $rE(r)$, and the minor field component, $E(y)$. As the diagrams are individually scaled a quantitive comparison was made of the total RMS electric field in each case, which yielded a ratio of 80:1. Since the minor field component is small, the polarised assumptions are justified. Also, the extent of the field penetration into the air cladding is seen to be slight and so the effective boundary approximation used in the SI method is also justified.

Figure 7-14 and figure 7-15 illustrate the cross sectional field amplitudes, $rE(r)$ resulting from the SI and the SVFD approaches for the $WG_2$ and the $WG_{15}$ modes respectively. These illustrate the validity of the effective width approach used. For the lower order resonances the field penetration into the air cladding is greatest. It is therefore intuitive to assume that the effective width assumption be weakest for these resonances. Nevertheless it is seen that the agreement between both the SI and SVFD method appear very good, figure 7-14. Moving to the higher order WGMs, excellent agreement is observed, figure 7-15.

(a)  (b)
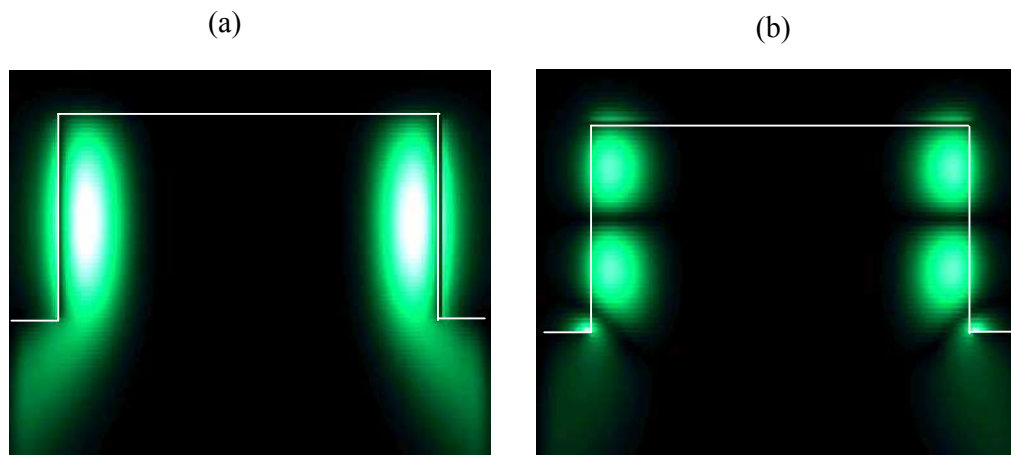


**Figure 7-13** Vector field distributions of the $WG_{15}$ mode of the device depicted in figure 7-12; (a) principal component $rE(r)$, (b) minor component $E(y)$.

Figure 7-16(a) and (b) illustrate the optical field distributions for the $WGE_{15,1,1}$ mode as given by the SI method and the SVFD method and very good agreement is observed between the two, again the slight field penetration shown by the SVFD method further justifies the assumptions of the SI method.
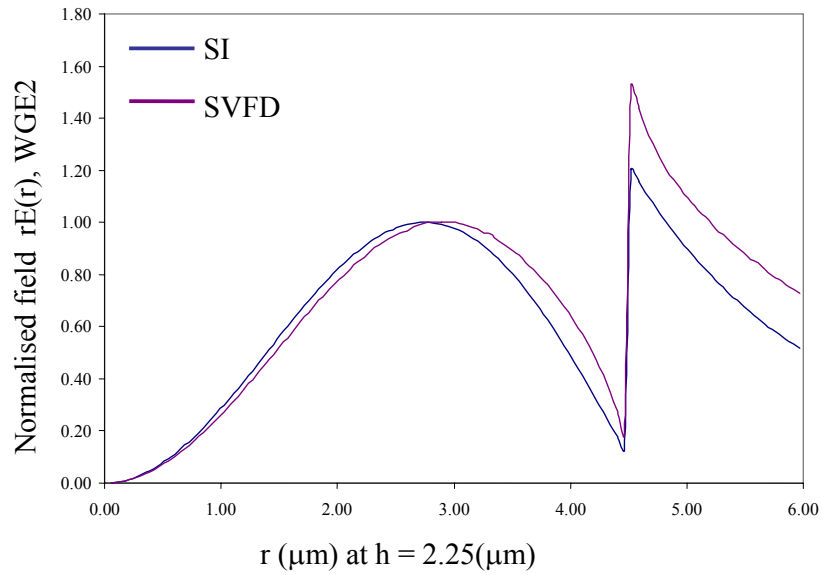
**Figure 7-14** Cross sectional field amplitude comparison for the $WGE_2$ mode supported by the structure of figure 7-12.
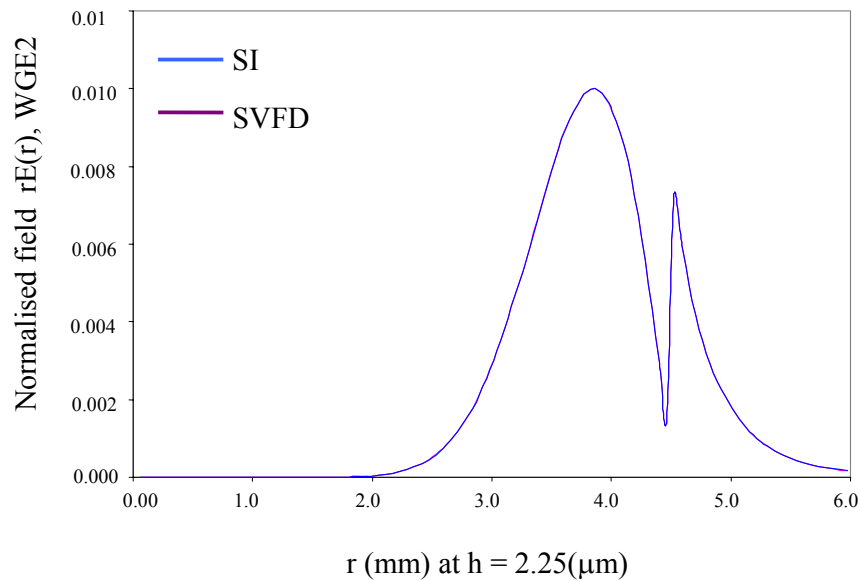


**Figure 7-15** Cross sectional field amplitude comparison for the $WGE_{15}$ mode supported by the structure of figure 7-12.

Figure 7-17 illustrates the convergence of the real part of the resonant wavelength predicted by the SI method with the number of terms used to represent the radial field distribution. It was found that 1 term was sufficient in providing agreement to 4 decimal places (i.e. to within 0.1nm) for the higher order WG modes, n > 12. Figure 7-18 compares the real component of the WG resonant wavelength obtained using the SI method with those obtained using SVFD schemes. $SIM_{1,2,3}$ utilise 1,2 and 10 terms in (7.29) respectively. $SVFD_{1,2}$ employ a mesh size of 0.03 and 0.06μm respectively over a problem window of 20 x 30μm. In the case of the SVFD, convergence was obtained to 5 decimal places, with agreement being obtained to the $4^{th}$ decimal place between the two methods. This is further illustrated in figure 7-9, which depicts the percentage difference between the real parts of the resonant wavelength calculated using the SI approach when compared to the SVFD results. In the case of single term SI, a 0.03% difference is achieved for the $WGE_{15}$ mode. This equates to an accuracy of better than 1nm. Increasing the number of terms used leading to a marginal increase in computation time and gives within ~0.1nm for the resonant wavelength.
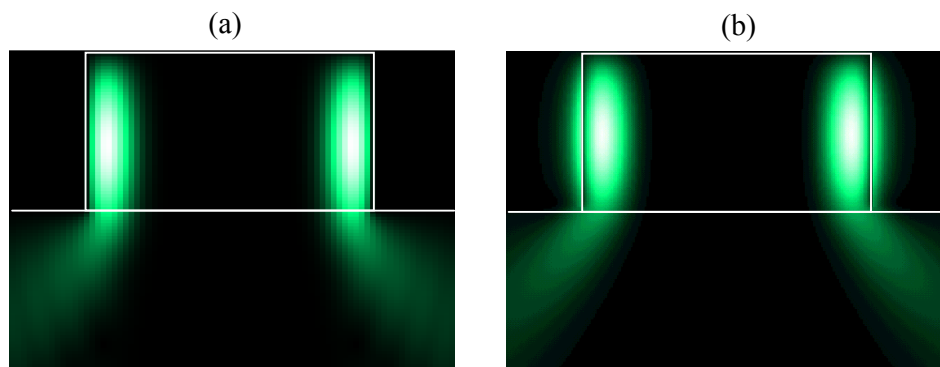


**Figure 7-16** Distributions for the $WGE_{15,1,1}$ mode; (a) SI method, (b) SV-FD.
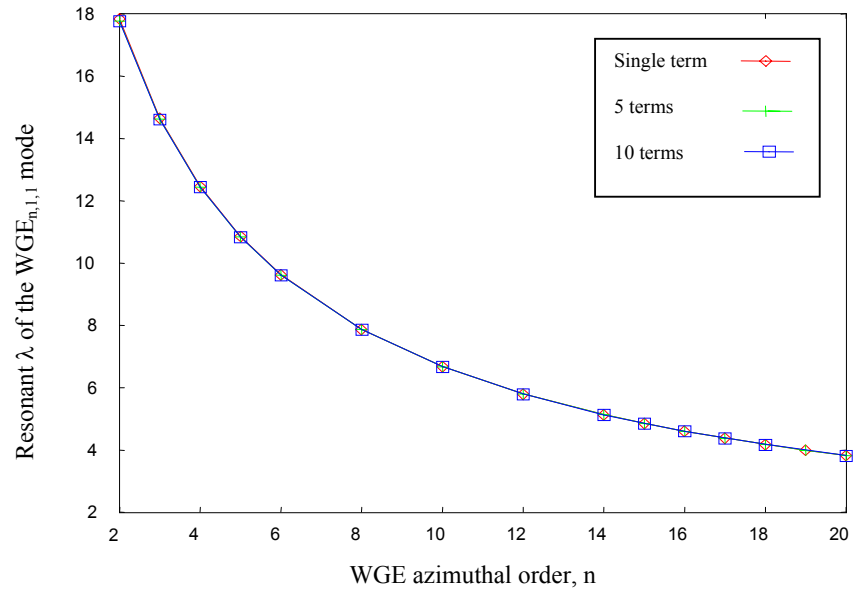
**Figure 7-17** Resonant wavelength, real part. Convergence with number of terms used in the SI field expansion.
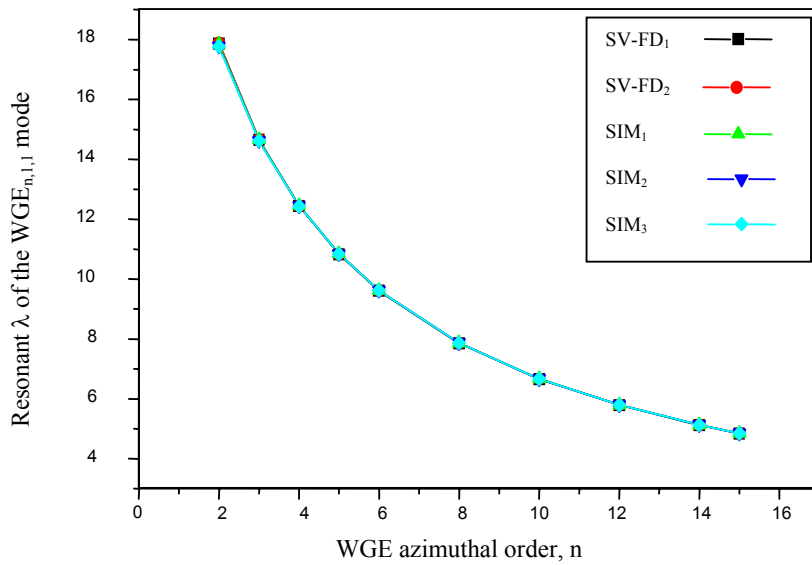


**Figure 7-18** Resonant wavelength, real part. Comparison of the SI approach with SV-FD.
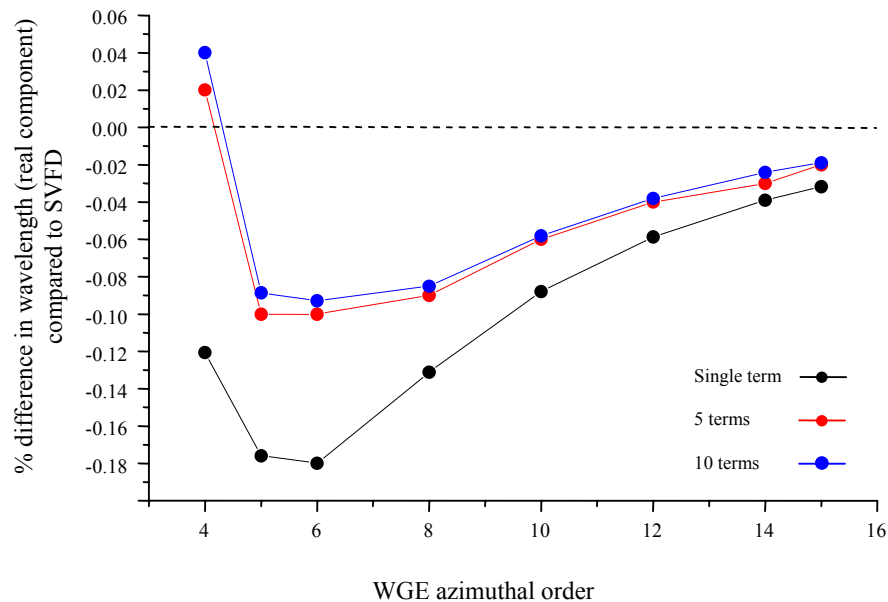
**Figure 7-19** Percentage difference in the SVFD results compared with the SI schemes for the real part of the resonant wavelength.

The quality factors or Qs of the dielectric disc illustrated in figure 7-12 as computed by the SI method utilising single and multiple terms are given in table 7-1 for a range of WGMs. These are compared with those obtained from three SVFD schemes of increasing accuracy. Reasonable agreement is seen between the two sets of results and improves, as expected, for the higher order WGMs. The method of effective widths being weaker for the low order WGMs due to the high penetration of the field into the air cladding.

| WGE$_{x,1,1}$ | SI Method Terms used in rib field expansion | | | Semi-vectorial Finite Difference Method Mesh size (µm), dx=dy | | |
|---|---|---|---|---|---|---|
| *x* | 1 | 5 | 10 | 0.1 | 0.05 | 0.03 |
| 5 | 26.0455 | 26.2361 | 26.1559 | 35.60557 | 35.6088 | 35.9223 |
| 10 | 86.6258 | 87.8294 | 87.6152 | 105.3472 | 105.2291 | 106.3471 |
| 15 | 188.5118 | 191.8645 | 191.5677 | 221.0763 | 220.9545 | 223.5693 |
| 20 | 336.5828 | 343.5479 | 342.8043 | 390.7318 | 390.0197 | 394.7403 |
| 25 | 545.8289 | 556.3344 | 555.8512 | 619.2382 | 618.5820 | 626.5044 |
| 30 | 814.0301 | 830.1652 | 829.5522 | 913.7674 | 912.5651 | 924.8995 |

**Table 7-1** The computed Q-factors for the WGMs of the device illustrated in figure 7-12**;** comparing the SI method against those results generated by SVFD schemes.

Figure 7-20 again illustrates the WGE$_{15,1,1}$ mode, but a further plot of the field in the plane of circular cross section is depicted showing the circular coherence of the WGM.
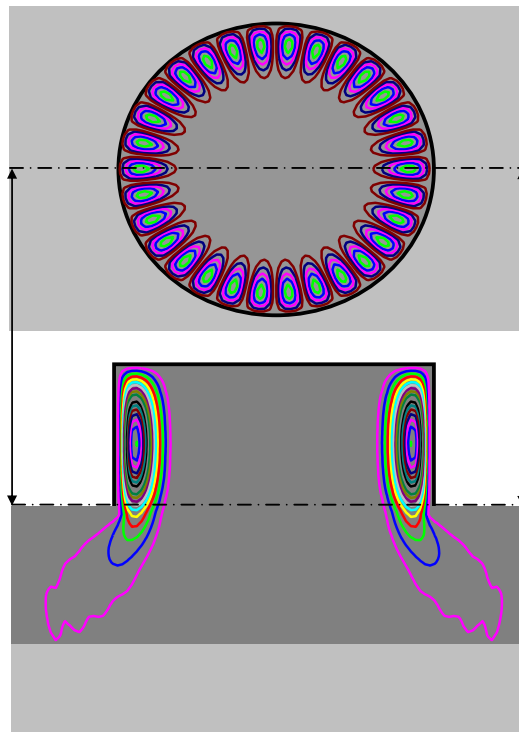


**Figure 7-20** Cross sectional field profile of the WGM$_{15,1,1}$.

### 7.4.2 The Dielectric Ring Resonator

Figure 7-21 illustrates the geometry of an air-clad circular dielectric ring resonator initially considered. The outer radius is fixed at 4.5μm and the inner radius is variable for the purposes of analysis.
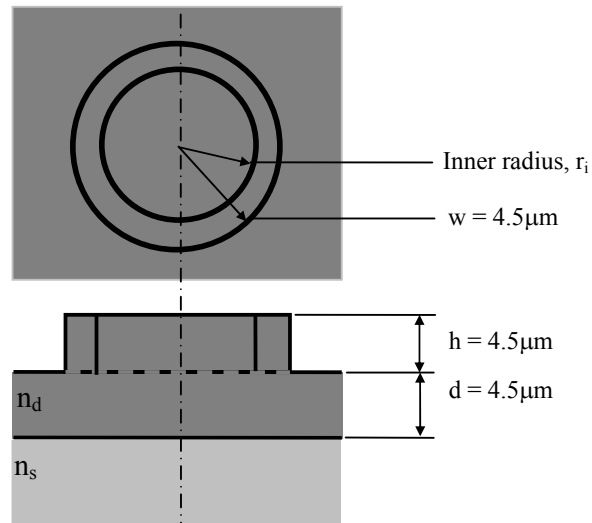


**Figure 7-21** Geometry of a dielectric micro-ring resonator; $n_d$=3.44 and $n_s$=3.40.

Figure 7-22 presents a SVFD analysis of the WGE $_{20,1,1}$ mode supported by the structure depicted in figure 7-21, where the inner radius ($r_i$ ) is increased from 0-3.75μm. At the time of writing numerical instabilities in the implementation of the SI approach prevented a complete comparison of results, although preliminary results are given for two cases and are shown on the same figure. As can be seen the optical characteristics of the device remain unperturbed as the inner dielectric material is removed, due to the absence of field in this region, for r<3.0μm. As the inner radius is increased further and the inner boundary of the ring impinges upon the WGM field
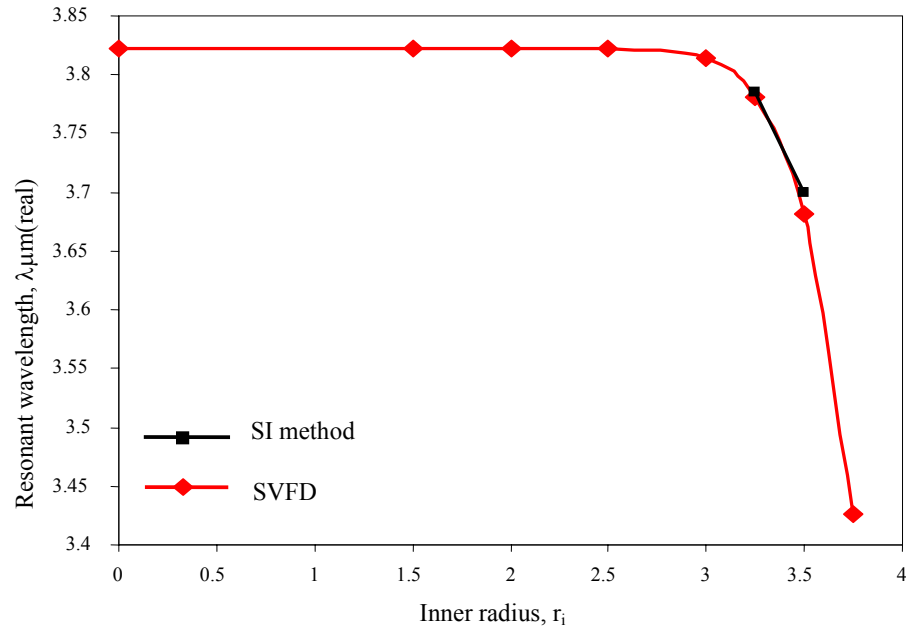
**Figure 7-22** Computed resonant wavelength (real part) versus the inner radius of the dielectric-ring resonator of figure 7-21, showing those obtained via an SVFD scheme together with preliminary results from the SI approach.
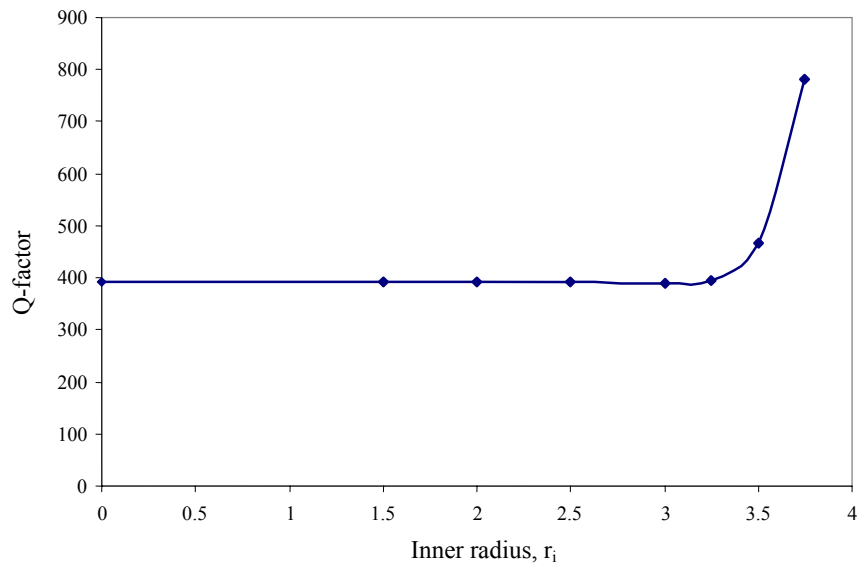


**Figure 7-23** Computed Q-factor versus the inner radius of the dielectric-ring resonator of figure 7-21, obtained via an SVFD.

a decrease in resonant wavelength frequency is observed, albeit small. The Q-factor, however is seen to increase dramatically, figure 7-23, as the inner radius increases.

## 7.5   Conclusions

Dielectric ring and disc resonators are attractive building blocks of various optical communications, lasers, and signal processing applications. Resonant frequencies and Q-factors were obtained for both circularly symmetric DRs using the SI method presented and compared with those obtained using a finite difference method implemented in cylindrical coordinates. Resonant frequencies of various modes can be located close to each other, and therefore for their proper classification, electric-field spatial distributions in DR were computed and presented. Due to versatility of the finite difference method, the numerical results obtained for resonant frequencies including those of high order modes are of high accuracy. Unfortunately, its implementation is time and memory consuming. The spectral index method offers higher efficiency, providing accurate results for resonant frequencies and a reasonable estimation of quality factors. Nevertheless, results obtained by both methods need further verification against data obtained by applying an accurate full-vectorial surface integral equation technique. However, the modelling undertaken provides quantitative and qualitative data, which provide a sufficient physical insight and guidance useful for practical design of photonic devices and systems containing disc dielectric resonators.

## 7.6   References

[7.1] D. Kajfez, P. Guillon, "Dielectric resonators", Artech House, 1996.

[7.2] S. C. Hagness, D. Rafizadeh, S. T. Ho, A. Taflove, "FDTD microcavity simulations: Design and experimental realization of waveguide-coupled single-mode ring and whispering-gallery mode disk resonators", IEEE Journal of Lightwave Technology, vol. 15, 1997.

[7.3] R. Orta, P. Savi, R. Tascone, and D. Trinchero, "Synthesis of Multiple Ring-Resonator Filters for Optical Systems", *IEEE Photon. Tech. Lett*., vol. 7, pp.1447-1449, 1995.

[7.4] B. E. Little, S. T. Chu, H. A. Haus, J. Foresi, and J. –P. Laine, "MIcroring resonator channel dropping filters", IEEE Journal of Lightwave Technology, vol. 15(6), pp. 998-1005.

[7.5] D. Rafizadeh, J. P. Zhang, R. C. Tiberio, and S. T. Ho, "Propagation loss measurements in semiconductor microcavity ring and disk resonators", IEEE Journal of Lightwave Technology, vol. 16(7), pp.1308-1313, 1998.

[7.6] B. E. Little, J. S. Foresi, G. Steinmeyer, E. R. Thoen, S. T. Chu, H. A. Haus, E. P. Ippen, L. C. Kimerling, and W. Greene, "Ultra-compact Si-SiO$_2$ microring resonator optical channel droping filters", IEEE Photonics Technology Letters, vol. 10(4), pp. 549-551, 1998.

[7.7] B. E. Little, S. T. Chu, W. Pan, D. Ripin, T. Kaneko, Y. Kokubun, and E. Ippen, "Vertically coupled glass microring resonator channel dropping filters", IEEE Photonics Technology Letters, vol. 11(2), pp. 215-217, 1999.

[7.8] S. T. Chu, B. E. Little, W. Pan, T. Kaneko, S. Sato, Y. Kokubun, "An eight-channel add-drop filter using vertically coupled microring resonators over a cross grid", IEEE Photonics Technology Letters, vol. 11(6), pp. 691-693, 1999.

[7.9] F. C. Blom, H. Kelderman, H. J. W. M. Hoekstra, A, Driessen, Th. J. A. Popma, S. T. Chu, B. E. Little, "A single channel dropping filter based on a cylindrical microresonator", Optics Communications, vol. 167, pp. 77-82, 1999.

[7.10]  X. H.Jiao, P. Guillon, L.A. Bermudez, "Resonant frequencies of whispering-gallery dielectric resonator modes", IEE Proc., vol.134, Pt.H, no.6, pp.497-501, 1987.

[7.11]  J. Krupka, "Computation of frequencies and intrinsic Q-factors of $TE_{0mn}$ modes of dielectric resonators", IEEE Trans. Microwave Theory Tech., vol. 33, no. 3, pp. 274-277, 1985.

[7.12]  R.K. Mongia, P. Bhartia, "Accurate conductor Q-factor of dielectric resonator placed in an MIC environment", IEEE Trans. Microwave Theory Tech., vol. MTT-41, no. 3, pp. 445-449, 1993.

[7.13]  J. Lee, Y.-S. Kim, "A new method of accurately determining resonant frequencies of cylindrical and ring dielectric resonators", IEEE Trans. Microwave Theory Tech., vol. MTT-47, no. 2, pp. 706-708, 1999.

[7.14]  J. Krupka et al, "Study of whispering gallery modes in anisotropic single-crystal dielectric resonators", IEEE Trans. Microwave Theory Techniques, vol. 42, no. 1, 1994.

[7.15]  A. Navarro, M. J. Nunez, "FDTD method coupled with FFT: a generalization to open cylindrical devices", IEEE Trans. Microwave Theory Tech., vol. 42, no. 5, pp. 870-874, 1994.

[7.16]  J. A. Pereda, et al, "Computation of resonant frequencies and quality factors of open dielectric resonators by a combination of FDTD and Prony's methods", IEEE Microwave and Guided Wave Letters, vol.2, no.11, 1992.

[7.17] A.W. Glisson, D. Kajfez, J. James, "Evaluation of modes in dielectric resonators using a surface integral equation formulation", IEEE Trans. Microwave Theory Tech., vol. 31, no. 12, pp. 1023-1029, 1983.

[7.18] A.A. Kucharski, "Resonances in heterogeneous dielectric bodies with rotational symmetry - volume integral-equation formulation", IEEE Trans. Microwave Theory Tech., vol. 48, no. 5, pp. 766-770, 2000.

[7.19] D. Cros, P. Guillon, "Whispering gallery dielectric resonator modes for W-band devices", IEEE Trans. Microwave Theory Techniques, vol. MTT-38, no. 11, pp. 1667-1673, 1990.

[7.20] D. Kajfez, "Incremental frequency rule for computing the Q-factor of a shielded $TE_0$ dielectric resonator", *IEEE Trans. Microwave Theory Tech*., vol. 32, no. 8, pp. 941-943, 1984.

[7.21] M. Yousefi, S.K. Chaudhuri, S. Safavi-Naeini, "GIBC formulation for the resonant frequencies and field distributions of a substrate-mounted dielectric resonator", IEEE Trans. Antennas Propagat., vol. 42, no. 1, pp. 38-46, 1994.

[7.22] S. W. Chen, K.A. Zaki, "Dielectric ring resonators loaded in waveguide and on substrate", IEEE Trans. Microwave Theory Techniques, vol. MTT-39, no. 12, pp. 2069-2074, 1991.

[7.23] A. Kishk, M.R. Zunoubi, D.Kajfez, "A numerical study of a dielectric disk antenna above grounded dielectric substrate", IEEE Trans. Antennas Propagat., vol. 41, no. 6, pp. 813-821, 1993.

[7.24] G. Annino, M. Cassetari, I. Longo, M. Martinelli, "Whispering gallery modes in dielectric resonators: characterization at the millimeter wavelengths", IEEE Trans. Microwave Theory Techniques, vol. MTT-45, no. 11, pp. 2025-2034, 1997.

[7.25]  S.-L. Lin, G.W. Hanson, "An efficient full-wave method for analysis of dielectric resonators possessing separable geometries immersed in inhomogeneous environments", IEEE Trans. Microwave Theory Tech., vol. MTT-48, no. 1, pp. 84-99, 2000.

[7.26]  Lord Rayleigh, "The problem of the whispering gallery", Philos. Mag., vol. 20, pp.100-1004, 1910.

[7.27]  R. D. Richtmyer, "Dielectric resonators", Journal of Applied Physics, vol. 10, pp. 391-398, 1939.

# Chapter 8   The Spectral Index Method: Optical Circuit Analysis

The ability to optimise the performance of optoelectronic circuits over a range of operational parameters and fabrication tolerances is foremost in the designers mind. To reduce chip length and provide increased component density, whilst at the same time enhancing performance over a range of wavelengths is a typical example. The ability to investigate the effects of tolerancing and integration upon device performance is highly desirable for its successful exploitation. This chapter describes the extensions made to the Spectral Index (SI) method to provide a new simulation tool, well suited to the design and optimisation of multi-mode interference coupler based devices.

## 8.1   Introduction

Coupling of power between optical components takes place through both guided and radiation modes. When considering waveguide configurations and optical circuits derived from them the optical components may be considered as individual blocks, each containing one or more waveguides, and connected to each other at well defined ports. The complete circuit may be then described in terms of a scattering matrix (S-matrix), [8.1]. Essential to the development of the S-matrix is the accurate calculation of the modal propagation constants of the optical circuit's constituent blocks. In the following work the efficiency of SI method is exploited in order to

obtain the complete modal spectrum of each discrete waveguide block to a high accuracy in a matter of seconds. Once the modal properties of each block have been calculated they can then be joined using an S-matrix allowing a relatively simple representation of a complex circuit. Such circuits may have large aspect ratios, i.e. microns wide and millimetres in length. These would prove prohibitive for 3D numerical methods, such as the finite difference beam propagation method (FD-BPM), as sufficient discretisation of the problem space would require significant computational resources. Additionally, computationally efficient FD-BPM algorithms assume paraxial propagation which is invalid for the classes of waveguide devices that support highly divergent fields, such as those discussed later in this chapter. FD-BPM applied to these devices would therefore require the implementation of wide-angle techniques (§2.8.3), resulting in a further increase in computational overheads. The suitability of the SI approach is demonstrated in the remainder of this chapter through its application to the design and optimisation of that range of multi-mode interference based devices for which the polarisation assumption of the SI method holds.

## 8.2   Multi-mode Interference Devices

Compact Multi-mode interference (MMI) based devices are extremely versatile components that form the basis of a wide range of optoelectronic devices, for example; couplers [8.2]- [8.5], optical beam splitters/recombiners [8.6], switches [8.7] and more recently wavelength multiplexers/demultiplexers [8.8]-[8.11]. MMI components are designed around the principle of self imaging, [8.12]-[8.13], which is described in [8.12] as

> *"Self-Imaging is a property of multimode waveguides by which an input field profile is reproduced in single or multiple images at periodic intervals along the propagation direction of the guide".*

A MMI device consists of a central multi-moded waveguide with *N* single mode input waveguides and *M* single mode output waveguides. Figure 8-1 illustrates a 3x3 MMI splitter.
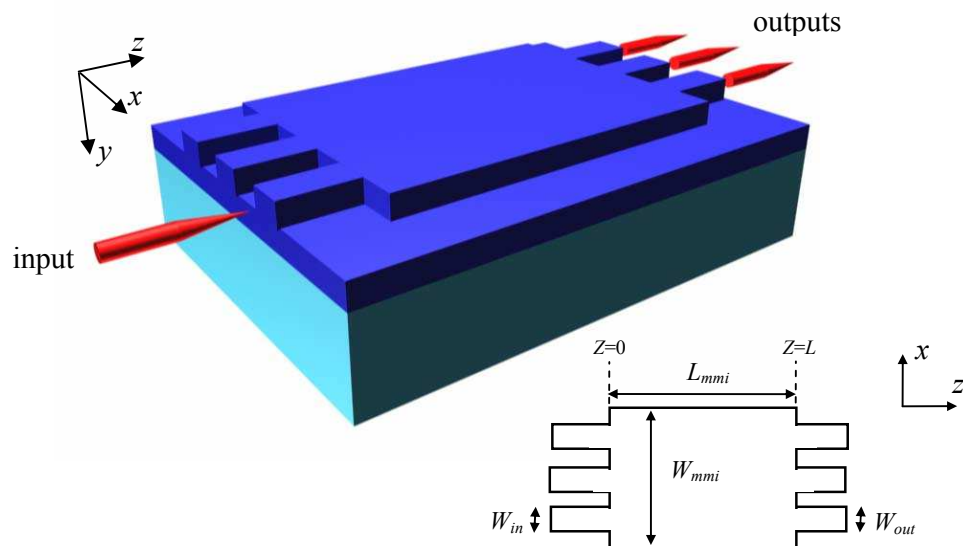


**Figure 8-1** Illustration of a 3x3 MMI splitter.

## 8.3   The SI Approach

The following outlines the application of the SI method to the problem of circuit analysis; obtaining the modal characteristics of each waveguide section, propagation of the modal field and joining the sections to form a circuit through overlap integrals.

### 8.3.1  Field Descriptions

Using the SI method the complete modal spectrum of each discrete waveguide section can be obtained in a straightforward manner. Typical computation times being < 1 minute for the examples given in the following sections. The total field, $\Psi_{guide}(x,y,z)$, in an input guide at $z = 0$ is then given by the superposition of all modes of that guide

$$\Psi_{guide}(x,y,0) = \sum_{n,m} A_{n,m} E_{n,m}(x,y) \tag{8.1}$$

where the subscripts $n$, $m$ denote the lateral and vertical mode numbers respectively and $A_{n,m}$ are modal amplitudes.

### 8.3.2  Overlap Integrals

The excitation of an optical field in an output guide by the field in an input guide is determined by the overlap of those fields. Assuming excitation by an input field $\Psi_{guide}(x,y,z)$ at $z = 0$ that is normalised such that

$$\iint \Psi(x,y)\Psi^*(x,y) = 1 \tag{8.2}$$

the excited modal amplitudes, $A_{n,m}$ are then, in general, determined by the overlap integral

$$A_{n,m} = \frac{\iint \Psi(x,y) E_{n,m}^*(x,y) \, dxdy}{\iint E_{n,m}(x,y) E_{n,m}^*(x,y) \, dxdy} \tag{8.3}$$

which are subsequently normalised such that

$$\iint E_{n,m}(x,y) E_{n,m}^*(x,y) \, dxdy = 1. \tag{8.4}$$

(8.3) then simplifies to

$$A_{n,m} = \iint \Psi(x,y,0) E_{n,m}^*(x,y) \, dxdy \, . \tag{8.5}$$

In the case of the SI method the process of evaluating this type of overlap integral is greatly simplified due to the definitions describing the fields in the rib. Considering the two separate regions; the rib $(\Omega_1)$ and the underlying multilayered substrate region $(\Omega_2)$. The field in each of these regions as described earlier (§3.4) are,

$$E = \sum_m F_m(x) G_m(y) \tag{8.6}$$

in the rib and below the rib.

$$\phi(s,y) = f(s) g(s,y) \tag{8.7}$$

Performing the overlap between an input and output waveguide of the fields in each of these regions gives

$$\langle \Psi_{in}(x,y), \Psi_{out}(x,y) \rangle = \iint\limits_{\Omega_1} dxdy \left( \sum_m F_m(x)G_m(y) \right) \cdot \left( \sum_n F_n^*(x)G_n^*(y) \right) \quad (8.8)$$

for the rib region, where $\Omega_1$ is taken to be the cross section of the input guide only and the subscripts $m,n$ denote those modes in the input and output guides respectively. Re-writing (8.8)

$$\langle \Psi_{in}(x,y), \Psi_{out}(x,y) \rangle = \int\limits_{-W}^{W} dx \left( \sum_m F_{in}^m(x) \sum_n F_{out}^n(x)^* \right) \cdot \int\limits_0^{-H} dy \left( G_{in}^m(y) G_{out}^n(y)^* \right) (8.9)$$

and performing the integral over $x$

$$\langle \Psi_{in}(x,y), \Psi_{out}(x,y) \rangle = \int\limits_0^{-H} dy \sum_m \delta(s_m - s_n) \left( G_{in}^m(y) G_{out}^n(y)^* \right) \quad (8.10)$$

where $s_m$ and $s_n$ are given by

$$s_q = (2q-1)\pi/2W \quad , \quad q\pi/W$$

and $q = m,n$ for symmetric and antisymmetric modes respectively. Finally (8.10) can now be reduced to

$$\langle \Psi_{in}(x,y), \Psi_{out}(x,y) \rangle = \int\limits_0^{-H} dy \sum_m \left( G_{in}^m(y) G_{out}^n(y)^* \right) \quad (8.11)$$

For the multilayered region below the rib

$$\left\langle \varphi_{in}(s,y), \varphi_{out}(s',y) \right\rangle =$$
$$\frac{1}{2\pi} \iiint\limits_{\Omega_2} dy\,ds\,ds' \left( f_{in}(s)\, g_{in}(s,y) \right) \left( f_{out}(s')\, g_{out}(s',y) \right) \tag{8.12}$$

where $s$ and $s'$ denote the spectral variable in the input and output guides respectively. Using the fact that

$$f(s) = \int dx\, F(x) e^{jsx} \tag{8.13}$$

(8.12) may be expressed as

$$\left\langle \varphi_{in}(s,y), \varphi_{out}(s',y) \right\rangle =$$
$$\iiiint\limits_{\Omega_2} dx\,dy\,ds\,ds' \left( F_{in}(x) e^{jsx} g_{in}(s,y) \right) \left( F_{out}(x) e^{js'x} g_{out}(s',y) \right) \tag{8.14}$$

Performing the integral over $x$ gives

$$\left\langle \varphi_{in}(s,y), \varphi_{out}(s',y) \right\rangle = \iiint\limits_{\Omega_2} dy\,ds\,ds'\ \delta(s-s') g_{in}(s,y) \cdot g_{out}(s',y) \tag{8.15}$$

Evaluating the integral over $ds'$ reduces (8.15) to

$$\left\langle \varphi_{in}(s,y), \varphi_{out}(s',y) \right\rangle = \iint\limits_{\Omega_2} dy\,ds\ g_{in}(s,y) \cdot g_{out}(s,y) \tag{8.16}$$

In (8.16) the integration with respect to $y$ can be performed analytically leaving a function of $s$ alone that is required to be integrated numerically. Thus it is seen that in the SI method evaluation of the overlap integral it is reduced to a one-dimensional integral. Provided one is dealing with an optical circuit that consists of rib waveguides etched to the same depth, as would usually be the case in practice.

Where the output guide is offset with respect to the input guide by a distance $d$, figure 8-2, the $x$ dependent terms for the output guide in (8.9) and (8.14) are modified such that

$$\langle \Psi_{in}(x,y), \Psi_{out}(x,y) \rangle =$$
$$\int_{-W}^{W} dx \left( \sum_m F_{in}^m(x) \sum_n F_{out}^n(x-d)^* \right) \cdot \int_0^{-H} dy \left( G_{in}^m(y) G_{out}^n(y)^* \right) \qquad (8.17)$$

and

$$\langle \varphi_{in}(s,y), \varphi_{out}(s',y) \rangle =$$
$$\iiint_{\Omega_2} dx\,dy\,ds\,ds' \left( F_{in}(x) e^{jsx} g_{in}(s,y) \right) \left( F_{out}(x-d) e^{js'x} g_{out}(s',y) \right) \qquad (8.18)$$

For multiple input guides the excitation is additive, so the overlaps are evaluated for each input guide and their contributions summed.

### 8.3.3 Field Propagation

Once the amplitudes of the excited modes have been obtained, the propagation of the excited modal field from the plane $z = 0$ to $z = L$ is then achieved through

$$\Psi_{z=L} = \sum_{n,m} E_{n,m}(x,y,0)e^{-j\beta_{n,m}L} \tag{8.19}$$
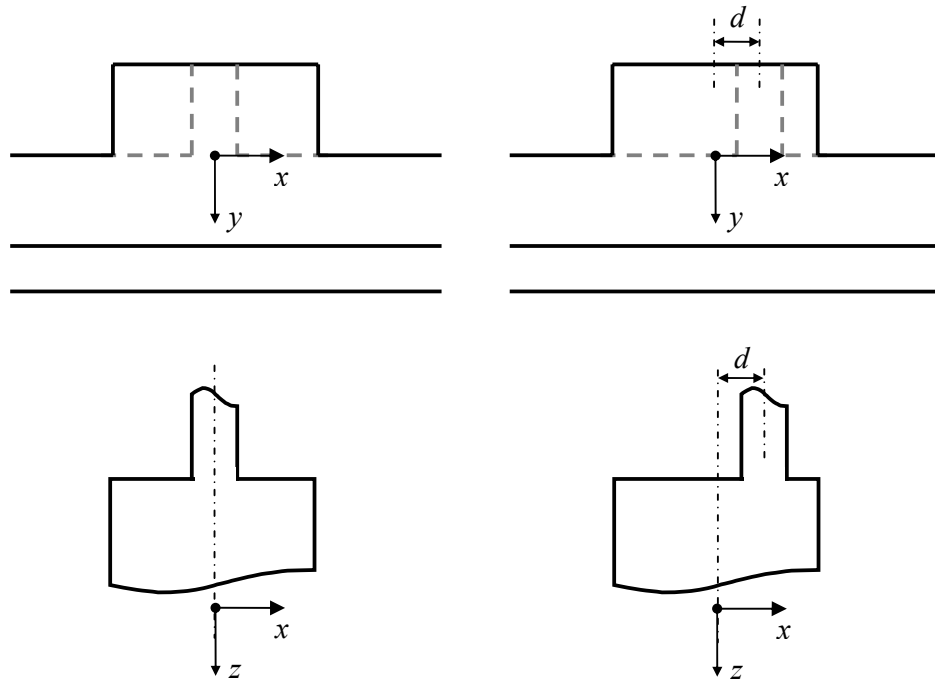


**Figure 8-2** Cross sectional and plan view of single waveguide to waveguide junction; (a) symmetric junction and (b) offset junction.

The excitation of the output guides at $z = L$ is calculated in the same manner, whereby the overlap is performed between the normalised output field and the normalised MMI field. This process is then repeated for the whole circuit; calculation of the total excited field at an interface, propagation to the next interface, calculation of excited field and so on for each interface. The remainder of this chapter will apply the principles discussed above to the analysis of several MMI-based devices.

## 8.4   Analysis of MMI Based Optical Devices

The following analyses of several MMI based devices are used to illustrate the applicability of the method previously discussed to a range of practical devices. The following sub-sections assume a constant epitaxial structure, figure 8-3, and a constant etch depth of $d = 4.47\mu m$. The corresponding refractive index distribution is given in table 8-1. The epitaxial structure has been successfully shown to provide an ideal basis for the fabrication of low loss rib waveguides suitable for integrated optical devices, [8.14]. The epitaxy allows for the fabrication of deeply etched rib waveguides with strong lateral confinement. The high lateral confinement reduces the cross-talk between waveguides allowing for higher levels of integration. These structures are also ideal for multimode interference devices where the high lateral confinement results in highly accurate self imaging [8.14].
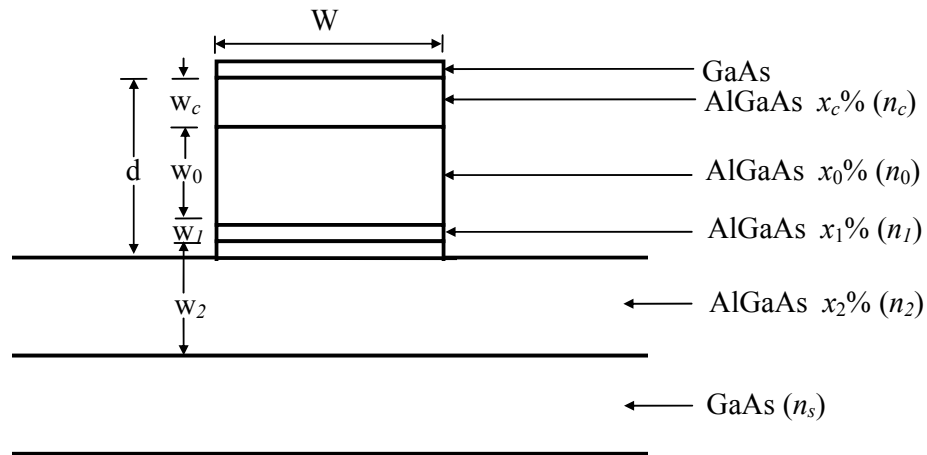


**Figure 8-3** Schematic of the epitaxial structure showing layer thickness (*w*), AlGaAs alloy composition (*x*) and their associated refractive indices (*n*).

| Layer | thickness(μm) | Al (%) | Refractive index, λ=1.064μm, $n$ |
|---|---|---|---|
| Cap layer (GaAs) | 0.1 | 0 | 3.48043422 |
| Upper cladding ($n_c$) | 1.2 | 20 | 3.36755329 |
| Core layer ($n_0$) | 2.5 | 5 | 3.45189744 |
| Lower cladding ($n_1$) | 0.3 | 15 | 3.39552660 |
| Spacer layer | 0.5 | 5 | 3.45189744 |
| Lower cladding ($n_2$) | 2.8 | 6.5 | 3.44339260 |
| Substrate ($n_s$) | ___ | 0 | 3.48043422 |

**Table 8-1** Epitaxy parameters of the structure in figure 8-3, [8.14].

## 8.4.1  1x*N* MMI Optical Beam Splitter

Optical beam or power splitting is an important requirement for OEICs. MMI devices allow accurate and low loss beam splitting over a relatively short device length, figure 8-4 illustrates a centre fed 1x2 splitter. The input and output waveguides, guides 1, 3 & 4 respectively, in figure 8-4, have a width of 4.4μm and the MMI section is 17.6μm wide. The etch depth is 4.7μm . The output waveguides are symmetrical about the $x = 0$ axis at a pitch of 8.8μm . The operational wavelength is 1.064μm .

The efficiency of the splitter is ultimately determined by the length of the MMI section. Figure 8-5 shows the device insertion loss calculated using the SI approachversus MMI length. Insertion loss is defined as

$$\text{Insertion loss(dB)}=-10\log\left(\left(P_{guide3} + P_{guide4}\right)/P_{guide1}\right) \qquad (8.20)$$

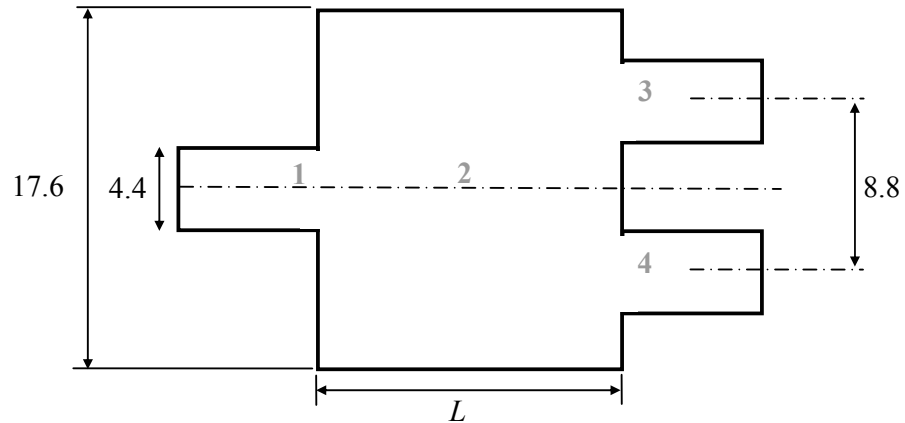where $P_{guide..}$ is the total power carried in the guide.



**Figure 8-4** Schematic of a 1x2 MMI splitter (all dimensions are in microns).

From figure 8-5 the optimum MMI length can be predicted and was found to be $L = 502\mu m$. Figure 8-6 illustrates the optical field intensity profile along the device for $L = 502\mu m$, clearly showing the equally split field at the output guides. A relationship between the number of output guides and the length of the MMI section for a symmetrically fed 1x$N$ optical beam splitter is given in [8.6] as

$$L = \Lambda/N \qquad (8.21)$$

where
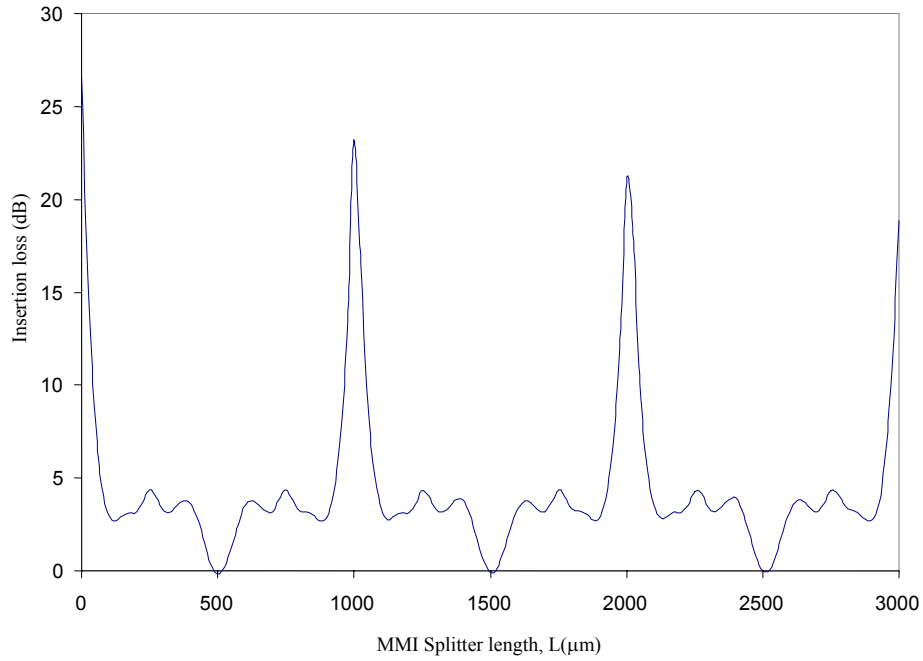
$$\Lambda = nW^2/\lambda_0 , \qquad (8.22)$$

**Figure 8-5** Insertion loss of the 1xN splitter calculated using the SI method versus the MMI guide length, L.
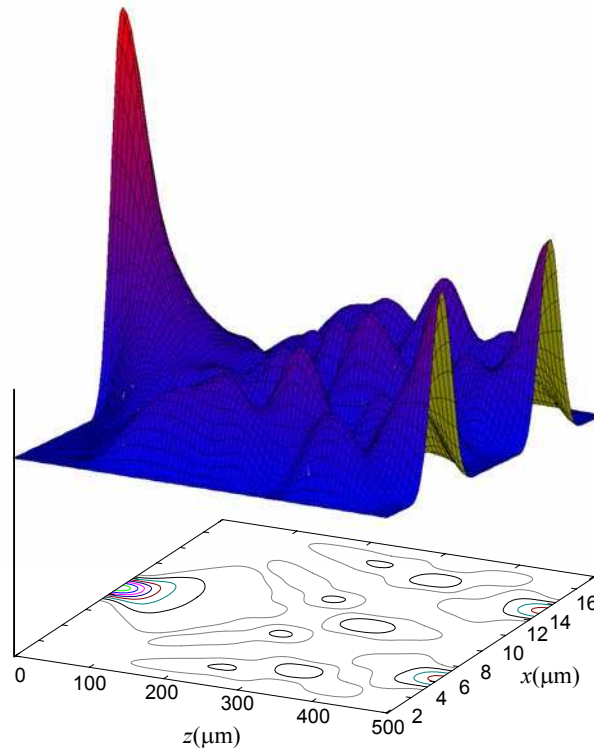


**Figure 8-6** The optical field intensity pattern in the 1x2 splitter MMI guide calculated using the SI method.

where $n$ is the effective refractive index of the guide ($n_{eff}$ = 3. 3.44739) and $\lambda_0$ is the free space wavelength. The pitch of the output guides being given by $p = W/N$. Equations (8.21) and (8.22) predict an optimal MMI length of 501.8μm which is in agreement with the simulated results. Figure 8-7 - Figure 8-9 illustrate the geometry and simulation of a 1x4 splitter with an MMI guide effective index of $n_{eff}$ = 3. 3.44746. Again the analysis was found to match the theory presented in [8.6], predicting an MMI section length of 564.5μm.
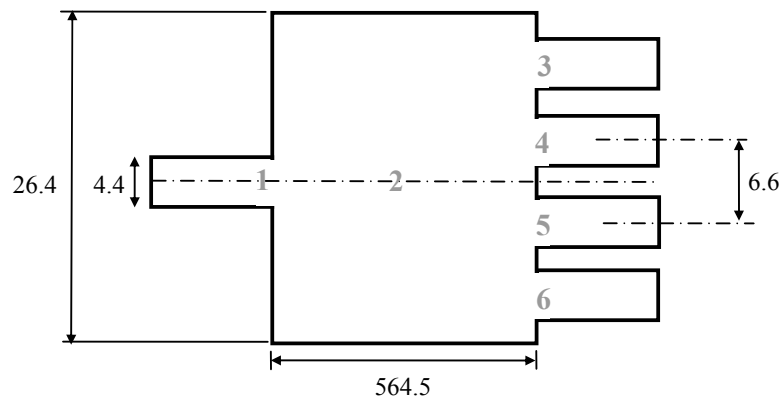


**Figure 8-7** Schematic of a 1x4 MMI splitter (all dimensions are in microns).

### 8.4.2  *N*x*N* Power Recombiner

MMI devices can also perform the reverse role to the previously discussed power splitters. Power in $N$ input guides may be combined and evenly distributed amongst $N$ output guides. Figure 8-10 illustrates a 2x2 3dB coupler that combines the power at the inputs and evenly couples it to the output waveguides.
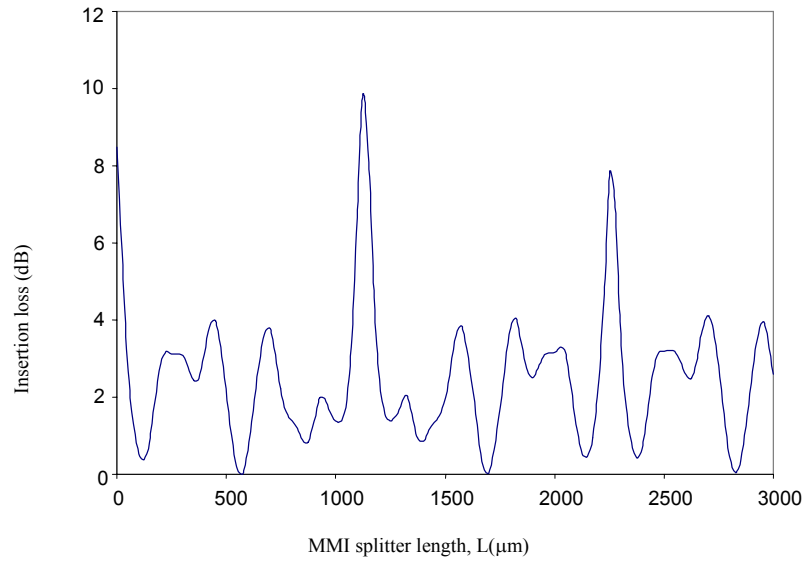
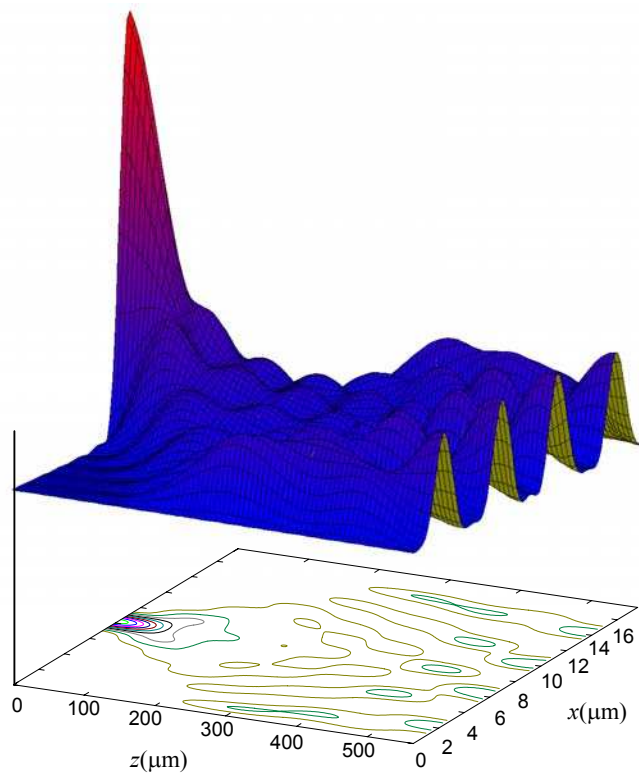**Figure 8-8** Insertion loss of the 1x4 splitter calculated using the SI method versus the MMI guide length, L.



**Figure 8-9** The optical field intensity pattern in the 1x4 splitter MMI guide calculated using the SI method
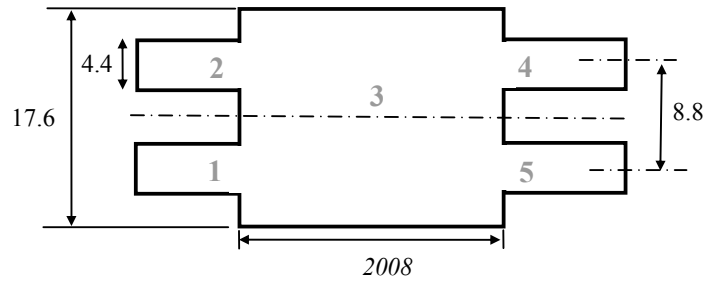
**Figure 8-10** 2x2 power recombiner.

A relationship between the number of output guides and the length of the MMI section for a symmetrically fed *N*x*N* optical beam recombiner as given in [8.6] is

$$L = 4\Lambda/N \qquad (8.23)$$

and

$$\Lambda = nW^2/\lambda_0 \qquad (8.24)$$

These equations predict a length of 2008μm for the MMI guide. Figure 8-11 illustrates the SI simulations of the three modes of operation of the device; (a) and (b) acting as a 3dB coupler and (c) as a power recombiner/3dB coupler.

### 8.4.3 1x2 Optical Switch

MMI devices can provide a simple optical switching solution. By cascading a 1x*N* splitter and an *N*x*N* recombiner and then electrically modulating the refractive indices of the input guides to the recombiner, so as to introduce an optical phase shift

along its length, an optical switch may be formed. The case of a 1x2 optical switch is illustrated in figure 8-12. By modulating the electro-optic guides (eog3 and eog4) the optical beam can be switched between the output guides 6 and 7.
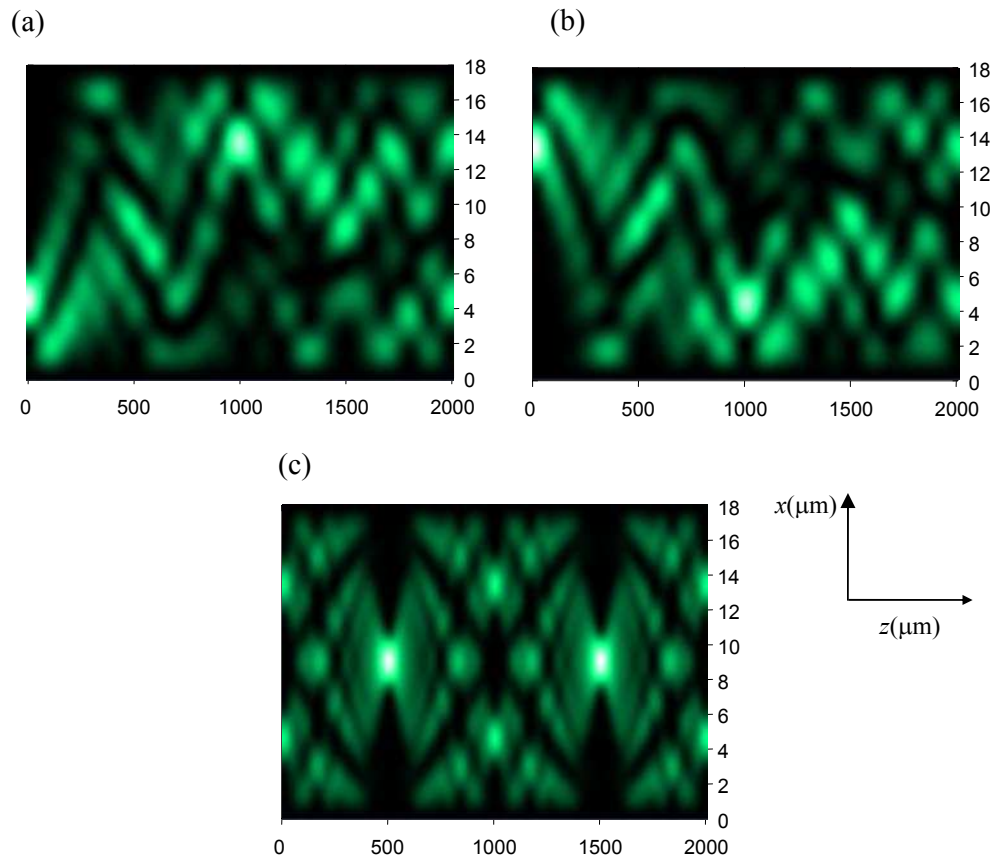
(a)

(b)

(c)



**Figure 8-11** SI simulations of a2x2 MMI recombiner operating as; (a),(b) 3dB coupler, and (c) 3dB recombiner 3dB coupler. All dimensions in microns.
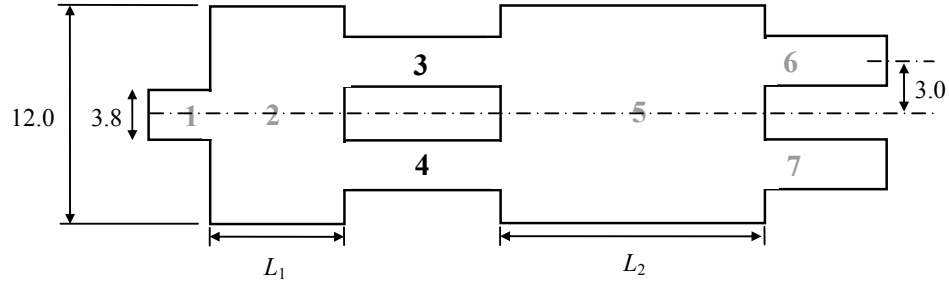
**Figure 8-12**  Illustration of a 1x2 optical switch (all dimensions in microns).

From equations (8.21) and (8.23) the lengths $L_1$ and $L_2$ are given as 502μm and 2008μm respectively. The electro-optic guides were taken to add a phase change of 0-2π when electrically modulated. The operation of the switch was then characterised by usingplotting the power contrast between the two output guides 6 and 7, being given by

$$P_{contrast} = 10\log(P_{eog3}/P_{eog4}). \qquad (8.25)$$

Figure 8-13 illustrates the simulated power contrast between the output waveguides simulated using the SI method. Two cases are illustrated; one for the modulation of guide eog3 only with no bias applied to guide eog4, and secondly the modulation of guide eog4 only with no bias applied to guide eog6. The complete switching of power from one guide to the other can clearly be seen to occur at $n\pi/2$ for $n = 1,3,5......$. The point at which switching occurs may be controlled by applying a constant bias to one electro-optic guide whilst the other is modulated, figure 8-14. Figure 8-15 further demonstrates the switching process and shows the optical field totally switched to either output guide.
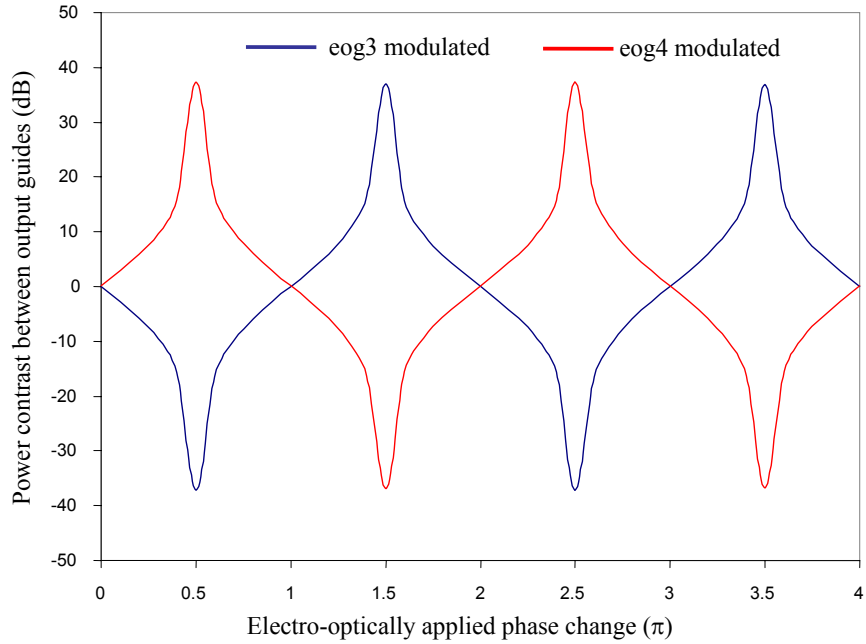
**Figure 8-13** SI simulation of the power contrast of the output waveguides for the 1x2 switch illustrated in figure 8-12 as a function of applied phase change.
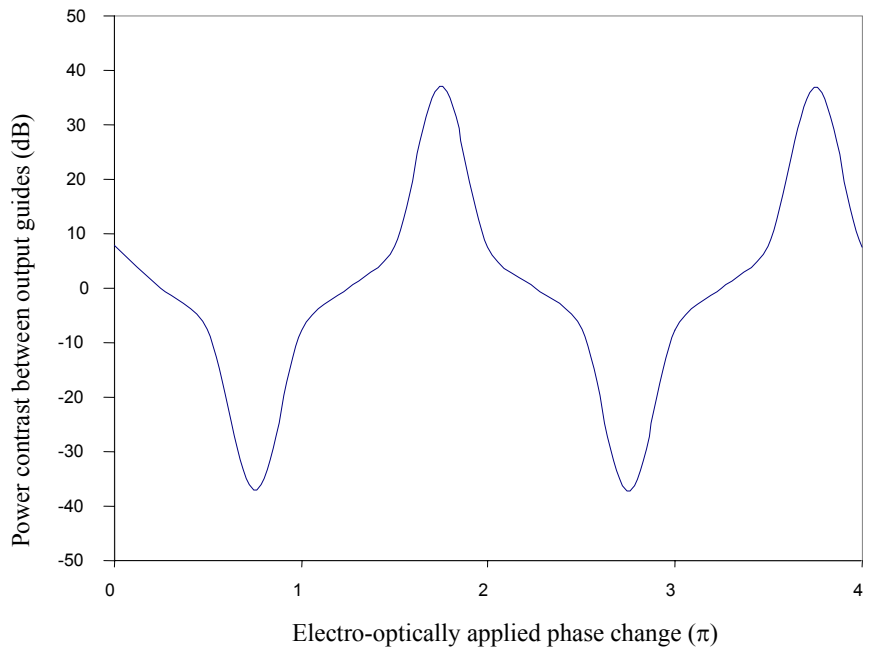


**Figure 8-14** SI simulation of the power contrast of the output waveguides for the 1x2 switch illustrated in figure 8-12 with the eog3 modulated and the eog4 biased at $0.25\pi$.
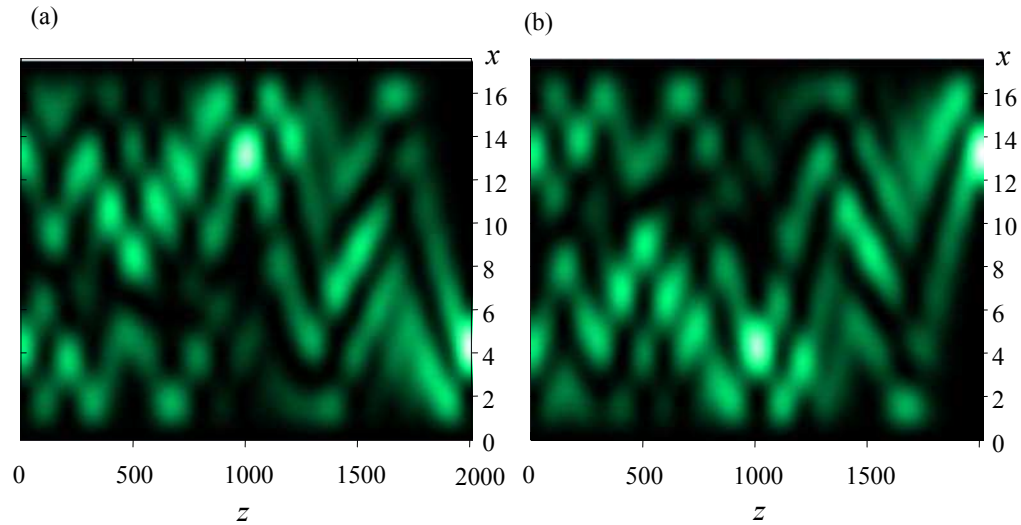
187

**Figure 8-15** Contour plot of the optical field in the MMI guide (guide 5 in figure 8-9); (a) switched to output guide 6, and (b) switched to output guide 7 (all dimensions in microns).

## 8.5   Conclusion

The efficiency and accuracy of the SI method has been exploited and applied for the first time to a scattering matrix approach to the analysis of optical waveguide circuits. The method presented has been applied to a range of structures of practical importance and the results obtained are shown to agree with other published work. Although the method has been demonstrated through application to MMI based devices any situation where the circuit maybe decomposed into a number of discrete waveguide blocks lends itself to an analysis by the method presented. MMI devices are by their nature 'wide angle' and accurate analysis by purely numerical methods, such as FD-BPM, would prove extremely costly in terms of computational resources. The SI based approach requires minimal effort yielding results for complex circuits in a matter of minutes to a high degree of accuracy.

## 8.6 References

[8.1] X. J. M. Leijtens, P. Le Lourec, and M. K. Smit, "S-Matrix Oriented CAD-Tool for Simulating Complex Integrated Optical Circuits", IEEE J. Selected Topics in Quantum Electronics, **2**, 257-262 (1996).

[8.2] E. C. M. Pennings, R. J. Deri, A. Scherer, R. Bhat, T. R. Hayes, N. C. Andreadakis, M. K. Smit, L. B. Soldano, and R. J. Hawkins, "Ultracompact, low-loss directional couplers on InP based on self-imaging by multimode interference", Applied Physics Letters, vol. 59(16), pp.1926-1928, 1991.

[8.3] L.B Soldano, F.B. Veerman, M.K. Smit, B.H. Verbeek, A.H. Dubost, and E.C.M. Pennings, "Planar monomode optical couplers based on multimode interference effects", IEEE Journal of Lightwave Technology, vol. 10 (12), pp. 1843 -1850, 1992.

[8.4] F.B. Veerman, P.J Schalkwijk, E.C.M. Pennings, M.K. Smit, B.H. Verbeek, "An optical passive 3-dB TMI-coupler with reduced fabrication tolerance sensitivity", IEEE Journal of Lightwave Technology, vol. 10 (3), pp. 306 -311, 1992.

[8.5] Q. Lai, M. Bachmann, and  H. Melchior, "Low-loss 1x*N* multimode interference couplers with homogenous output power distributions realised in silica on Si material", Electronics Letters, vol. 33(20), pp. 1966-1700, 1997.

[8.6] J. M. Heaton, R. M. Jenkins, D. R. Wight, J. T. Parker, J. C. H. Birbeck, and K. P. Hilton, "Novel 1-to-N way integrated optical beam splitters using symmetric mode mixing in GaAs/AlGaAs multimode wavguides", Applied Physics Letters, vol. 61(15), pp. 1754-1756, 1992.

[8.7] R. M. Jenkins, J. M. Heaton, D. R. Wight, J. T. Parker, J. C. H. Birbeck, G. W. Smith, and K. P. Hilton, "Novel 1xN and NxN integrated optical switches

using self-imaging multimode GaAs/AlGaAs waveguides", Applied Physics Letters, vol. 64(6), pp. 684-686, 1994.

[8.8] M. R. Paiam, C. F. Janz, R. I. McDonald, and J. N. Broughton, "Compact planar 980/1550-nm wavelength multi/demultiplexer based on multimode interference", IEEE Photonics Technology Letters, vol. 27(10), pp. 1180-1182, 1995.

[8.9] K. C. Lin, and W. Y. Lee, "Guided-wave 1.3/1.55µm wavelength division multiplexer based on multimode intereference", Electronics Letters, vol. 32(14), pp. 1259-1262, 1996.

[8.10] M. R. Paiam, R. I. McDonald, "A 12 channel phased-array wavelength multiplexer with multimode interference couplers", IEEE Photonics Technology Letters, vol. 10(2), pp. 241-243, 1998.

[8.11] B. Li, G. LI, E. Liu, Z. Jiang, J. Qin, and X. Wang, "Low-loss 1x2 multimode interference wavelength demultiplexer in silicon-germanium alloy", IEEE Photonics Technology Letters, vol. 11(5), pp. 575-577, 1999.

[8.12] R. Ulrich, and G. Ankele, "Self-imaging in homogeneous planar optical waveguides", Applied Physics Letters, vol. 27(6), pp. 337-339, 1975.

[8.13] L. B. Soldano, and E. C. M. Pennings, "Optical multi-mode interference devices based on self-imaging: Principles and applications", IEEE Journal of Lightwave Technology, vol. 13(4), pp. 615-627, 1995.

[8.14] J. M. Heaton, M. M. Bourke, S. B. Jones, B. H. Smith, K. P. Hilton, G. W. Smith, J. C. H. Birbeck, G. Berry, S. V. Dewar, and D. R. Wight, "Optimization of deep-etched, single mode GaAs/AlGaAs optical waveguides using controlled leakage into the substrate", IEEE Journal of Lightwave Tech., vol. 17(2), pp. 267-281, 1999.

# Chapter 9  Generalised 3D Spectral Index Method

## 9.1   Introduction

The previous chapter introduced the use of a mode matching method based upon the Spectral Index (SI) method for the analysis of optical circuits. In this chapter an alternative SI based approach to propagation analysis in three-dimensional rib waveguide based optical circuits is presented.
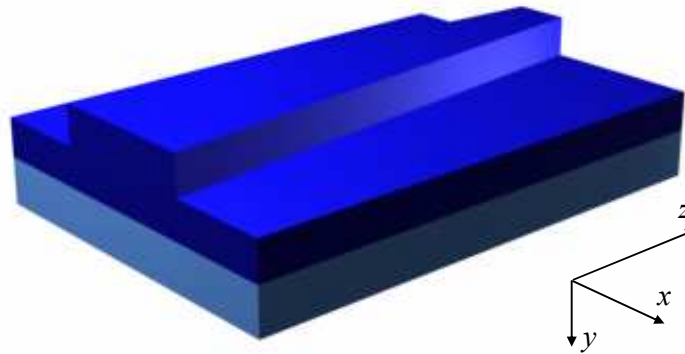


**Figure 9-1** Illustration of a tapered rib waveguide formed from a simple three-layer slab waveguide.

A full theoretical development of the method is presented in this chapter, along with a discussion of the implementation and application to a typical practical problem illustrative of including taper-based spot-size converters. Comparisons with direct numerical methods show the new technique to be sufficiently accurate for the design of many optoelectronic components.

**Figure 9-2** Transverse cross section of the tapered waveguide of figure 9-1 taken at an arbitrary point along its length.

## 9.2   Theory

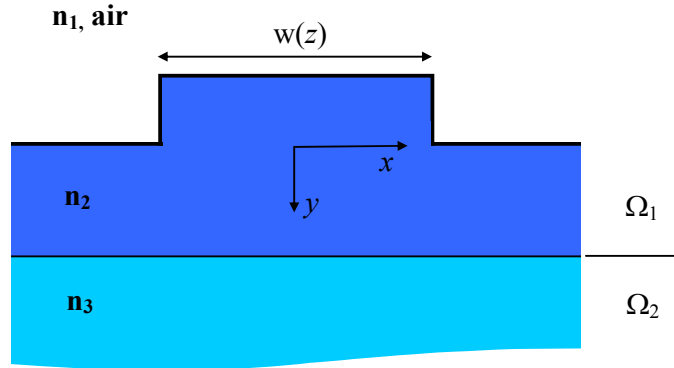Consider a simple three-dimensional, *z*-variant, air clad rib waveguide such as the tapered structure illustrated in Figure 9-1 and in the plane of cross-section in figure 9-2. It is fair to assume, due to the high refractive index contrast at the air-semiconductor boundary, that any scattered field will be predominantly into the substrate, with very little field present in the air region. Under this condition the actual structure may be replaced with an effective structure whose boundaries are displaced a small distance into the air region, the field at and outside of these boundaries being set to zero, [9.1]. This approach forms one of the key assumptions of the SI method presented earlier in this thesis and results in an effective structure that is significantly easier to analyse. The boundary displacements are, as for the standard SI method, polarisation dependant and are given by

$$\Delta_t = \frac{1}{\sqrt{\beta^2 - k_0^2}} \qquad , \qquad \Delta_n = \frac{1}{n_2^2}\Delta_t \qquad\qquad (9.1)$$

where $\Delta_n$ and $\Delta_t$ denote the displacement on those boundaries that are normal and tangential to the principal field component respectively. Here the subscripts $_t$ and $_n$ denote the tangential and normal component of the principal field component respectively, $\beta$ is the local propagation constant of the fundamental mode, $k_0$ is the free space wave number and $n_2$ is the refractive index of the guide. The significance of this approximation is that the field in the resulting structure can now be completely determined from the field at the base of the effective rib $y = 0$. Therefore the field in a fully three-dimensional structure is characterised by the field on a two dimensional surface.

The standard method proceeds by representing the field as an expansion of the local solutions of the wave equation in both the rib and the multi-layered substrate, which are then matched at their interface with a variational boundary condition resulting in a simple transcendental equation. But as the waveguide being considered is no longer invariant in the direction of propagation the trial function for the field in the rib requires modification from that used in the standard SI method, (chpt. 3). Consequently the variational principle is now expected to include an additional term reflecting the modification of this trial function. The field in the substrate region however, can still be represented as a superposition of plane waves that exactly satisfies the wave equation.

## 9.2.1  The Variational Expression

Consider the variational expression

$$k_0^2 = \frac{\iiint dx\,dy\,dz\ \nabla \mathbf{E}^* \nabla \mathbf{E}}{\iiint dx\,dy\,dz\ \mathbf{E}^* \mathrm{n}^2 \mathbf{E}} \tag{9.2}$$

where an additional integral is included over the standard expression, (§3.6) to account for the extension to a three dimensional domain. In equation (9.2) n, now a function of $(x,y,z)$, is the local refractive index and *E* is an approximation to the electric field the true expression for which is required to satisfy the wave equation

$$\left( \nabla^2 + n^2 k_0^2 \right) \mathbf{E} = 0 \tag{9.3}$$

Integrating equation (9.2) by parts

$$
k_0^2 = \frac{-\iiint\limits_{\Omega_1} dxdydz\ \mathbf{E}^* \nabla^2 \mathbf{E} + \iint\limits_{y=0^+} dxdz\ \mathbf{E}^* \dfrac{d\mathbf{E}}{dy} - \iiint\limits_{\Omega_2} dxdydz\ \mathbf{E}^* \nabla^2 \mathbf{E} + \iint\limits_{y=0^-} dxdz\ \mathbf{E}^* \dfrac{d\mathbf{E}}{dy}}{\iiint\limits_{\Omega_1+\Omega_2} dxdydz\ n^2 \left| \mathbf{E} \right|^2}
$$

$$\tag{9.4}$$

$$
= \frac{-\iiint\limits_{\Omega_1+\Omega_2} dxdydz\ \mathbf{E}^* \nabla^2 \mathbf{E} + \iint dxdz \left[ \mathbf{E}^* \dfrac{d\mathbf{E}}{dy} \right]_{y=0^-}^{y=0^+}}{\iiint\limits_{\Omega_1+\Omega_2} dxdydz\ n^2 \left| \mathbf{E} \right|^2}
$$

where $\Omega_1$ and $\Omega_2$ are the rib and underlying substrate regions respectively, figure 9-2. It is required that equation (9.4) be minimised to $k_0^2$ for the exact solution of $\boldsymbol{E}$, therefore re-writing equation (9.4) in order to identify the condition for which this occurs.

$$k_0^2 = \frac{-\iiint\limits_{\Omega_1+\Omega_2} dxdydz\ \boldsymbol{E}^*\nabla^2\boldsymbol{E} \pm \boldsymbol{E}^*n^2k_0^2\boldsymbol{E} + \iint dxdz\ \left[\boldsymbol{E}^*\dfrac{d\boldsymbol{E}}{dy}\right]_{y=0^-}^{y=0^+}}{\iiint\limits_{\Omega_1+\Omega_2} dxdydz\ n^2\left|\boldsymbol{E}\right|^2}$$

$$= \frac{\iiint\limits_{\Omega_1+\Omega_2} dxdydz\ \left(\left|\boldsymbol{E}\right|^2 n^2k_0^2 - \boldsymbol{E}^*\left(\nabla^2+n^2k_0^2\right)\boldsymbol{E}\right) + \iint dxdz\ \left[\boldsymbol{E}^*\dfrac{d\boldsymbol{E}}{dy}\right]_{y=0^-}^{y=0^+}}{\iiint\limits_{\Omega_1+\Omega_2} dxdydz\ n^2\left|\boldsymbol{E}\right|^2}$$

(9.5)

Equation (9.5) can be re-written as

$$k_0^2 = \frac{\iiint\limits_{\Omega_1+\Omega_2} dxdydz\ \left(\left|\mathbf{E}\right|^2 n^2k_0^2\right) - \iiint\limits_{\Omega_1+\Omega_2} dxdydz\ \mathbf{E}^*\left(\nabla^2+n^2k_0^2\right)\mathbf{E} + \iint dxdz\ \left[\mathbf{E}^*\dfrac{d\mathbf{E}}{dy}\right]_{y=0^-}^{y=0^+}}{\iiint\limits_{\Omega_1+\Omega_2} dxdydz\ n^2\left|\mathbf{E}\right|^2}$$ (9.6)

In the volume $\Omega_2$ for the exact solution of $\boldsymbol{E}$, the wave equation (9.3) is satisfied exactly, i.e.

$$\iiint\limits_{\Omega_2} dxdydz\ \mathbf{E}^*\left(\nabla^2+n^2k_0^2\right)\mathbf{E} = 0$$ (9.7)

Applying (9.7) to (9.6) gives

$$
k_0^2 = \frac{\iiint\limits_{\Omega_1+\Omega_2} dxdydz \left(|\mathbf{E}|^2 n^2 k_0^2\right) - \iiint\limits_{\Omega_1} dxdydz \ \mathbf{E}^* \left(\nabla^2 + n^2 k_0^2\right)\mathbf{E} + \iint dxdz \left[\mathbf{E}^* \frac{d\mathbf{E}}{dy}\right]_{y=0^-}^{y=0^+}}{\iiint\limits_{\Omega_1+\Omega_2} dxdydz \ n^2 |\mathbf{E}|^2} \quad (9.8)
$$

It can now be seen that the right hand side of equation (9.8) is minimised to $k_0{}^2$ when the variational boundary condition

$$
\iiint\limits_{\Omega_1} dxdydz \ \boldsymbol{E}^* \left(\nabla^2 + n^2 k_0^2\right)\boldsymbol{E} + \iint dxdz \left[\boldsymbol{E}^* \frac{d\boldsymbol{E}}{dy}\right]_{y=0^-}^{y=0^+} = 0 \quad (9.9)
$$

is satisfied.

## 9.2.2  Field Formulation

For cases where the waveguide geometry is slowly varying in the direction of propagation, the field may be approximated by the simple trial function

$$
\boldsymbol{E} = \frac{A(z)}{N(z)} \cos(s_1 x) \frac{\sin(\gamma_1(y+h))}{\sin(\gamma_1 h)} e^{-\int dz \ \beta} \quad (9.10)
$$

where in general W is the effective width of the rib and is consequently a function of

z, $s_1 = \dfrac{\pi}{2W}$ and β is the propagation constant of the local fundamental mode of the

waveguide. $\gamma_1$ and the local normalisation constant N(z) are given by

$$\gamma_1^2 = n^2 k_0^2 - s_1^2 - \beta^2$$

(9.11)

$$N^2(z) = \iint_{\Omega_1} dxdy \; \Phi^2(x, y, z) \quad , \quad \Phi(x,y,z) = \cos(s_1 x) \frac{\sin(\gamma_1(y+h))}{\sin(\gamma_1 h)}$$

and *A(z)* is a slowly varying envelope. Using equation (9.10) the following term

appearing in equation (9.9) can be evaluated

$$\iint dxdz \; E^*(x, +0, z) \frac{d\mathbf{E}}{dy}(x, +0, z) = \int dz \left( \frac{|A(z)|}{N(z)} \right)^2 w(z) \gamma_1 \cot(\gamma_1 h) \quad (9.12)$$

Below the rib a 2D Fourier transform of  (9.10) is taken such that

$$e(s,t) = \int_{-\infty}^{\infty} dx \int_{-\infty}^{\infty} dz \; e^{-j(sx+tz)} \frac{A(z)}{N(z)} \cos(s_1 x) e^{-j\int dz\beta}$$

(9.13)

$$= \int_{-\infty}^{\infty} dz \; \frac{A(z)}{N(z)} \left( \frac{2s_1 \cos(sw)}{s_1^2 - s^2} \right) e^{-jtz} e^{-j\int dz\beta}$$

thus allowing the field in the substrate to be expressed as a simple superposition of plane waves. For these plane waves a response function of the layered substrate, $\Gamma(s,t)$, can be found such that

$$\left.\frac{de}{dy}(s,t)\right|_{y=-0} = \Gamma(s)e(s,t)\big|_{y=-0} \tag{9.14}$$

Consequently the following term in (9.9) is obtained from Parseval's theorem

$$\iint ds\ \mathbf{E}^*(x,-0,z)\frac{d\mathbf{E}}{dy}(x,-0,z) = \left(\frac{1}{2\pi}\right)^2 \int_{-\infty}^{\infty} ds \int_{-\infty}^{\infty} dt\ e^*(s,t)\Gamma(s,t)e(s,t) \tag{9.15}$$

The first term in equation (9.9) is evaluated as

$$\iiint_{\Omega_1} dxdydz \left(\frac{A}{N}\Phi e^{-j\int dz\beta}\right)^* \left(\begin{bmatrix}\dfrac{d^2A}{dz^2} - 2j\beta\dfrac{dA}{dZ} - jA\dfrac{d\beta}{dZ}\end{bmatrix}\dfrac{\Phi}{N} \\ +2\begin{bmatrix}-j\beta A + \dfrac{dA}{dz}\end{bmatrix}\dfrac{d}{dz}\left(\dfrac{\Phi}{N}\right) + A\dfrac{d^2}{dz^2}\left(\dfrac{\Phi}{N}\right)\end{bmatrix}\right) e^{-j\int dz\beta} \tag{9.16}$$

where advantage has been taken of the fact that

$$\left(\frac{d^2}{dx^2} + \frac{d^2}{dx^2} + k^2 - \beta^2\right)\frac{\Phi}{N} = 0 \tag{9.17}$$

noting that the definition of $N(z)$ ensures that

$$\iint\limits_{\Omega_1} dxdy \ \frac{\Phi}{N}\frac{d}{dz}\left(\frac{\Phi}{N}\right) = 0 \tag{9.18}$$

Neglecting second order terms, which physically corresponds to the case of quasi-paraxial propagation, (9.16) becomes

$$\int dz \ A^*(z)\left[-2j\beta\frac{dA}{dz} - jA\frac{d\beta}{dz}\right] \tag{9.19}$$

Therefore substituting equations (9.12), (9.15) and (9.19) into equation (9.9) gives

$$\int dz \ A^*(z)\left(A\frac{w'}{N^2}\gamma_1\cot(\gamma_1 h) - 2j\beta\frac{dA}{dz} - jA\frac{d\beta}{dz}\right)$$
$$= \left(\frac{1}{2\pi}\right)^2\int\limits_{-\infty}^{\infty} ds\int\limits_{-\infty}^{\infty} dt \ e^*(s,t) \ \Gamma(s,t) \ e(s,t) \tag{9.20}$$

which is the expression A(z) must satisfy.

For a *z* invariant waveguide such that *A*=1 and β is constant, equation (9.13) gives

$$e(s,t) = \frac{2\pi\delta(t+\beta)}{N}\left(\frac{2s_1\cos(sw)}{s_1^2 - s^2}\right) \tag{9.21}$$

noting that

$$\delta(x) = \frac{1}{2\pi}\int\limits_{-\infty}^{\infty} dk \ \exp(ikx) \quad \text{and for } x = 0 \quad \delta(0) = \frac{1}{2\pi}\int\limits_{-\infty}^{\infty} dk$$

Equation (9.20) Then becomes

$$\int\limits_{-\infty}^{\infty} dz \; \frac{w'}{N^2} \gamma_1 \cot(\gamma_1 h) = \delta(0) \int\limits_{-\infty}^{\infty} ds \; \Gamma(s,-\beta) \left( \frac{2s_1 \cos(sw)}{s_1^2 - s^2} \right) \tag{9.22}$$

which upon noting that

$$\int\limits_{-\infty}^{\infty} dz = 2\pi\delta(0)$$

yields the standard SI dispersion equation for the fundamental mode of a *z*-invariant rib waveguide, (§3.6)

$$\frac{w'}{N^2} \gamma_1 \cot(\gamma_1 h) = \frac{1}{2\pi} \int\limits_{-\infty}^{\infty} ds \; \Gamma(s,-\beta) \left( \frac{2s_1 \cos(sw)}{s_1^2 - s^2} \right) \tag{9.23}$$

Equation (9.23) is satisfied as β is defined as the local propagation constant of the rib waveguide.

## 9.3   Implementation and Numerical Results

The following section details the implementation and solution of the previously presented theory.

## 9.3.1  Practical Implementation

In order to solve  (9.20) for $A(z)$ it is necessary to discretise (9.10) as a superposition of simple basis terms, a technique commonly applied in the analysis of microstrip lines [9.2]-[9.5]. In order to achieve this, the structure is modelled as a sequence of overlapping segments each of which has a fixed width, figure 9-3. Within each segment, $A(z)$ is represented by a triangular function whose amplitude is an unknown of the discretised problem, such that overall $A(z)$ is approximated in a piecewise linear manner, figure 9-4. These overlapping segments have certain numerical advantages, which recommend their use. Firstly, the two-dimensional Fourier transform of each is separable which significantly reduces the calculation time (evaluation of two one dimensional Fourier transforms instead of one two dimensional Fourier transform). Furthermore, as the field in each of these segments is zero on all its edges these transforms converge more quickly than if "rooftop" functions had been chosen. Secondly, and more significantly, this representation does not lead to spurious air-semiconductor interfaces in the x-y plane, which would occur if the segments did not overlap.
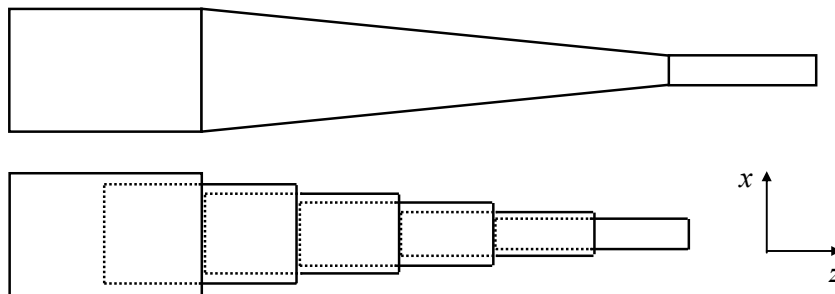


**Figure 9-3** Tapered rib waveguide and its subsequent representation as overlapping uniformegments.
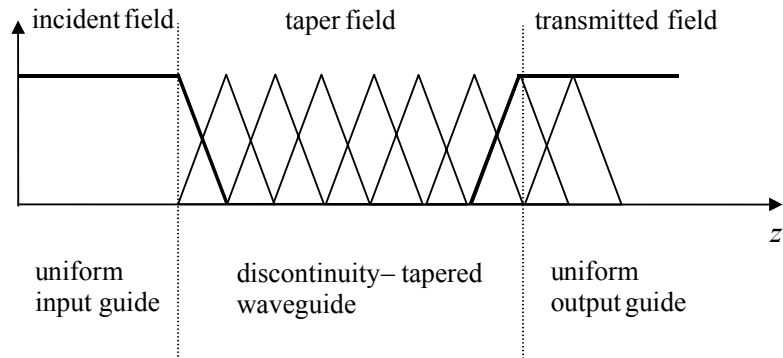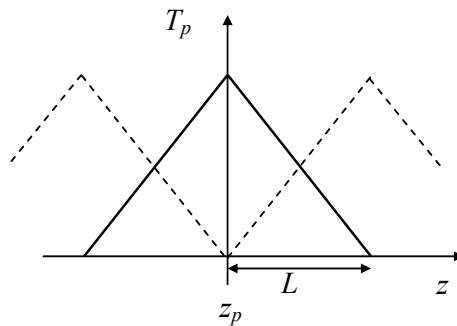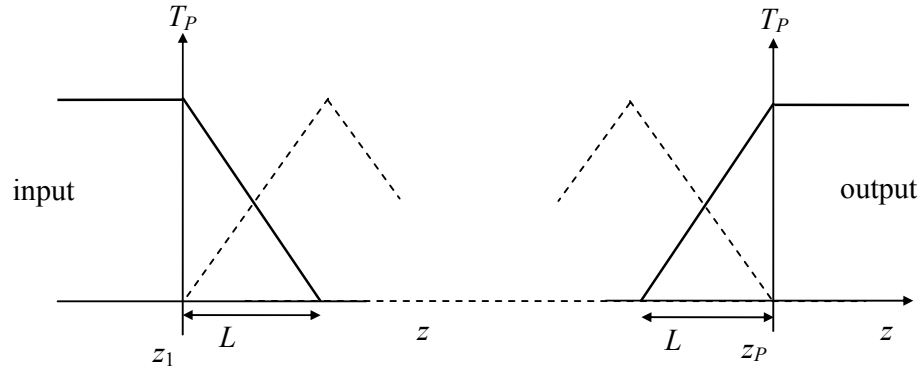
**Figure 9-4** Triangular basis function representation of the field at the base of the rib.

To obtain the discrete equivalent to (9.20) the basis functions are defined such, that

for $p \neq 1$ and $p \neq P$



$$T_p(z) = \left(1 + \frac{(z - z_p)}{L}\right) \quad \text{for } -L < (z - z_p) < 0$$

$$= \left(1 - \frac{(z - z_p)}{L}\right) \quad \text{for } 0 < (z - z_p) < L$$

(9.24)

and for p=1 and p=P



$$T_1(z) = 1 \text{ for } z < 0 \text{ , } T_1(z) = \left(1 - \frac{(z - z_1)}{L}\right) \qquad \text{for } 0 < z - z_1 < L$$

$$(9.25)$$

$$T_P(z) = \left(1 + \frac{(z - z_P)}{L}\right) \text{ for } -L < z - z_P < 0 \text{ , } T_P(z) = 1 \text{ for } z > z_P$$

In the input guide the field is initially assumed to consist only of the incident guided mode. In the output guide, the field is modelled as a transmitted guided mode, which is augmented with additional basis functions to model the field disturbances, which are localised to the discontinuity.

If P overlapping segments are used to expand the field, then along with the amplitude of the transmitted guided mode there are P+1 unknowns to be found. The Rayleigh-Ritz approach, [9.6], is applied to the variational expression using the P segment functions as the test functions along with an additional one in the output guide (shown dashed in figure 2). Thus upon substitution into equation (9.20) a

linear system of P+1 equations in P+1 unknowns is recovered which is of moderate

order and straight forward in its solution. Therefore using (9.24) and (9.25), equation

(9.20) can be re-expressed as

$$
\begin{aligned}
&\sum_{q=1}^{P}\int_{-\infty}^{\infty} dz\; T_p(z)\left(\frac{w_q'}{N_q^2}\gamma_{1q}\cot(\gamma_{1q}h)T_q(z)-2j\beta\frac{d}{dz}T_q(z)\right)A_p \\
&-\sum_{q=1}^{P}\left(\frac{1}{2\pi}\right)^2\int_{-\infty}^{\infty} ds\int_{-\infty}^{\infty} dt\; t_p^{\;*}(s,t)\;\Gamma(s,t)\;t_q(s,t)A_p \\
&=-\int_{-\infty}^{\infty} dz\; T_p(z)\left(\frac{w_1'}{N_1^2}\gamma_{11}\cot(\gamma_{11}h)T_1(z)-2j\beta\frac{d}{dz}T_1(z)\right) \\
&+\left(\frac{1}{2\pi}\right)^2\int_{-\infty}^{\infty} ds\int_{-\infty}^{\infty} dt\; t_p^{\;*}(s,t)\;\Gamma(s,t)\;t_1(s,t)
\end{aligned}
\tag{9.26}
$$

where

$$
t_p(s,t)=\int_{-\infty}^{\infty} dz\;\frac{T_p(z)}{N(z)}\left(\frac{2s_1\cos(sw_p')}{s_1^2-s^2}\right)e^{-jtz}e^{-j\int dz\beta}
\tag{9.27}
$$

and $A_1$, the amplitude of the incident field is taken as 1 without loss of generality.

Expressing equation (9.26) in matrix form

$$
\left(\overline{\overline{\mathbf{W}}}-\overline{\overline{\mathbf{X}}}\right)\cdot\overline{\mathbf{A}}=\overline{\mathbf{Y}}+\overline{\mathbf{Z}}
\tag{9.28}
$$

where $\overline{\overline{\mathbf{W}}}$ and $\overline{\overline{\mathbf{X}}}$ are square matrices whose elements are given by

$$W = \sum_{q=2}^{P} \int_{-\infty}^{\infty} dz \; T_p(z) \left( \frac{w_q'}{N_q^2} \gamma_{1q} \cot(\gamma_{1q}h) T_q(z) - 2j\beta \frac{d}{dz} T_q(z) \right)$$

$$\text{(9.29)}$$

$$X = \sum_{q=2}^{P} \left( \frac{1}{2\pi} \right)^2 \int_{-\infty}^{\infty} ds \int_{-\infty}^{\infty} dt \; t_p^{\;*}(s,t) \; \Gamma(s,t) \; t_q(s,t)$$

$\overline{\mathbf{Y}}$ and $\overline{\mathbf{Z}}$ are vectors with elements

$$Y = \int_{-\infty}^{\infty} dz \; T_p(z) \left( \frac{w_1'}{N_1^2} \gamma_{11} \cot(\gamma_{11}h) T_1(z) - 2j\beta \frac{d}{dz} T_1(z) \right)$$

$$\text{(9.30)}$$

$$Z = \left( \frac{1}{2\pi} \right)^2 \int_{-\infty}^{\infty} ds \int_{-\infty}^{\infty} dt \; t_p^{\;*}(s,t) \; \Gamma(s,t) \; t_1(s,t)$$

and $\overline{\mathbf{A}}$ is the vector of unknown basis function amplitudes.

## 9.3.2  Numerical Results

Figure 9-5 schematically illustrates the geometry of a linear embossed tapered waveguide that was analysed by the new method discussed. The dimensions of the taper are $W_{in}$ = 3µm, $W_{out}$ = 1.6µm, H = 1µm and $L_{taper}$ = 100µm, with material refractive indices being taken as $n_{sub}$ = 3.40 and $n_{rib}$ = 3.44 at a wavelength of 1.15µm. In order to verify the accuracy of the method presented, comparisons were drawn with those results obtained via a finite difference beam propagation method (FD-BPM), (§2.8.3). Quantitative comparisons of the field along the base rib obtained by both methods were made. Also examined was the convergence of the

solution of the new method presented with number of overlapping segments used to define the taper.

In order to quantitatively compare the results produced by the Spectral Index method (hence for the referred to as 3D-SI) and the FD-BPM, a measure of the field, $E_{0,}$ across the base of the rib was used, where $E_0$ is defined as

$$E_0(z) = \int\limits_0^W dx \sqrt{\frac{2}{W}} \cos\frac{\pi x}{W} \; E(x, y = 0) \qquad (9.31)$$

The results are shown in figure 9-6. It is clearly seen that very good agreement is obtained between the methods. Figure 9-7 show the field distribution obtained by each method. Again very good agreement between the methods is obtained. In the case of the field generated by the FD-BPM the penetration of the field into the air cladding can just be made out. The fact that this field penetration is small further goes to justify the use of the effective boundary approximation used in developing the 3D-SI approach.
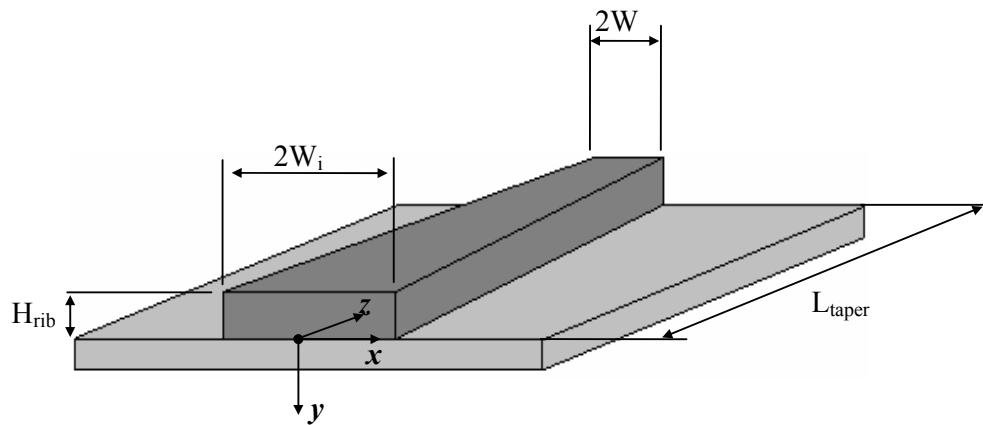
**Figure 9-5** Schematic illustration of a linear embossed tapered rib waveguide.

Finally, figure 9-8 depicts the convergence of the field across the base of the rib predicted by the 3D-SIM with the number of segments used to describe the taper. As opposed to the FD-BPM, which may typically use a longitudinal mesh size of 1μm or even 0.5μm for the structure analysed, excellent convergence is seen in the case of the 3D-SI for equivalent step sizes of 5μm. This cruder sampling allows for substantially reduced computation times without loss of accuracy. Computation times in the order of minutes are achieved with the 3D-SI, which compares favourably to FD-BPM approaches typically requiring ~1 hour. As the 3D-SI requires only a 2D discretisation of the problem space, compared to a 3D discretisation required by FD-BPM, along with the ability to employ a coarser discretisation without loss of accuracy, the method requires little in the way of computational resources.
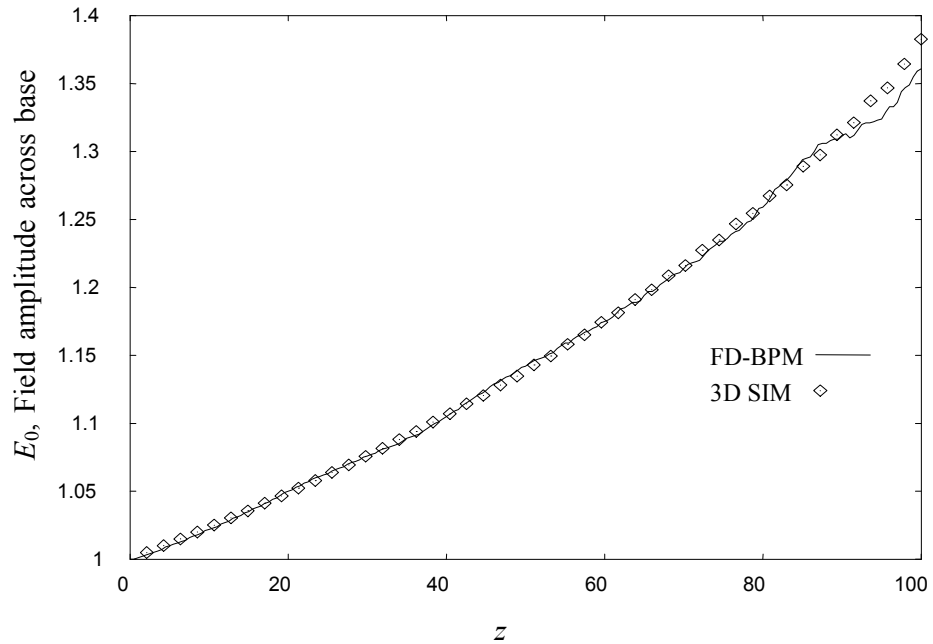
**Figure 9-6** Comparison of field amplitudes across base of rib, $E_0$, given by 3D-SIM and FD-BPM.
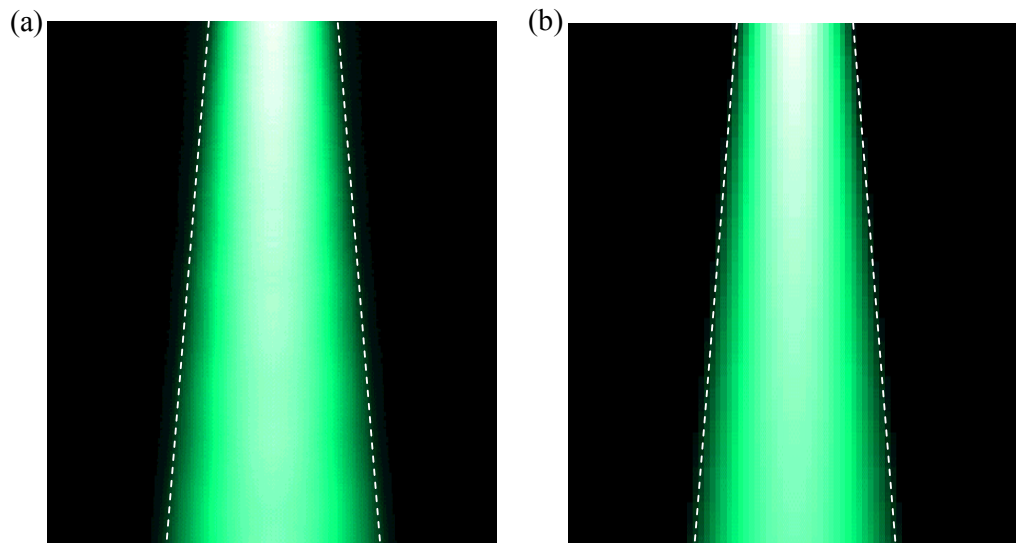


**Figure 9-7** Field distributions along the base of the rib (a) FD-BPM, (b) 3D-SIM. The broken white lines indicate the physical boundary of the structure.
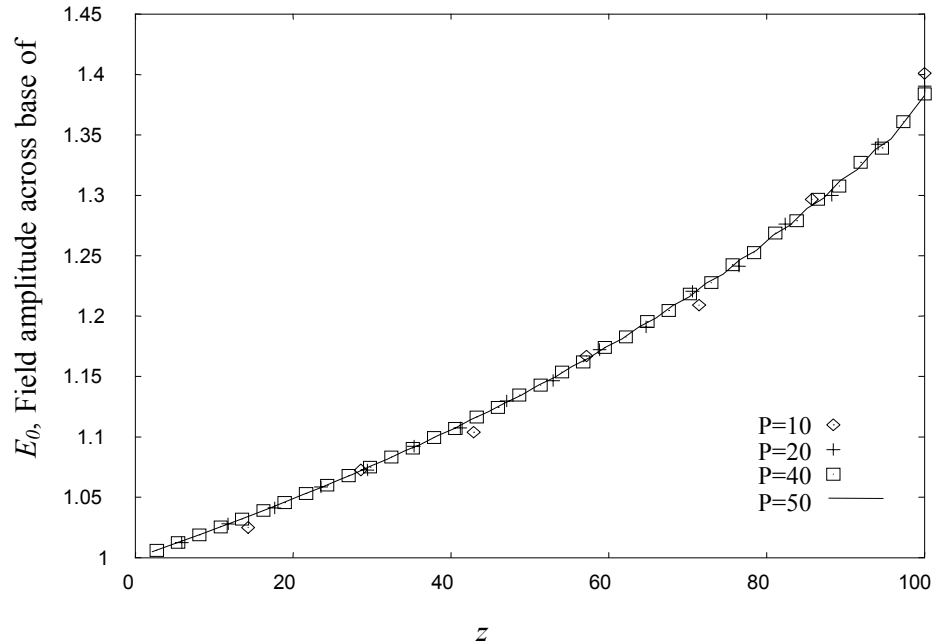
**Figure 9-8** Convergence of the field, $E_0$, predicted by the 3D-SIM with number of segments, P, used to describe taper.

## 9.4 Conclusions

A novel and highly efficient method based on the spectral index method that is suitable for the analysis of a broad range of optoelectronic integrated components and circuits. The method presented is based on rigorous field theory, with both the theoretical derivation and its practical implementation being detailed in this work. The method was validated through the analysis of a tapered rib waveguide and ensuing comparison with results obtained from an existing technique, namely FD-BPM. Extension of the method to other structures e.g. y-branches, bends and t-junctions can be envisaged and is possible with modification of the basis functions chosen.

## 9.5 References

[9.1] M. A. Matin, T. M.Benson, P. C. Kendall, M. S. Stern,'New technique for finite difference analysis of optical waveguide problems', International Journal of Numerical Modelling: Electronic Networks, Devices and Fields, vol. 7, no. 1, pp. 25-33, 1994.

[9.2] T. Itoh, R. Mittra, "A technique for computing dispersion characteristics of shielded microstrip lines", IEEE Trans. Microwave Theory and Techniques, vol. MTT-22, pp. 896-898,1974.

[9.3] R. W. Jackson, D. M. Pozar, "Full-wave analysis of microstrip open-end and gap discontinuities", IEEE Trans. Microwave Theory and Techniques, vol. MTT-33(10), pp. 1036-1042, 1989.

[9.4] R. W. Jackson, "Full wave, finite element analysis of irregular microstrip discontinuities", IEEE Trans. Microwave Theory and Techniques, vol. MTT-37(1), pp. 81-89, 1989.

[9.5] S. A. Meade, C. J. Railton, "Efficient implementation of the spectral domain method including precalculated corner basis functions", IEEE Trans. Microwave Theory and Techniques, vol. MTT-42(9), pp. 1678-1684, 1994.

[9.6] R. E. Collin, "Field theory of guided waves", IEEE Press, 1991.

[9.7] P. Sewell, Private communication.

# Chapter 10    Conclusions

The following will review the work the main conclusions of the work presented in this thesis and draw on those conclusions, where necessary, for suggestions of further work.

The Spectral Index (SI) method is a well established method for the analysis of rectangular, air-clad semiconductor rib waveguides. It has been shown to be highly accurate and computationally efficient when compared to the more exact, benchmark numerical methods. The philosophy of the basic SI method lends itself well to exploitation in the analysis of a wider range of optoelectronic components and circuits that fall within the remit of the key assumptions of the basic method; that the devices have a high core/cladding refractive index contrast resulting in negligible field penetration into the cladding and that the modes supported by the structure are essentially polarised.

The aim of this work was to therefore develop and extend the SI method to a wider class of waveguiding components and circuits and further demonstrate its suitability as a practical design tool. In respect of the latter, an extension of the SI method for the analysis of optical modes spot size converters (SSC) was used to design a novel silicon germanium (SiGe) based SSC. The experimental device described was the first of its type to be demonstrated in this material system. The design process being

greatly aided by the efficiency of the SI method and its suitability for use as an iterative computer aided design tool. The application of a theoretical design tool to practical problems is not a straight-forward one. Knowledge of the material system has been shown to be an important consideration, together with the tolerancing and limitations of the fabrication process.

Semiconductor optical waveguide are often though of as ideal components with regards to modelling; rectangular waveguides are rectangular, side walls are smooth etc. The chemical processes involved in semiconductor fabricated have their own properties that can result in a waveguide that is far from ideal. In order to address this problem from a designer's point of view a novel extension to the SI method was developed for the modal analysis of rib waveguides with sloping side walls.

Accurate determination of modal propagation constants are required in order to implement a successful design. Knowledge of waveguide losses is an essential requirement characterising the overall performance of waveguiding components. The SI method in its complex form was applied for the first time to the analysis of waveguide losses attributable to the slab leakage mechanism, a mechanism that plays an essential part in the successful implementation of large, single mode rib waveguides – a class of waveguide that is of importance for it ease of coupling to optical fibres.

The novel extension of the SI method to a cylindrical co-ordinate system was carried out in order to provide an analysis tool for the characterisation of an important class of optical components –dielectric disc resonators. When operated in the whispering

gallery mode such devices are able to realise high Qs and are thus ideally suited for use as wavelength selective components. Essential to their successful exploitation are accurate design tools that reveal the optical characteristics. The SI implementation was shown to accurately predict the resonant wavelengths of the devices which are seen to be in very good agreement with those results produced by benchmark numerical methods. A fair estimation of the quality factors or Qs yielded by such devices was obtained. The subsequent extension of the approach to the analysis of dielectric ring resonators has been described and initial results provide an indication of the accuracy of the method. The method as applied to the dielectric rings is further believed to be extendable to the case of uniform waveguide bends. At the time of writing numerical instabilities in the algorithm's implementation hindered progress in this area.

The efficiency of the basic SI method was further exploited where it formed the basis of a mode matching approach to three dimensional optical circuit analysis. The method was proven in the design of several multi-mode interference waveguide based devices. The accurate prediction of waveguide characteristics and field profiles, together with the relative ease with which full circuit design curves can be obtained, make this a powerful method for the analysis of complete circuits that would otherwise require huge computational resources or prove prohibitive altogether.

A further novel extension of the SI generalises the basic approach to the analysis of three dimensional waveguiding structures. The previously described approach relied upon the representation of a complex optical circuit by a series of connected

'building blocks', the optical properties of which were computed in isolation before being connected through a scattering matrix. IN the generalised approach the three-dimensional structure is represented and simulated in its entirety. The methodology was demonstrated through application to a simple longitudinally variant tapered waveguide and the results were in excellent agreement with those produced by a finite difference beam propagation algorithm. The accuracy and efficiency obtained through the SI implementation provides confidence in its suitability for further application to a wide range of waveguide components and circuits that may compose many different components.

Overall the SI method in, now, its many formulations has been shown to be a powerful tool for the analysis of the optical properties of a wide range of practically important waveguides and photonic integrated circuits.